Research on emergent physical properties of integrated nanomaterials

Qiao Li

October 2020

Research on emergent physical properties of integrated nanomaterials

Qiao Li
Doctoral Program in Materials Science and Engineering

Submitted to the Graduate School of
Pure and Applied Sciences
in Partial Fulfilment of the Requirements
for the Degree of Doctor of Philosophy in
Engineering

at the University of Tsukuba

Contents

List of Figures

List of Abbreviations

AI	Artificial intelligence
ANN	Artificial neural network
AS	Active sleep
CCD	Charge-coupled device
CF	Conductive filament
CMOS	Complementary metal oxide semicoductor
CS	Computer science
CVD	Chemical vapor deposition
DC	Direct current
DL	Deep learning
DLG	Double-layer graphene
EDX	Energy-dispersive X-ray spectroscopy
EEG	Electroencephalogram
EG	Ethylene glycol
EPSP	Excitatory postsynaptic potential
HOPG	Highly oriented pyrolytic graphite
IR	Infrared
LIF	Leaky integrate-and-fire
LIT	Lock-in thermography
LTM	Long term memory
MEMS	Micro-electromechanical system
NA	Numerical aperture
NEMS	Nano electromechanical system
NREM	Non-rapid-eye-movement
NS	Normal sleep
NW	Nanowire
PCMO	$Pr_{0.7}Ca_{0.3}MnO_3$
PEDOT:PSS	Poly(3,4-ethylenedioxythiophene) polystyrene sulfonate
PMMA	Poly(methyl methacrylate)
PVP	Polyvinylpyrrolidone
RAM	Radom access memory
RC	Reservoir computing
REM	Rapid-eye-movement
RRAM	Resistive random access memory
SEM	Scanning electron microscopy
SLG	Single layer graphene
SNN	Spiking neural network
STDP	Spike time dependent plasticity
STM	Scanning tunneling microscopy
TEM	Transmission electron microscopy

Acknowledgements

Firstly, I would like to express my sincere gratitude to my supervisor, Prof. Tomonobu Nakayama, for his patience, motivation and encouragement during my Ph.D study and related research. His guidance helped me in all the time of experiments and preparation of this thesis. The system we have been working on has very limited references. Many ideas came out during the discussions with him and he always encouraged me to free the thought and to imagine and make creations. My research experience could not be satisfied without him.

Beside my supervisor, I would like to thank the rest of my thesis committee: Prof. Shigekawa Hidemi, Prof. Jie Tang and Prof. Nobuhiko Kobayashi, for their encouragement and insightful comments, and also for the hard questions which incented me to widen my research from various perspectives.

I want to thank the National Institute for Materials Science, for supporting my study expense.

My sincere thanks also goes to Prof. Da Jiang and Dr. Xuefu Zhang, who provided the precious high-quality graphene film and triggered my whole Ph.D research works. Though I changed the research directions later, their support on my first scientific work gave me the confidence to continue my studies.

I also want to thank Prof. Ken-ichi Uchida and Dr. Ryo Iguchi, who shared their high-performance Lock-in Thermography with me, and who taught me how to obtain high-quality thermal graph from my samples. Without their precious support, it would not be possible to finish this thesis.

I also want to send my sincere thanks to Prof. Wilfred van der Wiel, for offering me the summer internship opportunity in his groups and leading me working on diverse exciting projects.

I thank my current and previous fellows in Nano Functionality Integration Group: Prof. Shigeki Kawai, Dr. Yoshitaka Shingaya, Dr. Adrian Diaz-Alvarez, Dr. Rintaro Higuchi, Dr. Ming Li, Dr. Kewei Sun, Ms. Lingying Li, Ms. Kayoko Hatori, Ms. Keiko Tanaka and Ms. Yasuko Kato. They gave a warm working environment and valuable assistance, which made my daily experiment time and office life so wonderful. Special thanks to Dr. Yoshitaka Shingaya and Dr. Adrian Diaz-Alvarez, for the stimulating discussions, for the teaching and support whenever I fall into experimental trouble.

Last but not least, I want to thank my friends and my family, who have been with me all the time. Special thanks to Dr. Daiming Tang and his family, for their warm care in work and daily life.

All in one, time flies in a way I could not count, I will always remember their warm and kind help during my studying period in Japan.

Qiao Li
Tsukuba, Japan
October 2020

Chapter 1: Introduction

This chapter aims to give a brief introduction of the integrated nanomaterials, mainly focusing on the two integrated systems the author has been working on during her PhD course, graphene-integrated system and memristive network. The first section gives a general review of integrated nanomaterials, introducing two forms of integration architecture in material science. The second and third sections focus on the graphene-integrated system and memristive network, respectively. Both started with a comprehensive historical review of the base material in the integrated system and followed by the detail applications of it.

1.1   INTEGRATED NANOMATERIALS

Nanomaterial refers to a material with any external dimension of an internal structure or surface structure in the nanoscale. Compared to its macroscopic counterpart, nanomaterial often shows extraordinary physical or chemical properties. It ranges from zero dimension like fullerene and nanoparticle to two-dimensions like graphene, thin-film molecule, covering organic, inorganic and carbon materials. The discovery of nanomaterials boosts the development of nanotechnology, where nanomaterials usually integrated into different architectures, emerging unique physical properties. As we see in Figure 1.1, in nature, the colour iridescence of the wing of the butterfly is a result of light interference at the wing surface[1-2], and super adhesion of the foot of gecko is due to the integration of van der Waals force of numerous spatulas to the wall[3-5]. The integration of nanomaterials is first inspired by nature and has been extensively studied with different architectures.

Integrating nanomaterials with other materials, especially with substrates when fabricating nanomaterial-based devices, would considerably influence physical properties of nanomaterials, such as electrical, optical, thermal and magnetic properties. This is primarily reflected when the nanomaterial is thin in its thickness, especially down to atomic thickness such as graphene. For example, strain and doping could be easily introduced to graphene while attaching to a substrate. By lifting the graphene from the substrate to some distance, another possibility may be opened: light interaction between graphene and substrate has been a suitable protocol for photo-thermal self-oscillation.

Meanwhile, the integration of nanomaterials would result in emergent phenomena beyond our expectation, even if it is based on a simple combination of different materials. This has recently recognized in experiments using novel materials having memristive properties has to be more carefully and thoroughly investigated. For example, self-assembled memristive nanowire networks have been suggested to have many parallels with the biological brain and to emerge interesting electrical and dynamical properties. In more details, by designing the crossing points between nanowires to have memristive properties, and by integrating a vast number of such crossing points, a collective interplay between the crossing points occurs and results in a modification of the inner structure as well as electrical state which contributes to a change of electrical resistance of the entire network. Since self-assembly of nanomaterials takes fewer fabrication costs, if we can find and utilize emerging and useful properties out of such self-assembled systems, it will be highly desirable for future application.
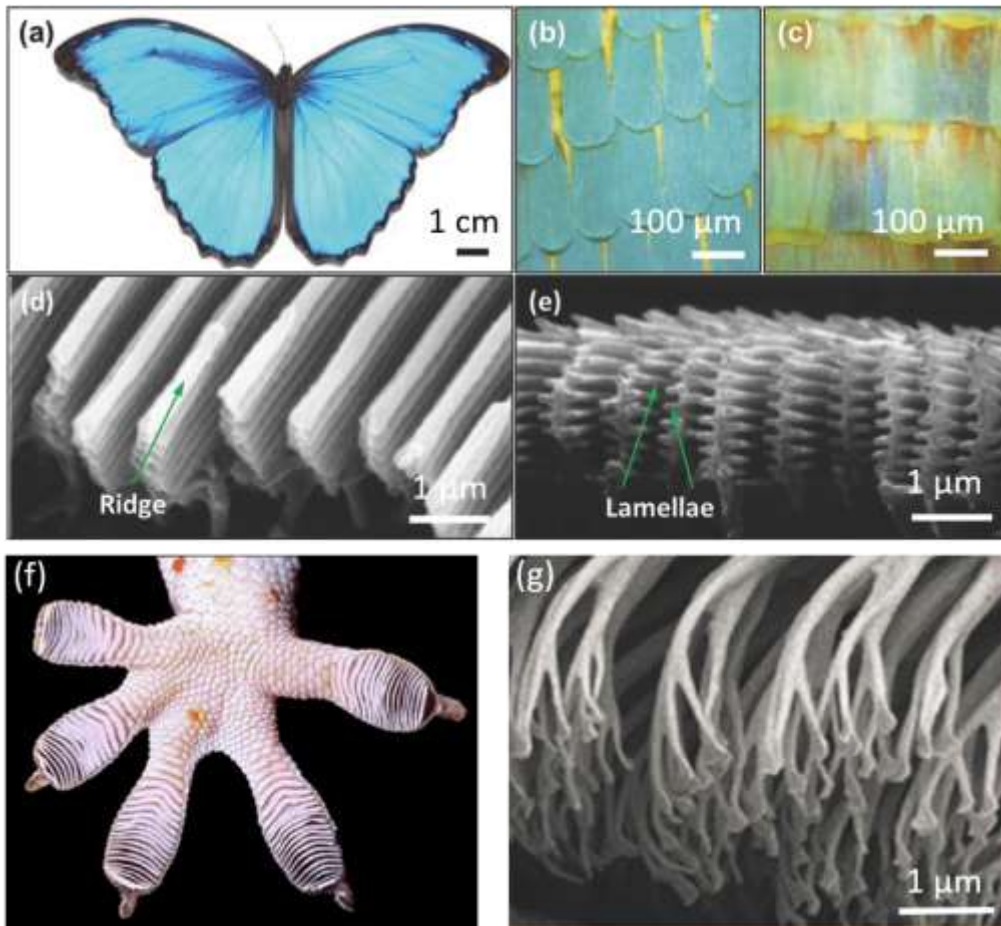
Figure 1.1. Integrated nanomaterials in nature. (a-e) Nanostructure of Morpho butterfly[2]. (a-c) Photographs of Morpho didius butterfly showing blue iridescence. (d) Scanning electron microscope (SEM) image of a male butterfly Morpho didius showing nanostructure. (e) A cross-sectional view of (d). (f-g) Nanostructure of gecko foot[4]. (f) Photograph of a gecko foot. (g) SEM image of the gecko toe pad which contains numerous antennas called spatulas.

1.2 GRAPHENE-INTEGRATED SYSTEM

1.2.1 History of graphene

Graphene refers to a monolayer of graphite, and Boehm and his colleagues initially introduced this term in 1986 from the combination of word "graphite" and suffix that refers to polycyclic aromatic hydrocarbons[6]. In 1946, Phil Wallace derived the electronic band structure of graphene in order to understand the electronic properties of bulk graphite and its unusual semi-metallic behaviour[7]. Since then, graphene has been a toy model to explain various questions of quantum electrodynamics [8-9]. However, experimental isolation of graphene had not been achieved[10-11] until 2004, when Professor A. K. Geim and his group successfully isolated the one-atomic-thick carbon layer by micromechanical cleavage from highly oriented pyrolytic graphite (HOPG)[11]. The top layer of graphite crystal was removed by Scotch tape and then pressed against the SiO_2 substrate. As the adhesion of the bottom graphene layer to the substrate was more substantial than that between interlayers of graphite, it is possible to transfer monolayer graphene onto the SiO_2 substrate. This technique is unique from previous studies and avoids coagulation into islands or three-dimensional (3D) carbon structures[12]. One can also notice that graphene film produced by cleavage is very stable under ambient temperature—not reactive with air or moisture. Inside graphene, each carbon atom has three nearest neighbour atoms, interacted with a strong σ bond and half-filled π bond and form Dirac cone valley in its Brillouin zone.

As the first two-dimensional (2D) material ever made, studies on graphene are unprecedented, including fabrication, chemical properties, physical properties and applications. Graphene shows outstanding intrinsic properties, yielding high electrical conductivity[11, 13], high thermal conductivity[14-15] and high elasticity[16]. It is impermeable to any molecules[17] and has broadband absorption covering the far-infrared to ultraviolet range[18]. By now, it is possible to obtain large scale and high-quality graphene sheet by mechanical exfoliation[19], liquid-phase exfoliation [20], and chemical vapour deposition (CVD)[21-23]. With its outstanding electronic properties and mechanical properties, the graphene-integrated system has broad applications in electronic device[24-25], such as gas sensors[26], radiofrequency electronics[27], flexible electronics[28-29], nanoelectromechanical system[30] and optical communication[29, 31], but its performance is primarily affected by the substrate which supports it. Strain and doping are frequently introduced in graphene from substrate[32], causing wrinkles and energy loss through electron scattering[33-34]. Substrate engineering has been a primary task in the graphene-integrated system for high-performance electronic device[35].

1.2.2 Substrate engineering in graphene-integrated system

Substrate engineering in graphene-integrated system covers topics from graphene growth to device fabrication. In the process of graphene growth, CVD method has been the primary technique to produce large and uniform high-quality graphene sheet with no or negligible defects[36]. Such a method involves carbon-based gas molecules (precursor) and substrate to allow graphene to grow epitaxially in a hot reaction chamber. The surface properties of the substrate primarily define the reaction temperature and the type of reaction. Metallic materials, such as copper[37-41],nickel[42-44], copper/nickel alloy[45-47] and silicon carbide[48-50], usually require a growth temperature between 300°C ~ 600 °C. To obtain a lower growth temperature is one of the main directions in graphene growth. At the same time, a dielectric substrate is essential for graphene electronic application. Transfer-free synthesis of graphene film, which retains the high quality of the film and reduces the device

preparation process, is favourable in industry. There is progress working with SiO_2 [51] and glass[52]. Fujita et al. reported graphene CVD temperature down to 50 °C on sapphire and 100 °C on polycarbonate, assisted with molten gallium as catalysts[53], which reduced the reaction to near room temperature regime.

Depending on the final target of application, researchers have integrated graphene into different architectures, which require micro/nanofabrication of graphene with a top-down approach on different substrates. In the approach to the field-effect transistor (FET), graphene films on standard SiO_2 substrates are highly disordered, presenting characteristics that far inferior to a suspended graphene[13]. Substrate engineering focuses on identifying dielectrics that allow a substrate-supported geometry while retaining the high carrier motilies as a supported one. One breakthrough discovery is that the carrier density of graphene on the atomically smooth h-BN surface is extremely high[24]. The lattice constant of h-BN is similar to that of graphene, which remarkably reduced energy loss during electron transportation. The work gives a new angle in substrate engineering even for other 2D materials.

Beside the substrate-supported architecture, graphene on the patterned substrate has potential applications for the future nanoelectromechanical system (NEMS). The suspended graphene can vibrate at a high resonant frequency which is tuneable over a wide range with moderate applied voltages. An integrated system like the graphene drum has been used as a mechanical resonator to detect pressure[54], molecule absorption[55] and operate in high frequency for energy-efficient radio frequency signal processing and communication[56-58]. It is also the most straightforward system to study some fundamental problems within the frame of interaction, such as light-matter interaction, for example, photo-thermal self-oscillation, laser cooling[59] and tuneable phonon-cavity coupling[57-58].

The existence of substrate, with no doubt, to some extent suppress the intrinsic properties of the graphene. However, with the substrate engineering, graphene-integrated systems demonstrate outstanding performance which could not be achieved by individual graphene sheet. Meanwhile, there are vast possibilities of physical modifications of graphene by posing different substrate architectures and should be more extensively studied.

1.3 MEMRISTIVE NANOMATERIALS

1.3.1 Introduction of memristive nanomaterials

Memristive behaviour stands for a device on its IV characteristics showing hysteresis loop, indicating a changed internal structure or electronic state in the device under external power application. An observation of memristive behaviour can trace back to two centuries ago when Sir Humphry Davy used voltaic pile for demonstrating the effect of large current on a generation of sparks[60-61] between two charcoal cylinders [62-63] and found that ionization and deionization take place depending on previously applied current[64]. Similar characteristics also appeared on tungsten filament, high pressure-vapour lamps, low-pressure mercury tube, discharge tubes and sodium tubes afterwards[65]. Also, magnetization and polarization of materials would be well-known examples of similar memristive behaviours. However, in the following discussion, we describe and discuss about resistively memristive behaviours.

The development of memristive nanomaterials has roughly gone through three stages, and each period has its representative functional materials. The first period start from the 1960s to 1980s, some unconventional electrical properties had been observed and reported on many metal/amorphous oxide film/metal device. The observation of memristive behaviour in nanomaterials was firstly reported in 1962 by Hickmott [66] on a group of amorphous oxide films ($Zr/ZrO_2/Au$, $Al/Al_2O_3/Au$, $Ta/Ta_2O_5/Au$, $Al/SiO_x/Au$, $Ti/TiO_2/Au$), showing resistance switching and also an unconventional negative resistance on their IV characteristics. After that many other amorphous oxide films, to list some, NiO, Al/SiO/Au, Al/Al_2O_3/metal (Ag, Mg) [67-73], have shown similar properties and the underlying mechanisms had been intensive discussed[69, 72-78]. Nevertheless, due to the poor controllability, there is a lack of comprehensive understanding of such resistance switching. At the same period, integrated circuit technology was developing rapidly, therefore study on memristive materials had reduced attention. Until the 1990s, as the flash memory with a floating gate structure faced the physical size limit, the application of the resistive switching materials in the storage field received renewed attention, the second phase of research boom began. With $Pr_{0.7}Ca_{0.3}MnO_3$(PCMO) discovered in 1997 by Asamitsu et al. [79]as the representative, the research on resistive switching nanomaterials mainly focused on transition metal oxide, such a manganite and titanate with complex perovskite structure[80]. In 2000, Liu et al. [81] and Beck et al. [82] respectively found reversible and reproducible non-volatile resistance switching behaviour in PCMO film and Cr doped $SrZrO_3$ film, showing the great potential of resistive switching in novel non-volatile memory. Since then, diverse materials emerged as resistance-switching memory, such as binary transition metal oxides(AlO_x[83], TaO_x[84], ZrO_x[85-86], CuO_x[87-88]), electron-ion mixed conductors (CuS[89], Ag_2S[89-90]) and organic nanomaterials (AIDCN[91-93], Alq3[94], PEDOT:PSS: NaCl/6T-co-PEO [95]).

The last period of research boom started in 2008 when Strukov et al. [96] from HP laboratory published a paper named "The missing memristor found", in which a physical model successfully demonstrated the hysteresis loop observed on TiO_2 nanodevice. Strukov's work for the first time connected the resistance switching behaviour with a theoretical model[97]. In the following years to now, more and more materials and device (TiO_x[98], GeS_x[99-100], Ge_2Sb_2Te[101], AgI[102-103], HfO_x[104-105], TaO_x[106], $SrTiO_x$ [107]) has been included into memristive material and extensively studied both

experimentally and theoretically, and the relevant physical mechanism of memristive behaviour and designing applications of memristive materials has been rapidly deepening and developing.

1.3.2 Background of redox-based memristive nanomaterials

With the rapid growth of information technology for big data processing and storage, there is an urgent need of non-volatile resistance switches with tuneable resistance states, high endurance, fast switching speed and low power consumption. Memristive nanomaterials are promising candidates owing to its unique characteristics. The driven force of the resistance switching can be one of four mechanisms: electrochemical reaction (redox and ion migration) [108-109], phase changes [110-115], tunnel magnetoresistance[116-126] or ferroelectricity[127-129]. Among them, the redox-based memristive device has attracted enormous attention owing to its excellent chemical and physical controllability and scalability.[130]

In this section, we introduce the background of the redox-based memristive device and provide general knowledge and understanding of the switching mechanism and switching modes. Memristive devices are generally in the form of metal/insulating layer /metal (M-I-M) structure, where the metal electrode, the insulating layer or their interface can contribute to the change of resistance state (Figure 1.2 a). The switching mode can be bipolar or unipolar, and if devices can work with both polarities, they are called nonpolar devices. Bipolar switching requires opposite voltage polarities for switching ON and OFF, respectively, whereas unipolar and nonpolar switching does not have such a requirement, as shown in Figure 1.2 b and c.
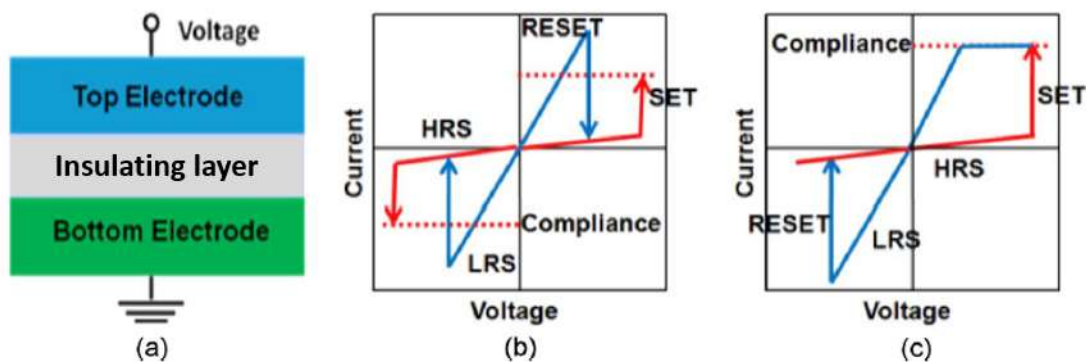
Figure 1.2. Schematic of M-I-M structure for the memristive device (a) and possible IV curves, showing two different switch modes: (b) unipolar and (c) bipolar.

Redox based memristive device can be either cation-based or anion-based one depending on the active element for the resistance switching of the device. In many cases, for an insulating layer terminated with inert electrodes, anion ion can be easily reduced under the application of a sufficient electrical field, forming a conductive channel in between electrodes. All type of transition metal oxide can be classified as anion-based memristive materials, and few non-oxide memristive materials also have been found in nitrides, telluride and selenide. Figure 1.3 shows the filament growth behaviour and the corresponding IV characteristics for transition metal oxide-based memristive device. Figure 1.3a takes from the case of a Pt/TiO$_{2-x}$/TiO$_2$/Pt device[131], in which the oxygen ions drift form oxygen-rich region to the oxygen-deficient region under an electrical field. Since the oxygen-deficient region has high conductivity, device conductance switches form low to high after an oxygen vacancy channel

is formed in the oxide layer. Then if an opposite polarity of the voltage is applied, oxygen ions move back, causing the device conductance to reset to low state. Therefore, its IV characteristic exhibits bipolar switching behaviour. The redox reaction formula can be written as:

$$O_O \rightleftharpoons \frac{1}{2} O_2(g) + V_O^{\cdot\cdot} + 2e'$$
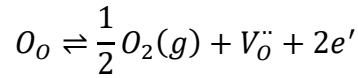
where O_O and $V_O^{\cdot\cdot}$ denote oxygen ions on regular lattice sites and oxygen vacancies, respectively. The switching picture in Figure 1.2a requires an asymmetry of oxygen distribution, needing careful consideration during device preparation. If simple polycrystalline oxide materials replace the insulating layer, the devices usually exhibit a unipolar switching behaviour, as shown in Figure 1.3d for a Pt/polycrystalline Ni/Pt memristive device[132]. In this case, localized oxygen vacancy sites which naturally exist at defect positions seeding the formation of oxygen vacancy channel. For this type of memristive device, the required switching voltage reduces, and the device resistance state can only be reset by posing sufficient temperature such as large Joule heat. In both thermal dominated or electrical field dominated switching mode, we can see once the device switches to ON state, its conductance state stays at a high value until a reset process, indicating a non-volatile memory switching nature of the anion-based memristive device. Later we will introduce a group of memristive device lose its conductance state at low voltage bias even after switching to ON state, known as volatile threshold memristor.

Despite properties of the materials in a memristive device, size of electrode, the thickness of the oxide layer, power of the electric field and Schottky barrier at the electrode/insulator interface also affect the formation of the conductive filament and change the IV characteristics in the real device. In all cases, four main driving forces work independently or together to influence atomic motion or rearrangement in memristive nanomaterials: electric potential gradient (field), electron kinetic energy, species concentration gradient and temperature gradient. The microscopic picture of how exactly these factors drive the mobile species to actuate a particular type of switching is still under debate. Therefore, experiments that could visualize the switching in real-time and at nanoscale resolution could be precious.[133] The conductive oxygen filament formation of an anion-based device was first confirmed by conductive atomic force microscope, which demonstrated insulate-metal transition of nano spots in single-crystalline $SrTiO_3$ under electrical field [88]. Later in a $Pt/TiO_2/Pt$ device, visual observation of a conical shaped Ti_4O_7 filament phase was taken under a scanning electron microscope (TEM) [134]. Further effort can be made by cooling the oxygen ions to speed down the quick and dynamical motion for detailed observation. A new technique which allows high-resolution observation at ambient condition is also urgently needed.
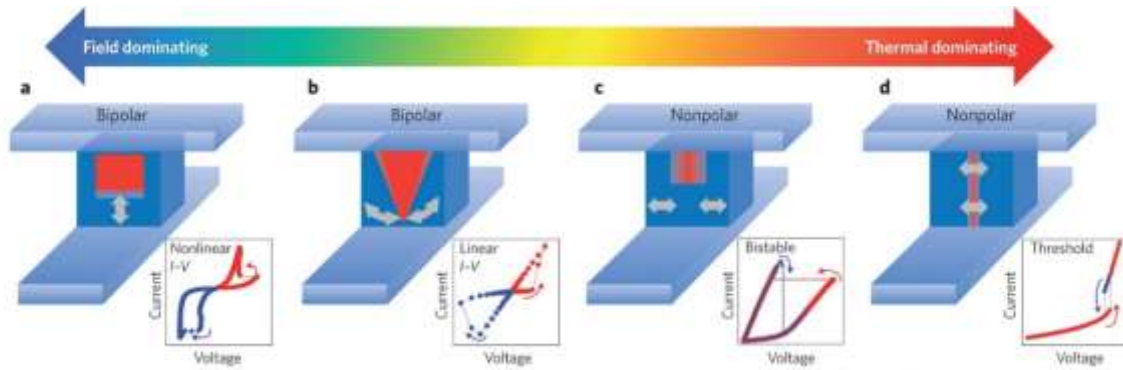
Figure 1.3. Simplified schematics of conduction channels (red) in insulating materials (blue) in four typical switching devices, in which both the electric field and Joule heating drive the switching. Inset to each schematic shows typical IV characteristic of bipolar nonlinear switching[131] (a), bipolar linear switching[135](b), unipolar non-volatile switching[136] (c) and unipolar threshold switching[132 137] (d).[138]

For a cation-based filament, active metal electrode, for example, Ag or Cu, is integrated into the MIM structure. The metal atoms at the cathode can be easily oxidized as metal ions, transport to cathode along the electrical field and reduced on the way to or at the cathode. Depending on the ion mobility (μ) and the redox rates (Γ^i), the cation-based filament has diverse morphologies. Yang at el. [139-140]extensively studied the electrochemical dynamics of nanoscale metallic inclusions in different dielectric and observed four different morphologies of the filament formation, as shown in Figure 1.4. When both μ and Γ^i are high (Figure 1.4a), metal ion easily can transport to the cathode, resulting in a cone-shaped filament growth from the cathode metal electrode. This type of filament growth has been widely observed on a cation-based device with an insulating layer which contains enormous anions for redox action [108, 141-142], for example, Ag_2S based atomic switch, Ag/Cu electrode with a solid electrolyte. In contrast, if both μ and Γ^i are low (Figure 1.4b), metal ions easily reach the critical nucleation conditions inside the dielectric and migrate to metal clusters from the anode side, further filament growth in the form of cluster displacement via repeated splitting-merging processes. On Ag/amorphous Si/Pt device researchers have observed such discontinues metal clusters[143]. The filament growth occurs with a slightly different manner if redox rate Γ^i is high while μ is still low, as shown in Figure 1.4c. Large amounts of metal ions will be reduced in the dielectric, forming a big cluster and move towards the anode. In the last case for metal ions high μ and low Γ^i (Figure 1.4d), metal ions could fast transport to the anode but have a limited amount. Therefore nucleation predominately occurs at the edges with high electrical field strength, leading to a dendrite-like filament growth towards the anode. For Ag ions transport in sputtered SiO_2 films or water[144], researchers observed such dendrite-like branches.
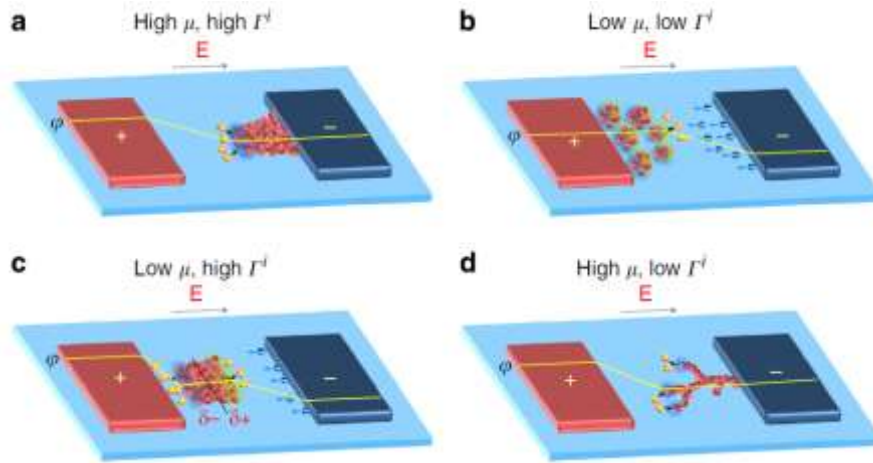
Figure 1.4. Qualitative model showing four different filament growth dynamics governed by kinetic parameters.[140]
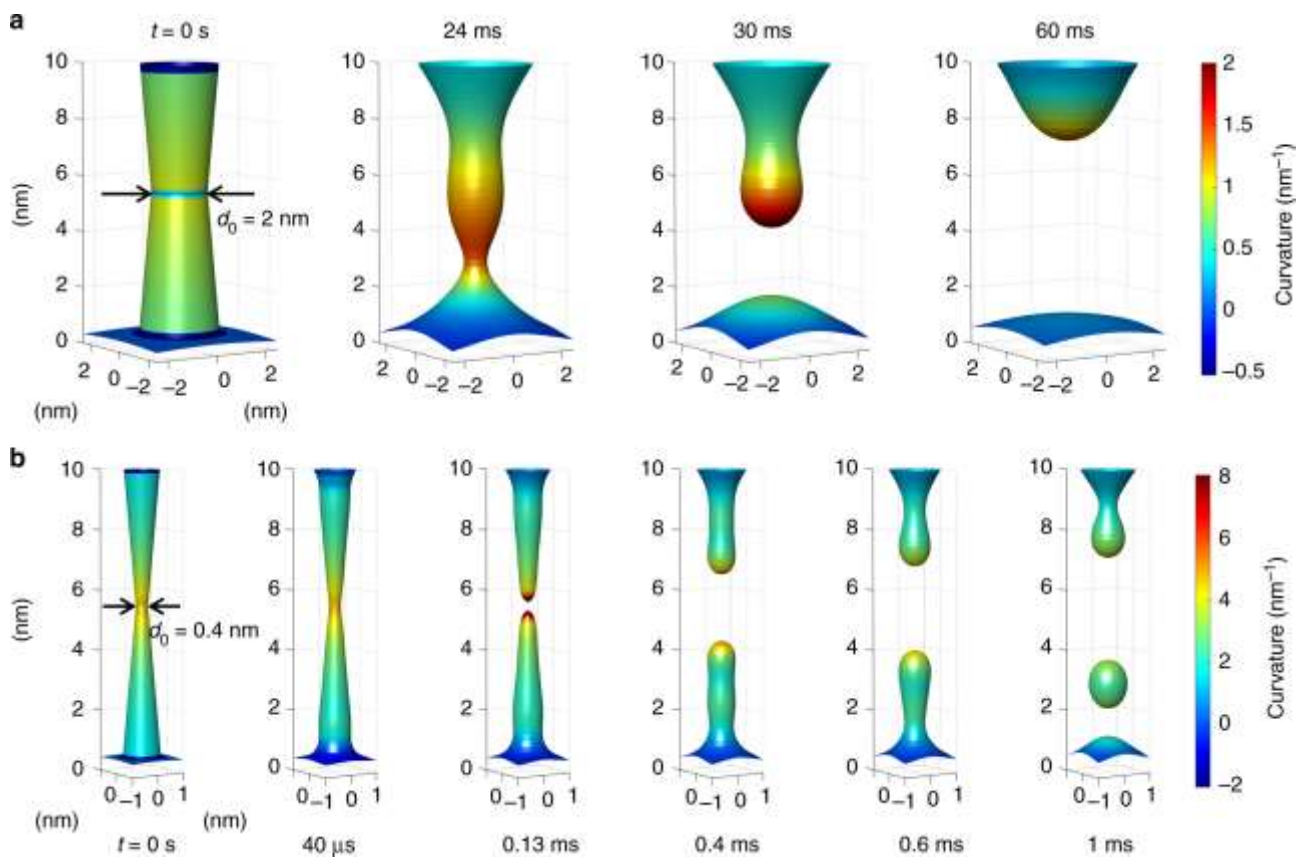
Figure 1.5. Morphological changes induced by surface diffusion. (a) Simulation results of the rearrangement of a silver conductive filament with initial diameter $d_0 = 2$ nm at increasing times, (b) Same as a, but for a conductive filament with an initial diameter $d_0 = 0.4$ nm. [145]

As we can see, even for the same Ag as the active metal electrode, in the different insulating material, the filament growth dynamic differs. The material properties, local electrical field, ionic speed could significantly affect the final morphology. However, a transition between different filament growth dynamics could take place by tuning one of those factors and can be reflected in the IV characteristic. Though in all action-based memristive devices, there exhibits bipolar switching

behaviour due to the polarity dependence of the metal oxidation[146], researchers noticed that non-volatile memory switching usually appears in a system with high ion mobility. In contrast, a threshold switching usually takes place in the system with low ion mobility, where current flows between neighbour in a tunnelling mode. Sun et al. observed a conversion between memory switching to threshold switching in Ag/SiO₂/Pt device, where the local electrical field was tuned by increasing the thickness of the SiO_2 layer[147].

Compared with the oxygen vacancy channel in the anion-based memristive device, the metal filament in the cation-based device has shorter retention time. Once the electrical filed is removed or reduced, in order to reach a chemical/physical equilibrium of the system, the metal atoms start to dissolve in the dielectric to minimize the surface energy. Depending on the size of metal aggrgates[148], surface energy at the metal/dielectric interface and temperature state, there exhibits different lifetime of the metal filament and the volatility of the resistance state. Wang et al. [145] studied the lifetime of the Ag filament with different size with molecular dynamics simulation method, as shown in Figure 1.5. For a filament of considerable size, it is gently deteriorated simultaneously to one side of the electrode, demonstrating a non-volatile switching behaviour on its IV characteristic. On the contrary, if the filament size is reduced by five times (Figure 1.5 b), a fast rapture occurs, and the filament lift time is reduced about 150 times.

1.3.3 Theoretical models for memristor

In 1971, Leon Chua published a theoretical work and introduced the concept of 'memristor', which is short for memory resistor [97, 149]. Memristor (M) follows a nonlinear functional relationship between charge (q) and flux (φ), $= Mdq$, taken as the forth fundamental passive circuit element along with resistor, capacitor and inductor (Figure 1.6). Later in 1976 he and his student Kang generalized the concept of the memristive system, introducing a state variable w [149]. Two equations can describe its nonlinear dynamic, a quasi-static conduction equation connecting voltage and current across a device and a dynamical equation:

$$v = R(w, i)i$$
$$\frac{dw}{dt} = f(w, i)$$

In the following 40 years, many nanosystems had shown similar resistance switching behaviour [90, 150-153], but a direct relation to memristor or this physical model did not present. In 2008, Strukov et al. proposed a physical model based on Chua's equation and successfully reproduced the hysteresis IV curves of a resistance switch[96, 154]. Since then, Chua's memristor model has been widely accepted and used to elucidate different resistance switching behaviours.[155-156]

The physical model proposed by Strukov et al. [96] was for a two-terminal electrical device to modulate the current transmission based on an atomic rearrangement. In this model, a thin TiO₂ film of thickness D sandwiched between two metal electrodes (Figure 1.7). The total resistance of the film is determined by two variable resistors connected in series, corresponding to regions with a high concentration of dopants (has low resistance R_{on}) and low dopant concentration (high resistance R_{off}) respectively. With the application of an external bias v(t), the boundary of two regions will move by causing the charged dopants to drift. The dynamical movement in the film thus leads to a change of total resistance. It can be described by:

$$v(t) = \left(R_{on} \frac{w(t)}{D} + R_{off} \left(1 - \frac{w(t)}{D} \right) \right) i(t)$$

$$\frac{dw(t)}{dt} = \mu_v \frac{R_{on}}{D} i(t)$$

where μ_v is the average ion mobility. The model well reproduced the hysteresis as in the experimental IV curve.
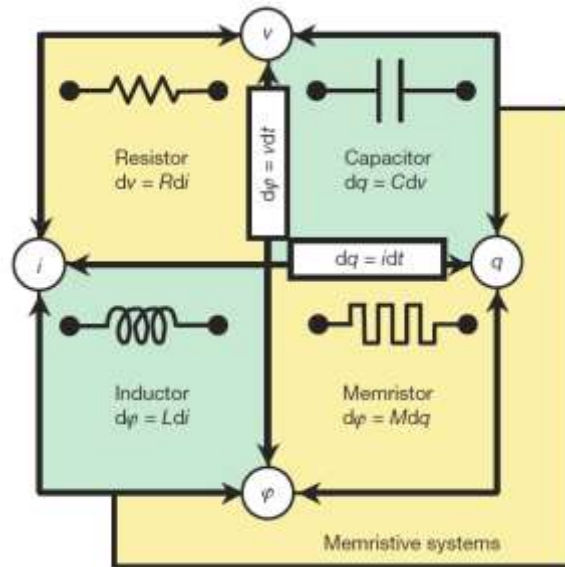
Figure 1.6. The four fundamental two-terminal circuit elements: resistor, capacitor, inductor and memristor, proposed by Leo Hua. [96, 154]
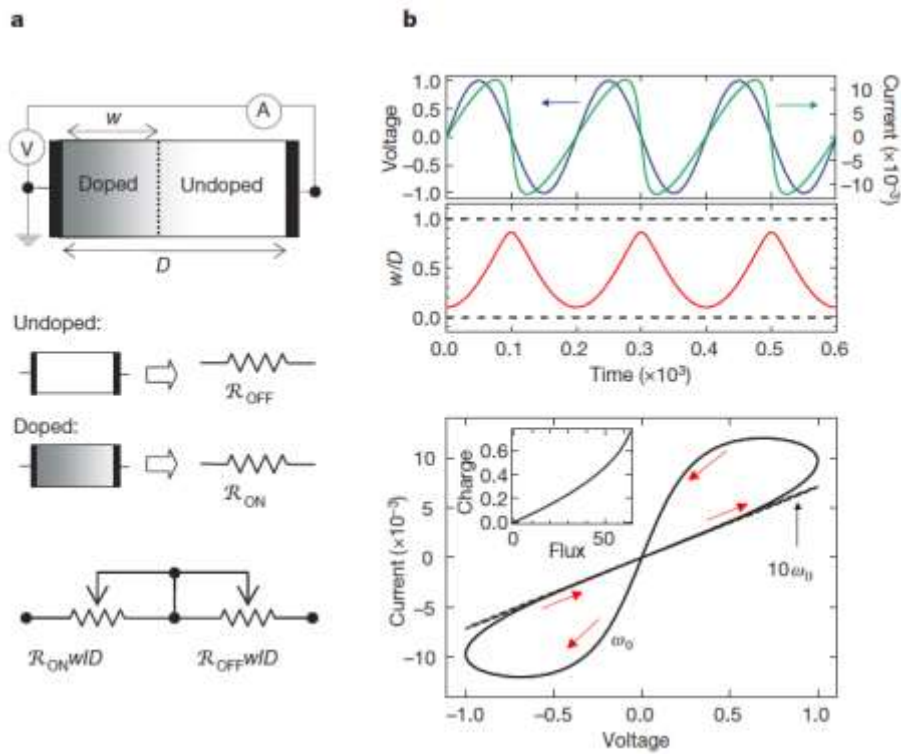
Figure 1.7. The coupled variable-resistor model for a memristor by Strukov et al. [96] *(a) Illustration with a simplified equivalent circuit. V, voltmeter; A, ammeter. (b) The applied voltage and resulting current as a function for time t for a typical memristor with* $R_{on}/R_{off} = 160$. *IV curve shows hysteresis loop.*

Strukov's model can be applied to typical bipolar memristor or the memory switching memristor. For a nonvolatile threshold switching memristor (mostly cation-based memristor), after removing the external bias voltage conductive filament has a limited lifetime and start to dissolve, a dissolution process should also be considered. [151-152] [157]Then equation can be rewritten as,

$$\frac{dw(t)}{dt} = \left[\mu_v \frac{R_{on}}{D} i(t)\right]\left[\frac{w(D-w)}{D^2}\right] - \tau(w-D)$$

where τ is a parameter related to filament dissolution and w is in range of (0,D).

1.3.4 Applications: approach, architecture and algorithm

Conventional non-Neumann architecture-based computer systems show significant advantages on mathematical calculation and permanent memory storage with large volume, compared with the biological brain. Data is transferred and processed in serial through the bus between memories with computing kernels, which dramatically slow down the information process speed and increase the designing complexity, especially for graphic process and more advanced recognition task. This data bus is known as von-Neumann bottleneck. In contrast, the nervous system in the biological brain is characterized as massive parallelism, distributed storage and processing, self-organization, self-adaptation and self-learning. Information process and storage are integrated, showing no clear boundary between the memory units and computing units. Therefore, building a new computer system like the biological nervous system is considered as an effective way to break through the von-Neumann bottleneck in future industry.

In this section, we first briefly explain the structure and the working principle of a biological neuron, which is the basic unit of information process in the biological brain. Then we will introduce the emergent interests of memristive materials toward the artificial brain and show some examples of the architecture and algorithms of memristive materials for artificial intelligence (AI).

The nervous system in the biological brain is composed of enormous neurons connected intricately (Figure 1.8)[158]. Each neuron cell consists of three components: the dendrites, the soma and the axon. It is surrounded with ion fluid with which different ions (mainly K^+, Cl^-, and Na^+) transfer through neuron cell membrane out and in to reach a dynamical concentration balance. When a neuron is at rest state, K^+ shows high concentration inside the neuron while Na^+ and Cl^- show lower concentrations, resulting in a potential difference (-10 ~ -100 mV) between the inside and outside of the neuron cell membrane, named rest potential. When the neuron is stimulated, the dynamical balance of the ion concentration breaks, generating an action potential which transfers along the cell membrane. An action potential is an electrical spike, typically has an amplitude of about 90~130mV and duration of 1-2 ms (Figure 1.8b, inset). The transmission position between neurons is known as synapse. In a typical synaptic transmission process (Figure 1.8), when an action potential arrives in the presynaptic (axon terminal), the depolarization of the terminal membrane causes voltage-gated calcium channels to open, which trigger the neurotransmitters to release from synaptic vesicles into the synaptic cleft and then captured by specific receptors in the postsynapse (dendrite terminal or soma). After this, Ca^{2+} channels will slowly close, and the neurotransmitters stop the release. If the second spike comes earlier than the Ca^{2+} channels close, more neurotransmitters release at the same time, enhancing the connection between neurons[159-160]. This spike-time-dependent plasticity (STDP) of the synapse is known as Hebbian learning rule, which was proposed by psychologist Donald Hebb in 1949 to describe an updated synaptic weight between neurons due to previous spike event.

The capture of neurotransmitter increases the membrane potential of the postsynaptic neuron, causing excitatory postsynaptic potential (EPSP). The EPSP can be integrated spatiotemporally from different sites of the neuron, and once it reaches a threshold value, neuron fires, accompanied with a generation of an action potential which further triggers the synaptic transmission to next neuron. Figure 1.9 shows how an action potential is generated in the postsynaptic neuron[161], showing an integrate and firing process. In 1943, Rosenblatt and McCulloch[162] proposed a computational neuron model which can mimic some feature of the integrate-and-fire process, paving the way for current AI algorithm. Neuroscientists believe the memory and cognition function in the biological brain are the

results of dynamical updated synaptic weight and complex connections between neurons, where neural codes hide in the spatiotemporal spikes in the whole system.
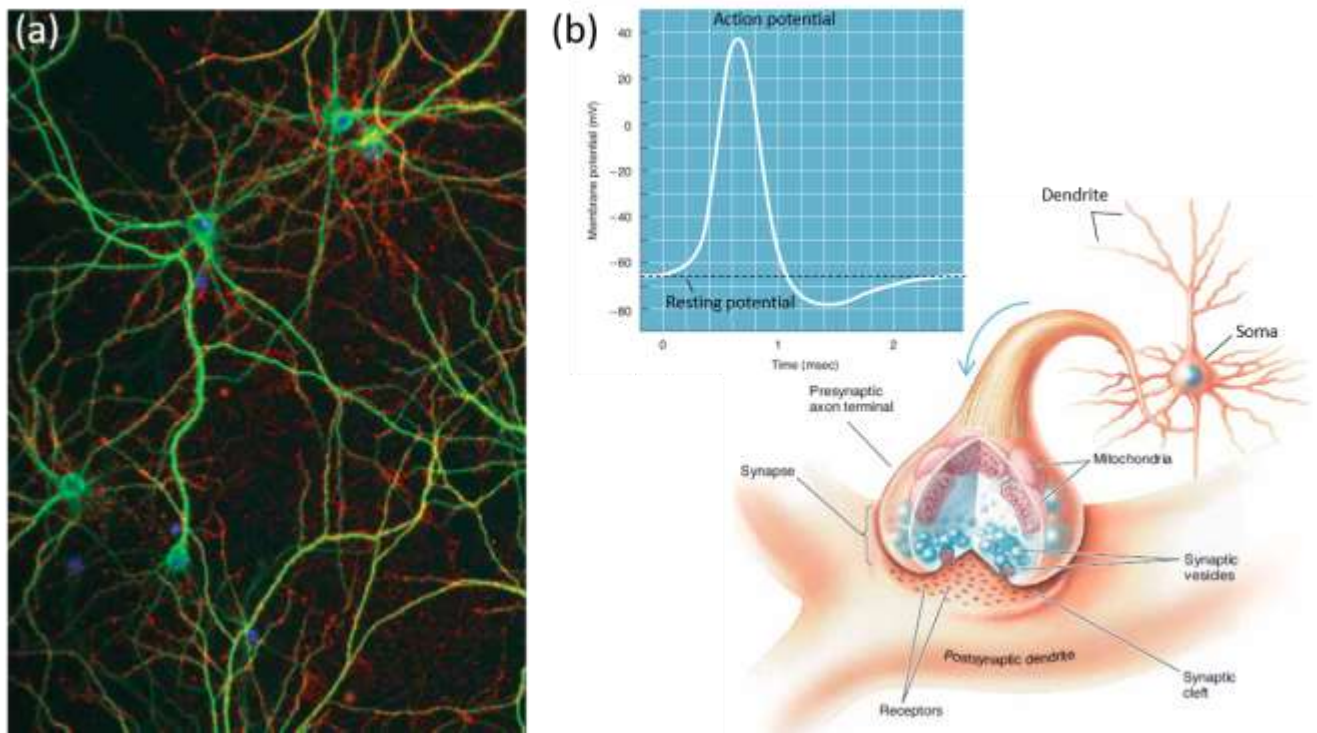
Figure 1.8.   (a) Neurons in the brain. (b) Illustration of neuron, synapse and the action potential.[158]
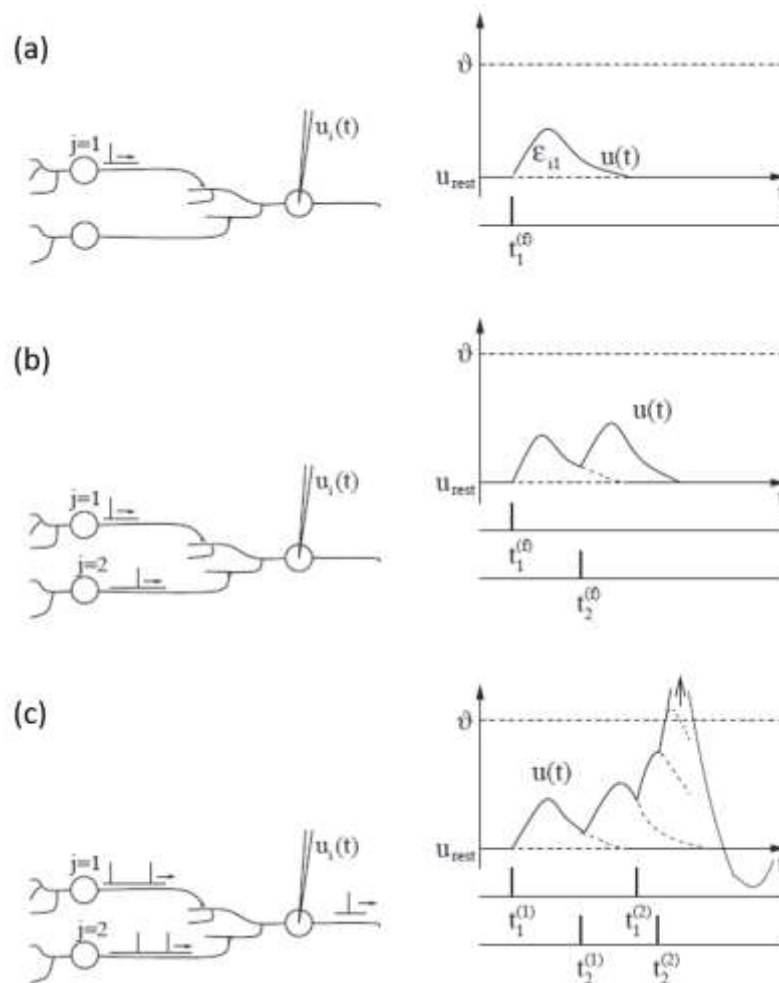
Figure 1.9. A postsynaptic neuron (i) receives input from two presynaptic neurons (j). (a) Only one presynaptic neuron fires, causing an excitatory postsynaptic potential (EPSP) in the postsynaptic neuron. (b) Two presynaptic neurons fires in sequence, inducing the accumulated EPSP. (c) Intensive spikes train from presynaptic neurons, firing the post neuron. $u_i(t)$: postsynaptic membrane potential, u_{rest}, rest potential, θ: membrane firing threshold.[161]

In the past decades, computer scientist has been committed to using non-linear circuits with very-large-scale integration to emulate the function of bio neurons or more advanced cognitive functions, boosting the development of soft AI systems such as Google's AlphaGo[163-164] and new AI accelerators with non-von Neumann architecture like the TrueNorth[165] launched by IBM, Loihi [166]from Intel and Tianjic[167] from the University of Tsinghua. A brief timeline of most significant discoveries in the field is shown in Figure 1.10 [168]. With the continuous improvement of the computational framework on the neuromorphic network, memristor as the ideal artificial synaptic component has been integrated into the neuromorphic chips, forming an artificial neural network (ANN) which can be trained and processed with knowledge in soft AI like machine learning. Based on the algorithm used behind the neuromorphic chips, there are two main architectures has been designed and studied for memristor integration: crossbar structure and random network.

Algorithms

● Understanding the brain   ● Enabling artificial intelligence

Hardware

● Neuromorphic computing   ● Computing efficiency

Current research

1940s–1960s

Hebb's rule: "Cells that wire together fire together"

Proposal of spiking neural models (Hodgkin & Huxley[13])

Perceptron invention for pattern recognition (Rosenblatt; McCulloch & Pitt[10])

Invention of the transistor at Bell Labs

Report by von Neumann[93] on building a computer, describing key aspects of today's von Neumann architecture

1970s–1980s

Fukushima's cognitron[138] (convolutional architecture)

Backpropagation learning (Rumelhart & Hinton[12])

Neuromorphic computing introduced at Caltech by Carver Mead[73]

Chua conceptualizes memristors as a missing passive component[105]

Use of floating-gate transistor as a synapse[115]

1990s

Proposal of spiking neurons as computational units for neural networks (Maass)

Long-term potentiation for memory

Spike-timing-dependent plasticity (Bi & Poo)

GPUs formally introduced as parallel computing processors

AER for on-chip spike communication

2000s

Neuromorphic vision sensors

DARPA announces SyNAPSE program for developing neuromorphic machine technology scalable to biological levels

ReSuMe and competitive STDP learning

Development of the SpinNNaker chip at the University of Manchester based on ARM mobile processors

Neurogrid chip development starts exploiting analog computations

HP Labs identifies the existence of the missing memristor proposed by Chua

2010s

Trained with GPUs, AlexNet wins the ImageNet challenge, fuelling the deep-learning revolution[6]

Digital 'Big Brain' chips such as True North[84] and Loihi[78]

Present

Using neural networks to understand brain mechanisms

Developing training algorithms for SNNs on available (or by modifying) machine-learning frameworks such as PyTorch and Caffe

Neuromorphic datasets from vision sensors

Extending SNN beyond vision tasks for active-learning environments

Boolean and analog in-memory computing with emerging and silicon and emerging technology

In situ implementation of synaptic efficacy and plasticity in RRAM, PCM and other crossbars

Algorithm–hardware co-design

Emerging devices that mimic neurons and synapses

Figure 1.10. Timeline of major discoveries and advances in intelligent computing, from the 1940s to the present. [147]

Figure 1.11. (a-d) Training scheme for pattern classification. (a) Input image. (b) Algorithm graph of a single-layer perceptron for classification of 3×3 binary images. (c) The input training pattern set. (d) The flow chart of one epoch with in situ training algorithm. (e) Memristor crossbar: Integrated 12×12 crossbar with an Al$_2$O$_3$/ TiO$_{2-x}$ memristor at each crosspoint. (f) An implementation of the single-layer perceptron using a 10×6 fragment of the memristive crossbar. (g) The evolution of output signals during training. If the output signal f$_i$ corresponding to the correct class of the applied pattern was larger than all other outputs, the classification was considered successful. [169]

Neuromorphic chips with crossbar architecture can take advantage of the current complementary metal-oxide-semiconductor (CMOS) fabrication platform, which aiming at large scale integration and operations, but they require high uniformity of constituting units. The algorithm used for neuromorphic computation is based on matrix multiplication, in which the conductance of each memristor, function as a synaptic weight, forms a transformation matrix to convert the input information into output cognition. According to the training scheme, algorithms for some machine learning networks can be adopted, such as convolutional neural networks and recurrent neural networks. Figure 1.11 shows a typical crossbar architecture used to implement a simple artificial neural network for pattern cognition.[169] Bottom electrodes of the memristive crossbar are the input terminals while three pairs of top electrodes function as the output terminals. The network is a single-layer perceptron, consists of an input layer, one hidden layer and one output layer, fully connected with 10×3= 30 synaptic weight (conductance of each memristor at the crosspoint). The outputs f_i (i=1,2,3) are calculated with an activation function:

$$f_i = tanh(\beta I_i)$$

$$I_i = \sum_{j=1}^{10} W_{ij}V_j$$

where β is a constant controlling the function's nonlinearity, W_{ij} is the synaptic weight and V_j is the input signal for the input electrode. Since in this memristive crossbar each synapse is implemented with two memristors, the synaptic weight is represented by a differential conductance:

$$W_{ij} = G_{ij}^+ - G_{ij}^-$$

where $G_{ij}^\pm$ is the effective conductance of each memristor. The training process requires repeated input and read to adjust the synaptic weights after each iteration. During one epoch, all patterns are presented one by one, and the output signals are recorded with external electronic. At the end of one epoch, the synaptic weights are updated by following a Manhattan update rule:

$$\Delta W_{ij} = \eta sgn \sum_{n=1}^{N} \Delta_{ij}(n)$$

with

$$\Delta_{ij}(n) = \delta_i(n)V_j(n)$$
$$\delta_i(n) = \left[f_i^{(g)}(n) - f_i(n)\right]\frac{df}{dI}|_{I=I_i(n)}$$

where η is a constant scales the training rate. $f_i^{(g)}$ is the target value of the i th output for the nth input pattern (set as +0.85 for correct pattern class and -0.85 for wrong class). As a result, N=30 patterns, the training patterns, have been classified into the three outputs by the crossbar chip.

In the above training process, the weight update calculation relies on the external calculation but not from a self-adaption process of the network itself. Chips work in a supervised way with pre-defined parameters and consume immense computing energy as the soft AI. With the increasing matrix size and layers, the entire process takes longer time than soft AI. To achieve an unsupervised learning scheme has been the main challenging for such crossbar architecture. On contrast, brain is self-adaptive and self-organized without pre-defined parameters. Though the mechanism underlying the brain's functionalities is still unknown, general concepts that neurons are connected randomly and spiking firing event happens in certain regions for specific tasks could inspire the development of a self-adaptive system. The random network, as the second architecture, has shown such possibility and attracted increasing attention in recent years.

Random networks emerge as a neuromorphic chip with the development of reservoir computing (RC), which is a type of spiking neural network (SNN) and based on the spike rate firing of neurons in a reservoir to transform the information (Figure 1.12) [170]. The firing condition also mimic the biological neuron condition, has models like leaky integrate-and-fire (LIF) model and Hodgkin-Huxley model (mimic the ion penetration process), and spike transfer only correlates to the presynaptic and postsynaptic neuron, following the Hebbian learning rule. However, in a physical random network device, information transfer is activated by potential bias has defined directions between artificial neurons. The synaptic weight, or the conductance at each connection node, is primarily influenced by the potential distribution in the whole network. Works on these have been concentrated on neuromorphic nanowire network; this part we will introduce in the next section.
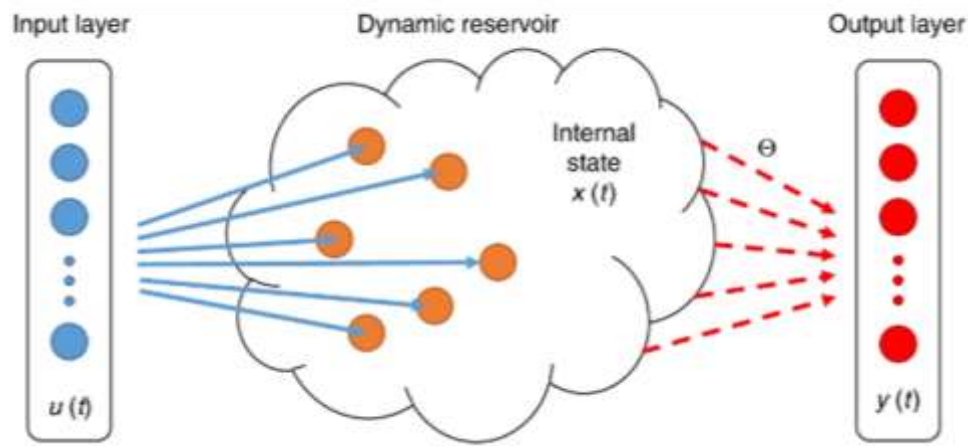
Figure 1.12. Schematic of a reservoir computing (RC) system, containing one input layer, a reservoir with internal dynamics and an output layer. The weight matrix Θ which connects the reservoir state x(t) and the output y(t) is the only parameter vector needs to be trained.[170]

1.3.5 Neuromorphic nanowire network

Neuromorphic nanowire networks are complicated ensembles of self-assembled nanowires whose interconnections have memristive properties similar as neurosynapses.[171-174] The local electrical properties at the interconnections contribute to the final functionality of the network, material science to synthesis nanowires with a metallic core and insulating shell has growing attention. Some candidates are metal oxide nanowire (NiO_x, CuO_x),[175-176] metal/organic nanowire ($Ag@PVP$)[177] and metal/dielectrics nanowire such as $Ag@TiO_2$.[146] Compared with conventional cross-bar architectures, though single memristive junctions are not individually controlled in such neuromorphic networks, high density of memristive junctions is achieved through high connectivity between nanowires[178].

In recent years, research has also revealed the rich interplay between the complex topology of the network and the memristive dynamics at the level of individual junctions.[178-182] These networks intrinsically have small-world topology after deposition[178-179] and emergent or self-organized dynamics appear by application of electrical stimulation,[180-182] where threshold or critical activation occurs after electrical pathway formation, causing a transition from a low-conductance state to a high-conductance state.[183] Moreover, this activation seems to be dominated by competing processes between possible current transmission pathways embedding the electrodes for providing electrical stimulation.[181-182] This has been proposed for an information processing device with auto-association between shared network pathways.[184] The studies on memristive interface properties and network systems, which mimic either topological or dynamical properties of neural systems, indicate that nanowire networks are promising for neuromorphic computing technology.

1.4   PURPOSE OF THESIS

In this thesis, I describe my PhD research work on two different integrated nanosystems. First, I introduce a graphene-cavity system where a graphene sheet is suspended over SiO_2/Si microcavity. I studied the optical interaction between the graphene sheet and the microcavity with Raman spectroscopy, and I demonstrate that concentric intensity oscillation rings appear over the graphene sheet. This is an example of a "designed" top-down approach to highlight the optical property of an integrated nanosystem. Then I focus on a self-assembled neuromorphic nanowire network, in which adaptive and memristive behaviours appear at nanowire-nanowire junctions, to show the exciting interplay between the topology of network with the memristive properties in the network. Owing to a "designless" self-assembled architecture, emerging properties are found in the neuromorphic network. Under the framework of sleep-dependent memory consolidation process in a biological brain, I proposed a demonstration of such process in this complex topological network and studied the connectivity revolution during the process at the level of individual junctions theoretically. Furthermore, I introduce research using lock-in thermography (LIT) to visualize current flowing pathways through the network. Dynamical formation and association of current pathways have been observed for the first time.

Chapter 2: Experimental methods

This chapter introduces the details about the experimental methods used in this thesis, including but not only the sample preparation and measurement methods. The first section lists the detail information of the sample preparation process handled by the author. For graphene/micro-cavity device, a wet transfer technique was present. Moreover, for the memristive network, a chemical synthesise process of Ag@TiO$_2$ nanowires and test device fabrication was introduced. In the second section, a brief explanation of the working principle of several frequently used measurement systems was given, including Raman spectroscopy, Lock-in Thermography and electrical measurements. The introduction is limited to the facilities primarily used in this thesis, and more detailed information like teat sample preparation is omitted.

2.1   SAMPLE PREPARATION

2.1.1 Graphene over the micro-structured substrate

In this thesis, we used single/double-layer graphene obtained by chemical vapour deposition (CVD) on copper foil. The as-grown CVD-grown graphene sheets[185] were transferred onto the SiO$_2$/Si substrate with pre-etched circular cavities by wet-transfer method[186].

We prepared SiO$_2$/Si substrates with pre-etched cavities of diameter 6µm, 9µm and 12µm and depth of 3.7µm. Figure 2.1 shows the process of sample preparation. First, a thin layer PMMA layer (MicroChem, 950,000 MW, 5 wt.% in anisole) was spin-coated (30 s @ 4000 rad/s) on top of the graphene/copper film to protect graphene layer and heated under 180 °C for 3 minutes. After that, the film was rinsed in a 0.02g/ml (NH$_4$)S$_2$O$_4$ aqueous solution for 3-4 hours to thoroughly remove the copper foil and then was washed with deionized water to remove acidic impurities. The remaining PMMA/graphene layer was then transferred onto the micro-fabricated SiO$_2$/Si substrate. The top PMMA layer was removed with acetone, and finally, graphene sheet over micro-patterned SiO$_2$/Si substrate was obtained.
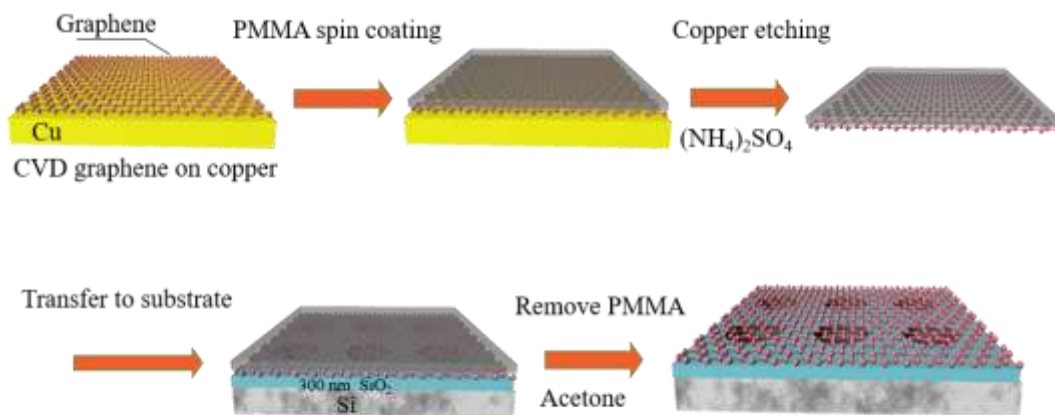
Figure 2.1. Schematic view of the graphene transfer process. CVD-grown graphene (pink layer) on copper foil (yellow layer) first spin-coated with PMMA (grey layer) and then transferred on Au (blue layer)/Si (textured layer) substrate after etching copper with (NH$_4$)$_2$SO$_4$ solution, then PMMA is removed by acetone.

2.1.2 Synthesis of Ag@TiO₂ nanowires and device fabrication

Ag@TiO$_2$ nanowires are prepared with two steps. First Ag nanowires were synthesised by a salt-mediated process[187], then a thin layer of TiO$_2$ polycrystalline was coated on the surface of Ag nanowire by the hydrothermal method using titanium tetrabutoxide as the titanium source[188-190].

In a standard process to synthesis Ag nanowire, 0.277g AgNO$_3$ was dissolved in 16ml EG at room temperature, while 0.757g PVP (M = 40000, Sigma-Aldrich) and 1.84 mg NaCl were dissolved in 32 ml EG at 120 °C under continuous magnetic stirring (600 rpm). After PVP/NaCl/EG solution naturally cooled down to room temperature, add it to the AgNO$_3$/EG solution drop by drop under vigorous stirring. Then the combined solution was allowed to mix for 2 mins and then transferred into a 50 mL Teflon-lined autoclave. The autoclave was heated at 160 °C for 7 hours and then naturally cooled down to the room temperature. The final solution was diluted in methanol (volume ration: 1:4) and centrifuged at 3000 rpm for 30 mins. After centrifugation, the supernatant which dissolved EG and NaCl was removed by syringe. Then methanol was added again. The purification process repeated three times more. The resulting Ag nanowires were dispersed into 12 ml ethanol.

To modify the Ag nanowire with TiO$_2$, 1 ml of as-prepared Ag nanowire solution was dispersed in a mixed solution of 2 mL ethanol and 15 µL titanium tetrabutoxide, respectively. The mixed solution then was transferred into the 50mL Teflon-lined autoclave. After sealing, the autoclave was heated to 150 °C for 10 hours then naturally cooled down to room temperature. The resulting supernatant was decanted, and the precipitate was washed with deionized water and ethanol with centrifuge for three times. The final nanowires were dissolved in method and sealed.

The experimental devices were prepared by spin-coating the Ag@TiO$_2$ nanowires on glass substrates with pre-deposited Au/Ti electrodes to form randomly connected networks. The electrodes were deposited on the glass substrates by maskless photolithography with the thickness of Au/Ti = 50nm /10 nm and width of 40 um. The distance between counter electrodes has two different sizes: 40 µm and 500 µm, for different measurements.

2.2   METHODS OF PHYSICAL MEASUREMENTS

2.2.1 Raman spectroscopy

Raman spectroscopy is a spectroscopic technique to observe the inelastic scattering when monochromatic light incidents on an object. It provides rich information on the chemical structures and physical forms to identify or qualify the substances in a whole range of physical states.

When monochromatic light (usually a laser beam) incidents on the object, electrons around the Fermi surface of the object could absorb photons and jump to a higher energy state (Figure 2.2)[191]. Some experience the infrared absorption, jump to a high energy state then stay excited. But mostly excited electron will return to lower energy state, it will emit a photon with the same frequency or different frequency. The middle energy states are called virtual energy state. For a process to emit a photon with the same frequency, the scattering is elastic scattering, called Rayleigh scattering. For a process to emit a photon with different frequency, it can have either higher frequency or low frequency, the scattering then is Anti-Stokes or Stokes, respectively. Both are inelastic scatterings and give information about the electronic state of the material. Therefore they are Raman active scatterings.
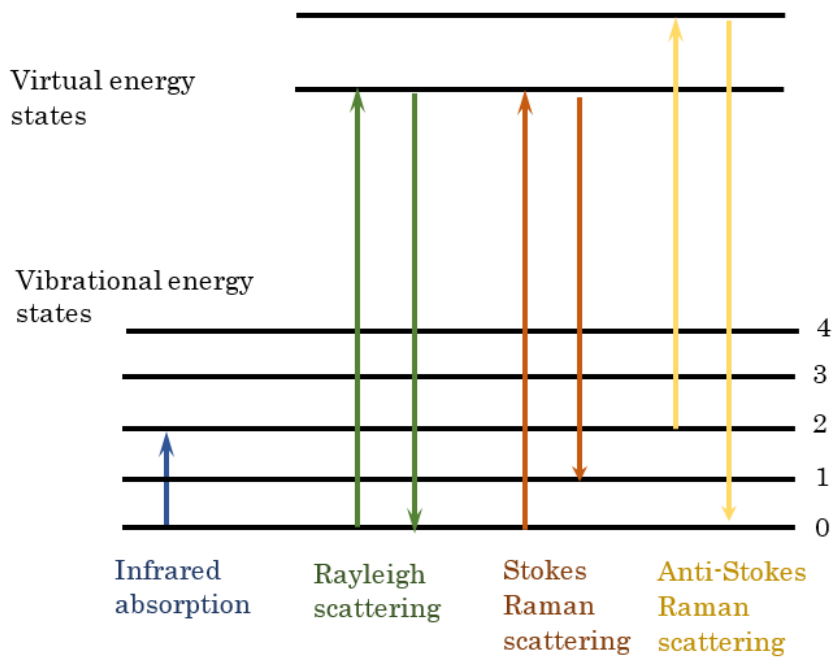
Figure 2.2. Excitation and relaxation of the electron under light irradiation, resulting in infrared absorption, Rayleigh scattering, Stokes and anti-Stokes inelastic scattering.

A Raman system consists of four major components: laser source, sample illumination system and light collection optics, optical filter and detector (Figure 2.3). Laser source generates a beam of very intense monochromatic light. It usually is in the ultraviolet, visible or near-infrared range, depending on the properties of the test materials. The sample illumination system and light collection optics are integrated into an optical microscope. When the laser beam is ejected from the laser source and incidents on the sample, light scattered from the sample surface. The scattered light is collected with the lens and sent through an optical filter to exclude the elastic scattering light. A commonly

used optical filter is known as Notch filter, which is a band-stop filter to reject signals in a specific frequency band, here, the light in the same frequency as the laser source is filtered. After scattered light passes through the Notch filter, only Raman active scattering signal remains and is collected by a CCD detector (commonly used) and sent to a computer for final analysis.
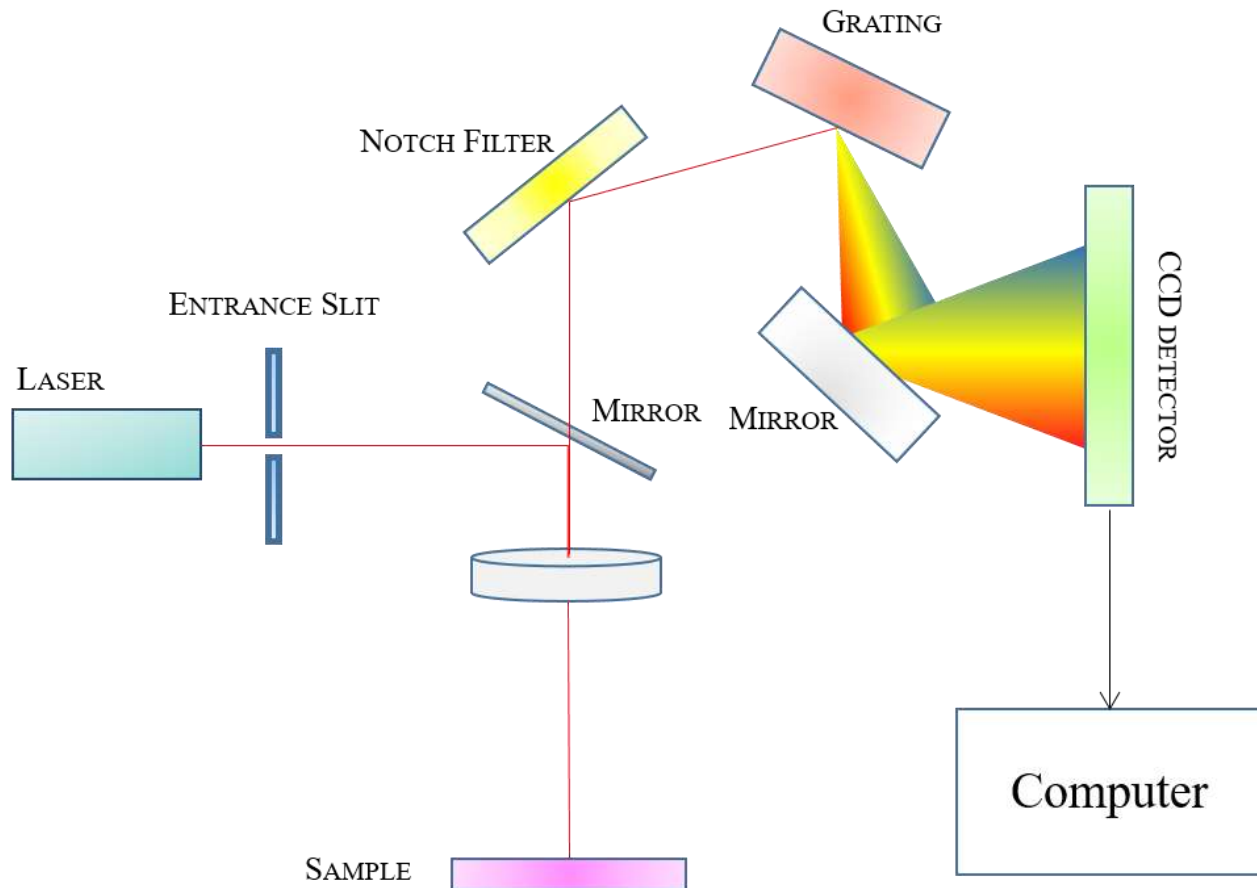
Figure 2.3. Set-up of Raman spectroscopy.

2.2.2 Lock-in thermography (LIT)

Lock-in thermography (LIT) is a form of dynamical infrared (IR) thermography which provides a time-dependent thermal image of an object.[192] It has a high signal-to-noise ratio, built-in compensation for non-uniform light radiation and capability of depth information and high noise suppression. With the rapid development of highly sensitive IR cameras, LIT as a rapid and non-destructive test method has an extensive application on the electronic component, for which localized device fault and material failure can be evaluated.

Figure 2.4 shows the general scheme of a LIT system integrated with a power supply for investigating the electronic component. Depending on the purpose of the test, the power supply could be electrical stimulation, light irradiation or magnetic field. The two central units of a LIT system is the lock-in signal correlation system and the IR detection system. The generated pulsed heat radiation is collected by the IR camera and sent to the lock-in correlator.

Each body at finite temperature would spontaneously and continuously emit some electromagnetic wave, in name as thermal radiation. The magnitude of the thermal radiation M_λ is called the spectral radiance, describing the unit emission power at a specific light wavelength. The

spectral radiance of a black body as a function of wavelength λ at thermal equilibrium is given by Planck's law[192]:

$$M_\lambda(T) = \frac{2\pi hc^2}{\lambda^5}(e^{\frac{hc}{\lambda k_B T}} - 1)^{-1}$$

where h is Planck constant, c is the velocity of light, k_B is Boltzmann constant, and T is the absolute temperature in Kelvin. Figure 2.5 shows the spectral radiance at a different wavelength. The noticeable radiation starts at 3 µm and reaches a maximum around 10 µm, covering a broad infrared light wavelength range to above 30 µm. At high temperature, it shows higher radiation at all wavelength. In a real object with different materials, the emission efficiency varies, thereby at the same room temperature the total radiation varies. Thereby thermography can also be used to evaluate the boundary of materials, for example, components distribution in an integrated circuit.
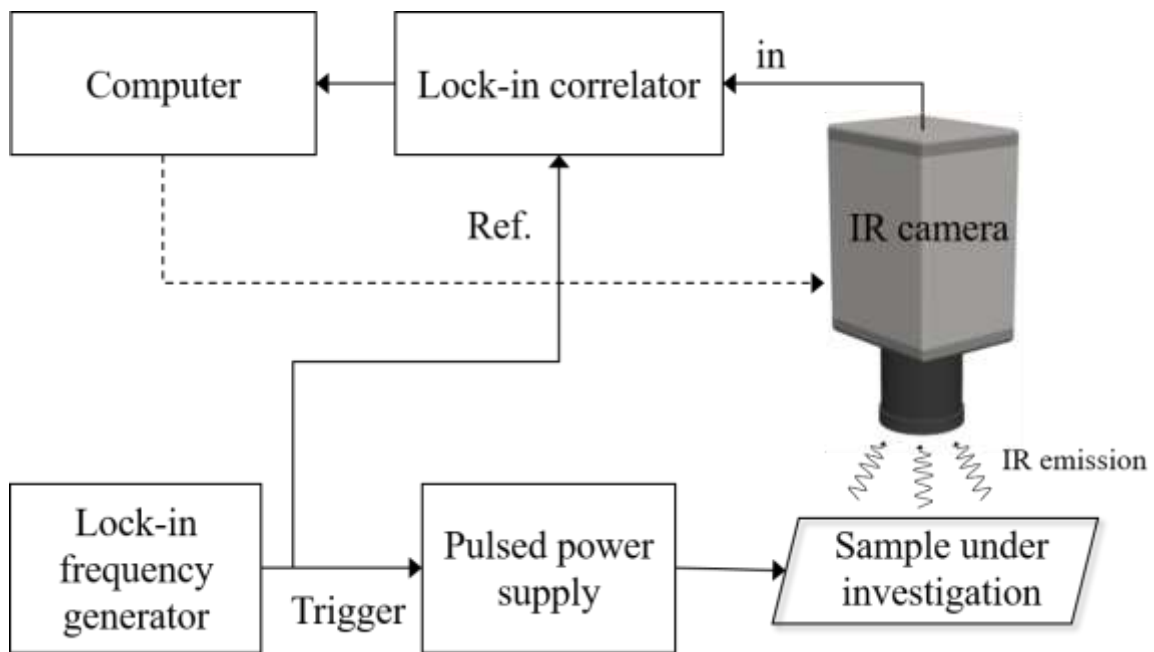
Figure 2.4. Schematic of lock-in thermography.
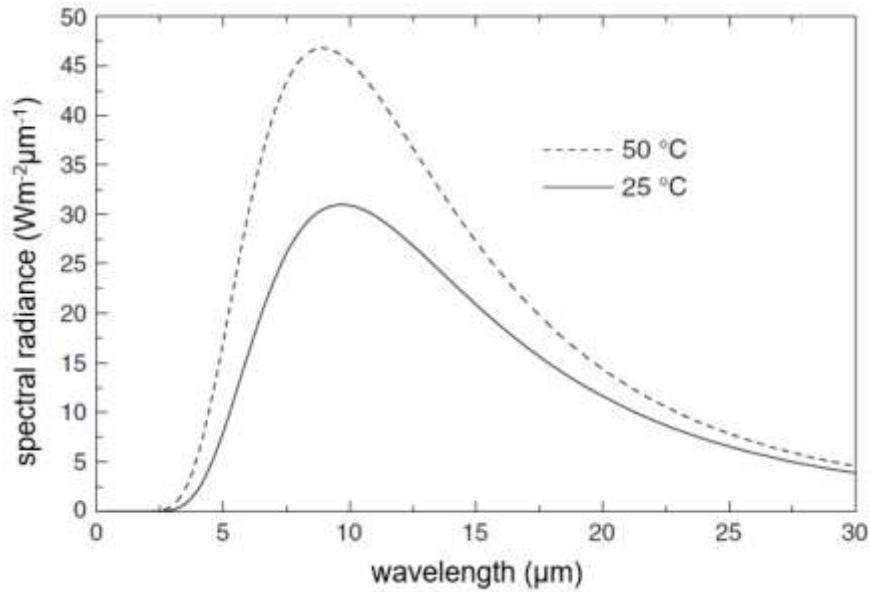
Figure 2.5. Black body radiation for two different room temperature, with higher radiation at a higher temperature. [192]
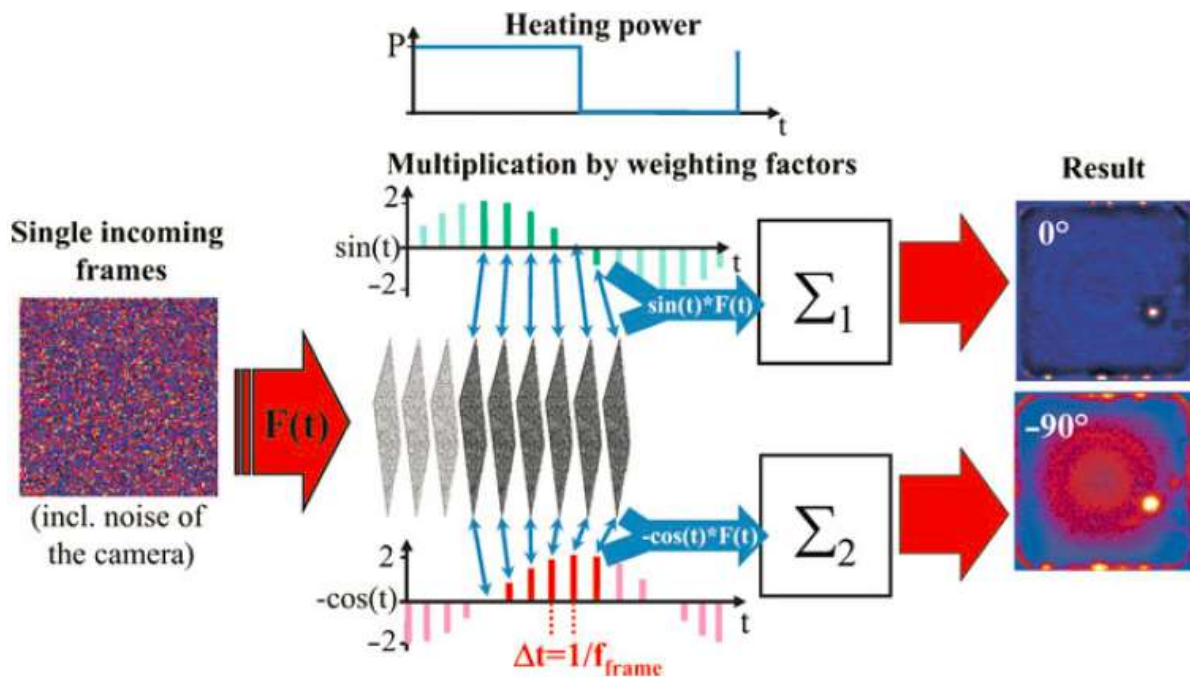
Figure 2.6. Principle of two-channel lock-in correlation procedure in lock-in thermography. [192]

The lock-in correlation procedure is mathematical multiplication of the detected signal F(t) with a correlation function K(t), K(t) is a periodical wave function is synchronized with the input lock-in frequency signal. For a fix-number of sampling event n per lock-in period, if the measurement is averaged over N lock-in periods, the digital lock-in correlation for synchronous correlation is given by:

$$S = \frac{1}{nN}\sum_{i=1}^{N}\sum_{j=1}^{n}K_J F_{i,j}$$

In a real test, as shown in Figure 2.6, two-channel correlation method is used to retrieve the in-phase signal and out of phase-signal. The correlation functions are:

$$K_j^{0°} = 2 \sin\left(\frac{2\pi(j-1)}{n}\right) \qquad\qquad K_j^{90°} = 2 \cos\left(\frac{2\pi(j-1)}{n}\right)$$

The resulting $S^{0°}$ and $S^{90°}$ are called the in-phase signal and the quadrature signal, respectively. Thus the lock-in amplitude A and signal phase Φ can be expressed as:

$$A = \sqrt{(S^{0°})^2 + (S^{90°})^2}$$

$$\Phi = \arctan\left(\frac{S^{90°}}{S^{0°}}\right) \text{ (-180° is } S^{0°} \text{ is negative)}$$

Compared with steady-state thermography, which is limited to detecting hot spots at least 100 mK (0.100°C) and dissipate at least 20 mW of power, lock-in thermography has a high sensitivity to 1mK (0.001°C) and dissipation below 100 µW (Figure 2.7). Higher sensitivity can be achieved by applying long test time to average the thermal images for several lock-in periods. With LIT, thermal amplitude image and thermal phase image could be obtained simultaneously. When test on an electrical component under the electrical power supply, the image of the local heat source within the electronic component can be visualized in the amplitude image, in which Joule heating, carrier recombination or Peltier effect in the sample can be evaluated. From the phase image, information about the heat dissipation rate to the surrounding/ adjacent area could be obtained. Different lock-in frequency could also provide different information. Lock-in measurement performed at lower frequencies could improve test signals/noise due to efficient heating to sample, while at higher frequency hot spot spatial resolution is improved because of a reducing thermal diffusion into adjacent areas of the device.
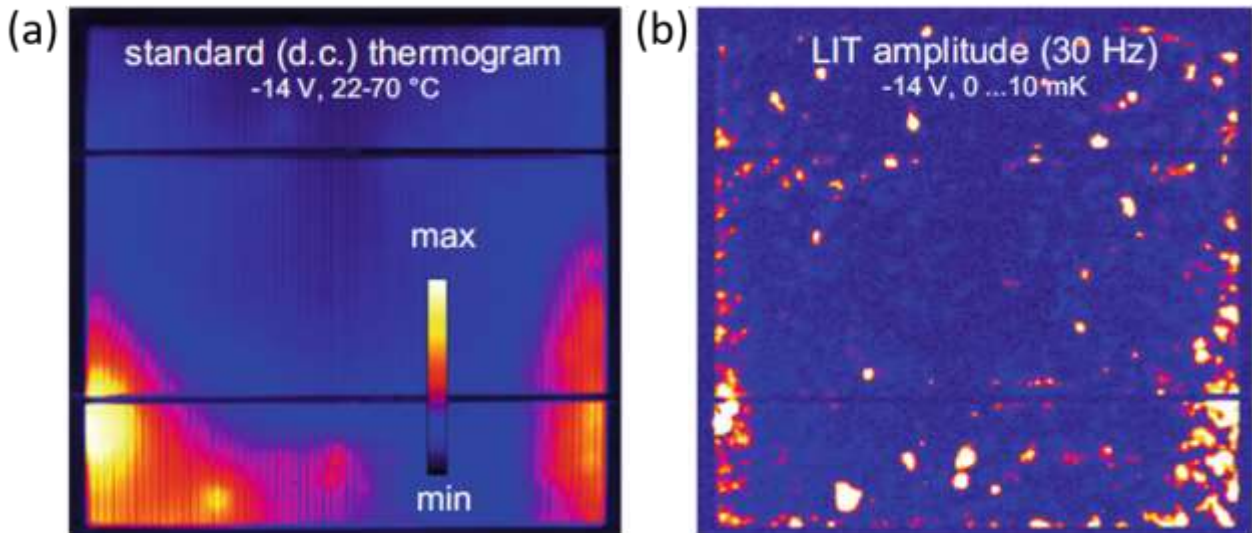
Figure 2.7. (a) A steady-state thermograph and (b) lock-in thermal amplitude image of a crystalline silicon solar cell. [192]

In recent years, LIT has shown a wide range of applications in the study of nanomaterials, evaluating physical properties or state variation in nanomaterials, for example, heating power in superparamagnetic iron oxide nanoparticles[193-194], localized defect in a graphene sheet[195]. In this thesis, we use LIT to detect the time-dependent formation of the current pathway in a neuromorphic

network. The network is powered by a pulsed current source. Due to Joule heat, the lock-in amplitude signal shows higher intensity along the current transmission pathway. Thus the dynamical formation of a current pathway can be visualized.

2.2.3 Electrical measurements

The resistance of the memristor can be modulated by the external power stimulation. In this thesis, we used the two-wire method to measure the conductance evolution of the memristive nanowire network under bias voltage, as shown in Figure 2.8. Experimental setup for electrical measurement. We used a two-wire test configuration terminated by Keithley 4200 Semiconductor characterization system (SCS) SourceMeter (Figure A-2).
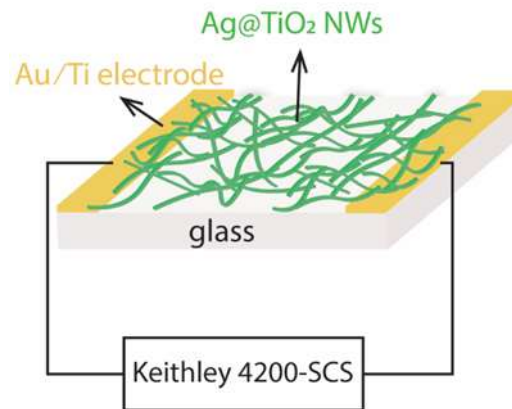
Figure 2.8. Experimental setup for electrical measurement. We used a two-wire test configuration terminated by Keithley 4200 Semiconductor characterization system (SCS) SourceMeter (Figure A-2).

Chapter 3: Emergent physical properties of integrated nanomaterials

In this chapter, we introduce the emergent physical properties found on two integrated nanosystems. We first introduce the unconventional Raman intensity rings observed on the graphene/micro-cavity system and then propose a theoretical model which explain the observed features. The second part of this chapter, we present the work on memristive nanowire network, which is composed by core-shell Ag@TiO$_2$ nanowires. For such a system, each nanowire-nanowire junction, with Ag/TiO$_2$/Ag structure, shows non-volatile threshold switching behaviour. We apply such nanowire random network to mimic certain biological functions in the bio-nervous system, extensively studied the sleep-dependent memory consolidation process in such network with theoretical simulation. In the third section, with LIT, we studied the dynamical current fluctuation in the network and found an association behaviour between different current pathways.

3.1 EMERGENT PHYSICAL PROPERTIES OF GRAPHENE ON A MICRO-STRUCTURED SUBSTRATE

3.1.1 Raman spectroscopy of graphene-integrated device

Raman spectroscopy is a widely-used, versatile and non-invasive tool for graphene characterization. For single-layer graphene, each unit cell has two carbon atoms. It has six phonon branches, three acoustic (A) and three optical (O) branches, named as iLO, iTO, oTO, iLA, iTA and oTA (Figure 3.1 a). Among them iTO mode phonons have E$_{2g}$ representation, they are Raman active phonons. In a typical Raman spectrum, as shown in Figure 3.1 b of single-layer graphene, there exist three main Raman peaks, named D, G, and 2D, which is located around 1350 cm^{-1}, 1582 cm^{-1} and 2700 cm^{-1}, respectively. Among them, D peak appears when there are defects at test graphene position. G and 2D bands of graphene are sensitive to strain[196-198], doping[199], the number of layers[200] and thermal variation [196-197, 199-201]. They have been ultimately analyzed for developing fast and precise investigation of graphene and its derivatives. For example, a previous study reported that strain and doping distributions of graphene on a SiO$_2$ substrate could be optically separated through Raman 2D band and G band frequency change ration[202]. Such phenomena were revealed through a detailed analysis of spatially-resolved Raman measurements (Raman mapping, hereinafter). By removing the substrate, phonon-cavity coupling observed on graphene drum is also an exciting topic towards electronic application[57]. A comprehensive Raman mapping analysis of graphene drum can provide valuable information for future NEMS.

In this section, we use Raman mapping to study the effect of substrate structure on the physical properties of graphene. Raman mapping was carried out at ambient condition by a confocal HR800 micro-Ramman spectrometer (Figure A-3). We used a 532 nm diode-pumped laser ($P_0 = 2.8mW$) and the spot diameter is around 1um. A piezo-actuated XY scanner was equipped to achieve Raman mapping with a specific step of 74nm.
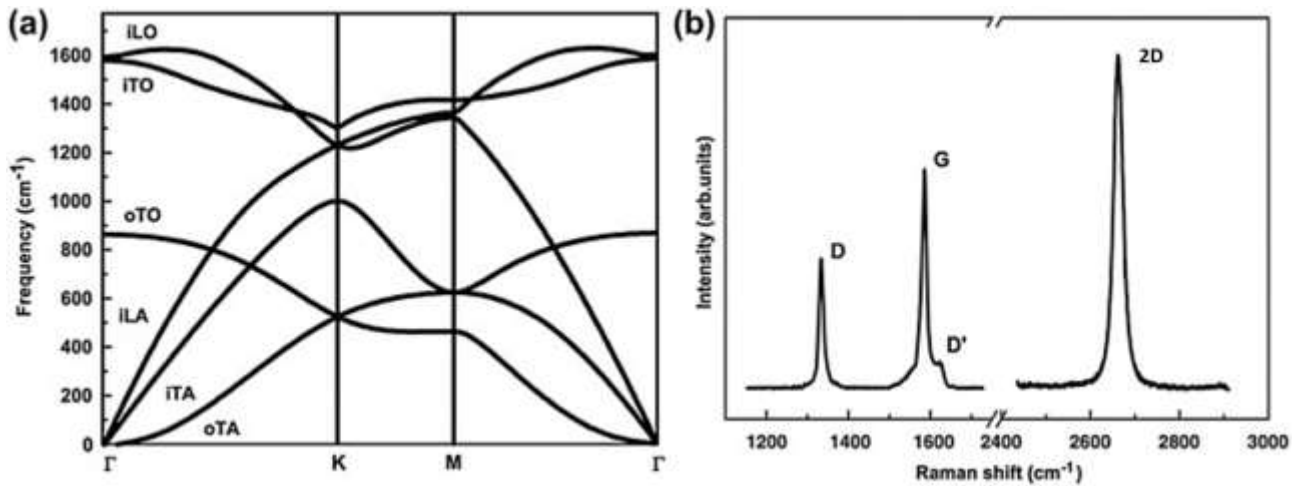
Figure 3.1. (a) Calculated phonon dispersion of single-layer graphene showing all six phonon branches. (b) Raman spectrum of a graphene edge, showing the main Raman features D, G and 2D bands (laser energy is 2.41eV).

3.1.2 Characterization of graphene over micro-cavities

Figure 3.2 shows the scanning electron microscope (SEM, Figure A-6) images of graphene over SiO_2/Si cavities with a diameter of 6.4 µm, 9 µm and 12 µm. The acceleration voltage for imaging is 2kV. Bare SiO_2 surface gives a brighter contrast while the graphene covered regions exhibit dark contrast. Double-layer graphene (DLG) region is darker than the single-layer graphene (SLG) region in the SEM image because of larger screening of secondary electrons from the substrate in the DL region. Over cavities, both suspended SLG and DLG are found as circled. SEM images of the cross-section of the cavity reveal a flat bottom but slight curvature near the sidewall, as shown in Figure 3.3. The depth is ~3.7µm for all cavities. The quality and the number of layers of graphene were also characterized by micro-Raman spectroscopy (Figure 3.4). The absence of D peak in all spectra indicates good quality of graphene sheet after transfer. We point out that the Raman intensity of both G and 2D of suspended part is three times smaller than that of standing graphene, which will be discussed later.
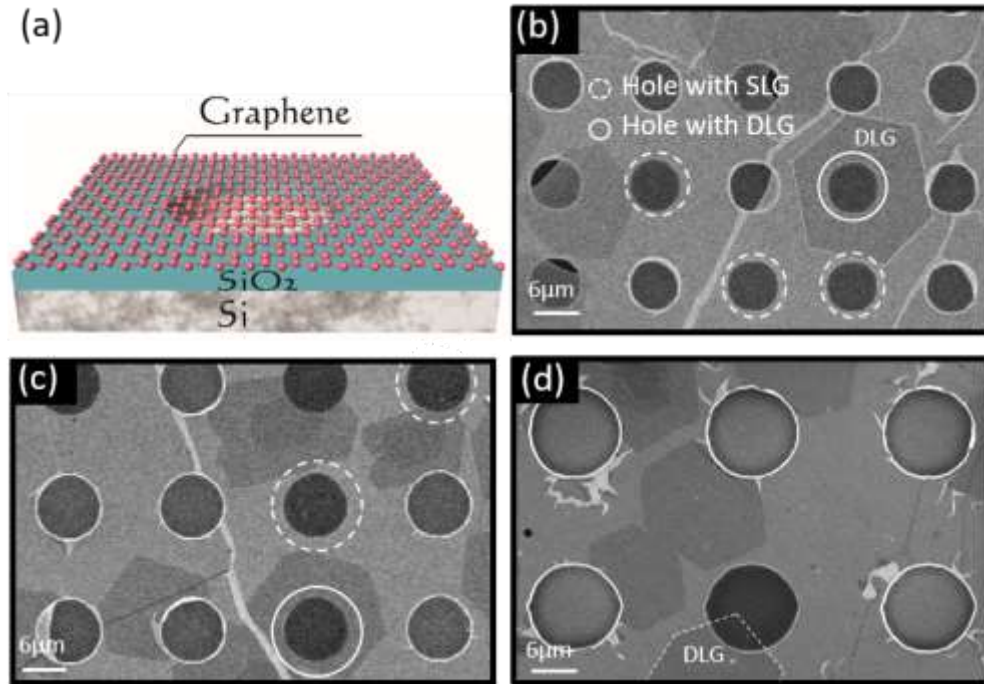
Figure 3.2. Characterization of graphene device. (a) Schematic of final device. (b-d) SEM images of graphene sheets over SiO₂/Si cavities of different diameters: 6 µm (d), 9 µm (c), and 12 µm (d). Regions of single layer graphene and double layer graphene are indicated with dash and solid lines, respectively. Acceleration voltage: 2kV.
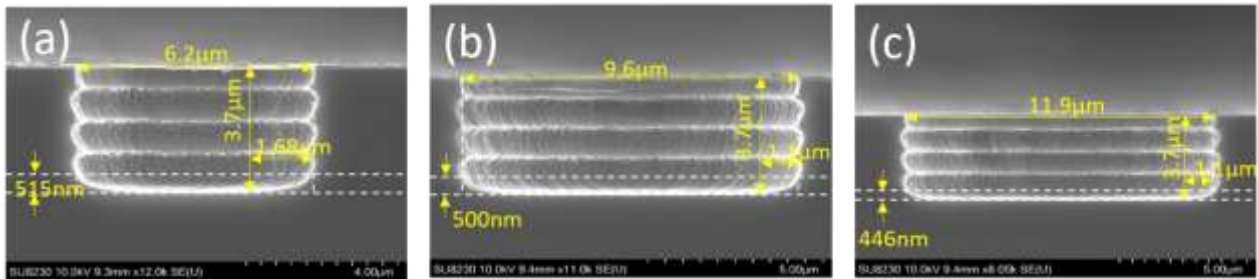
Figure 3.3. Cross-sectional SEM images of SiO₂/Si cavities of different diameter: 6.2 µm (d), 9.6 µm (c), and 11.9 µm (d). The depth of all cavities are 3.7 µm.
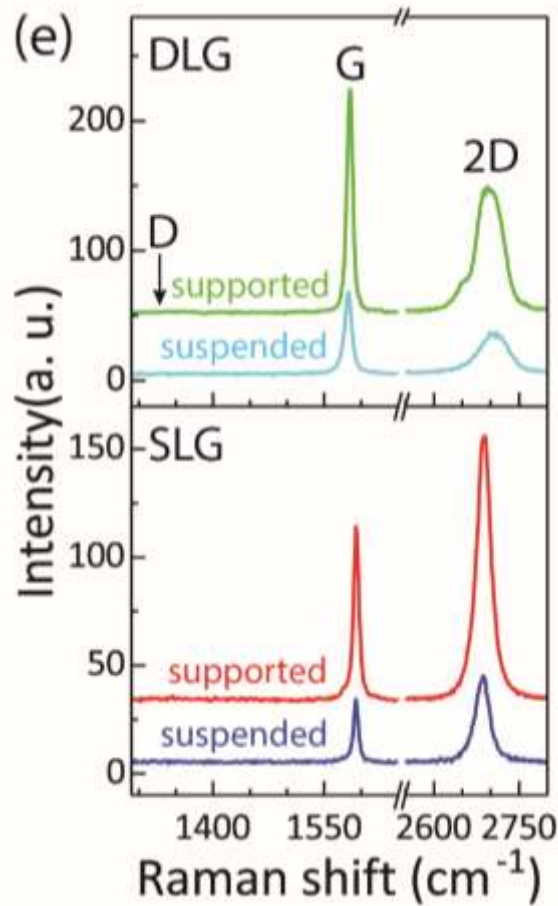
Figure 3.4. Raman spectra of suspended and supported SLG and DLG. D arrow points to 1350 cm-1.

3.1.3 Raman intensity oscillation on graphene over micro-cavity

Raman mappings carried out on SLG are shown in Figure 3.5 (a) and (b), showing the peak position and intensity maps of the G mode vibration. Despite several fringes exist around the edge of the micro-cavity which correspond to folding graphene, we recognize a downward shift of G band from supported graphene (~1596 cm^{-1}) to suspended graphene (~1593 cm^{-1}), owing to a softening of graphene. The lowest G band wavenumber appears in the vicinity of the edge of the cavity. In contrast, clear oscillations appear on its intensity map. The lowest intensity is not at the same position as in G band map but in the middle between edge and center, as indicated in the cross-sectional intensity profile below the map. Similar behaviour is also observed for 2D band maps, as shown in Figure 3.5 (c) and (d).
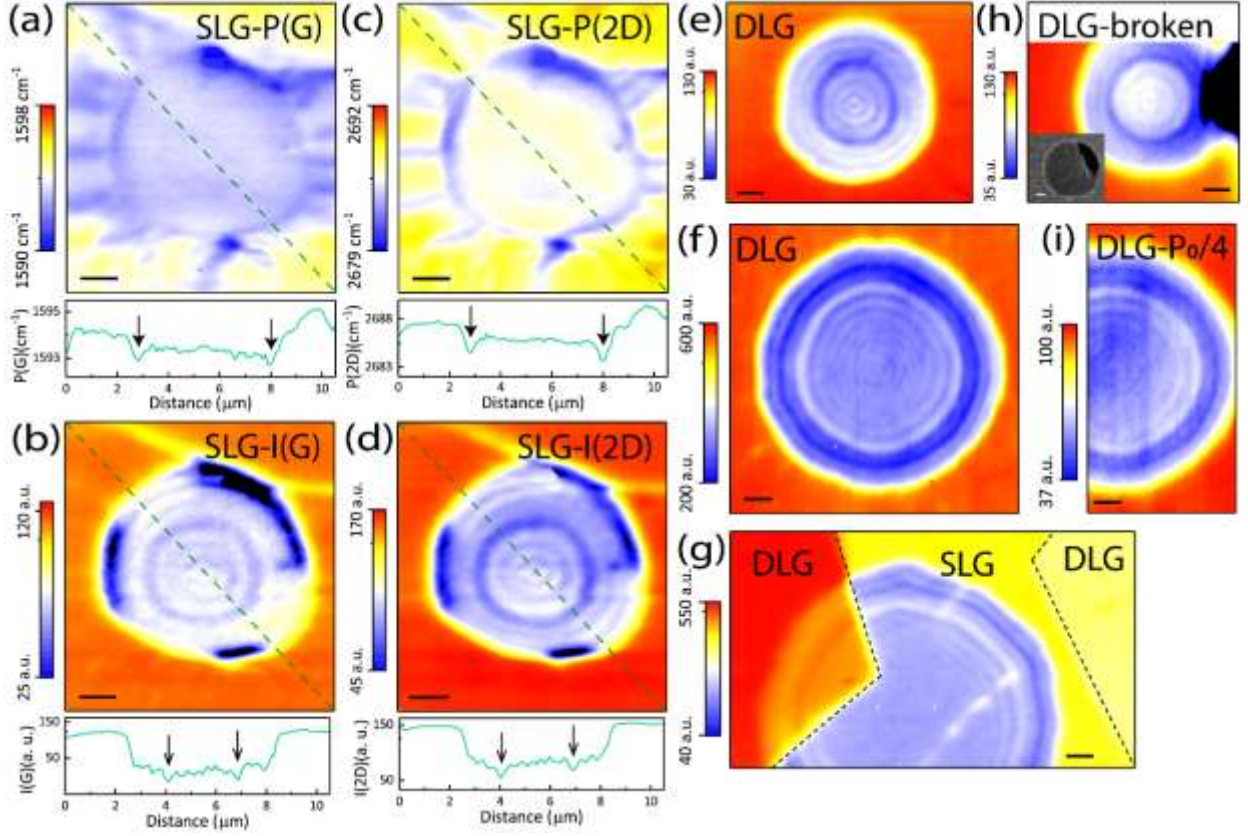
Figure 3.5. (a-d) Raman maps of a 6.4um SLG: (a) G band position/P(G), (b) Intensity of G band/I(G), (c) 2D band position/P(2D), (d) Intensity of 2D band/I(2D). Below each map is the profile of the green dash line. (e-i) Raman intensity maps of 2D band: (e) a 6.4μm DLG, (f) a 9.6μm DLG, (g) a 12μm graphene with SLG and DLG interconnected, (h) a broken 6.4μm DLG, inset shows the corresponding SEM image, (i) a 9.6μm DLG measured with reduced laser power (0.7mW). Scale bar: 1μm

To better understand the origin of oscillations in Raman intensity maps, we investigated the Raman maps of suspended DLG and also changed the size of micro-cavities. Figure 3.5 (e – g) show the Raman intensity maps of DLG over micro-cavities with different diameters. In Figure 3.5 (e) (cavity diameter: 6.4um), similar features shown in Figure 3.5 (d) are recognized: six concentric rings appear and the lowest intensity located at the similar position. Such consistency in SLG and DLG suggests that the number of layers does not contribute to the period of oscillation. In Figure 3.5 (f) (cavity diameter: 9.6um), ring number increases but the contrast decreases from edge to center. With increasing the cavity size, both ring number and contrast decrease to the center [Figure 3.5 (g)]. This tendency implies laser position affects phonon vibration efficiency in graphene.

There are several possible mechanisms could lead to the observed concentric oscillation in the Raman intensity maps. The electronic properties of graphene can be easily tuned by strain or doping, which usually cause Raman peak shift as well as intensity variation[202]. However, the difference between band position map and intensity map manifests the rising of intensity oscillation is not due to intrinsic property variation in graphene. Thermal effect could be another reason for such oscillation, which has been reported in a graphene bubble [203], where incident Raman laser and laser reflected from SiO_2 substrate interfere at graphene surface. However, in order to form the same number of rings as that in our observations, the height difference of the suspended graphene surface from center to edge for a 6.4μm cavity should be $n \cdot \frac{\lambda_0}{2} = 1.33 \, \mu m$ (take $n = 5$ and $\lambda_0 = 532nm$).

But except a slight height difference (~500nm) close to the edge, both the graphene surface and the bottom of cavity (Figure 3.3(c) and (d)) are sufficiently flat excluding this possibility. Taking into account of the super impermeability of graphene[204], we also considered about the possibility of expansion of the air sealed by graphene in the cavity owing to Raman laser irradiation. Figure 3.5 (h) shows Raman 2D intensity map of a slightly broken DLG. Compared with the fully covered one in Figure 3.5 (e), two maps show no big disparities. Therefore, the observed oscillation seems to be more like projecting some features from the cavity itself.

3.1.4 Theoretical simulation and discussions

We propose that the oscillation is caused by multiple-beam interference. When the laser irradiates the Si bottom and sidewall, part of the laser contributes to Rayleigh scattering at the Si surface and the intensity oscillation results from the superposition of the reflected field from all direction. Stokes phonons at the detector are created by two contributions: the incident laser E_G, and the Rayleigh reflection from the Si cavity E_{Si}. Thus the intensity at the detector can be integrated over all the possible incident/reflected angles and finally approximated as:

$$I \sim \left| \int (E_G + E_{Si})\, d\Omega \right|^2 \sim A_0^2 \left| \int_0^{2\pi} \int_0^{\theta_{max}} f(\theta) R(\theta,r) e^{i\Delta\delta} \sin\theta\, d\theta\, d\varphi \right|^2$$

where Ω is the integration solid angle with θ is the polar angle and φ is the azimuth angle. θ is limited by the numerical aperture (NA) of the objective lens with $\theta_{max} = arcsin(NA)$. A_0 is the amplitude of laser beam. $f(\theta) = e^{-2 sin^2\theta / sin^2\theta_{max}} 2\pi \cos\theta$ is the Gaussian laser beam profile. $R(\theta,r) \sim \frac{2\cos\theta}{\Delta l(\theta,r)\lambda_0^4}$ is the Rayleigh scattering coefficient of Si substrate and $\Delta\delta = \frac{2\pi\Delta l}{\lambda_0} + \pi$ is the phase difference of incident and reflected laser beams, with Δl as the optical path difference. Because of the existence of sidewall of the cavity, Δl depends on the laser position (r) on the suspended graphene and cavity depth.

Figure 3.6 (a) and (b) compares the experimental and theoretical intensity oscillation of a 9.6μm graphene. We neglect the unflatten region of bottom nearby the edge of cavity and compare the intensity from 1μm away from the edge. In Figure 3.6 (b), the first destruction point appears at 1.4μm, and 8 peaks appear afterwards. The intensity rises and drops along a horizontal line as seen both experimental and calculated data, which is unlike the decreased oscillation in the graphene bubble model[186]. We noticed the shift of oscillation peaks in theoretical results from experimental results, which may result from the unsmooth sidewall and bottom of the cavity (Figure 3.3). Figure 3.6 (c) collates the experimental and calculated positions of the rings for 9.6μm and 12μm, showing a good agreement between them. The multiple-beam interference model is a plausible one for our observations. With this model, it is expected that laser power will not affect the peak position, but reduce the contrast of rings, which is confirmed on the 9.6 um graphene with a less powerful laser beam ($P = \frac{1}{4}P_0 = 0.7mW$), as shown in Figure 3.5 (i).

The numerical aperture and cavity depth mainly contribute to the appearance of Raman intensity oscillation. In our proposed model, when laser only irradiates the flat cavity bottom, the integrated intensity does not depend on the position of the incident laser beam, as we observed in the central part of the 12 μm graphene (Figure 3.5 (g)). On the other hand, as a cavity depth decreases, the number of rings decreases, and the oscillation finally disappears. The proposed model also

explains why no clear intensity oscillation observed in the previous report [205], where the distance from graphene to the substrate was designed to be less than 500nm.
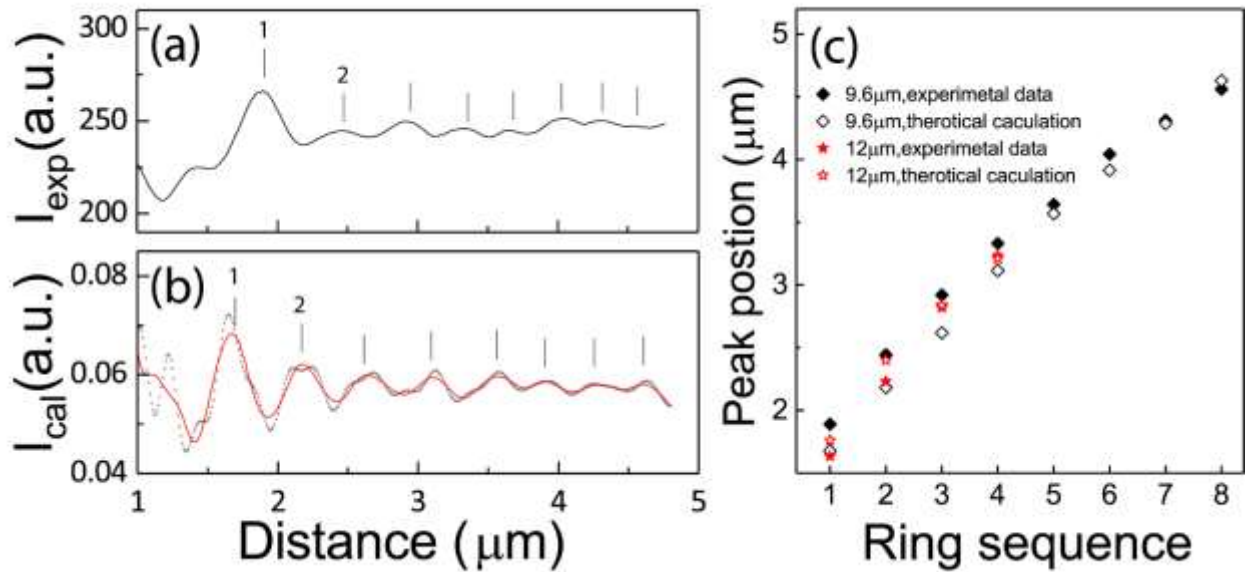
Figure 3.6. (a) I(2D) extracted from a 9.6μm DLG in Fig. 2f, the horizontal axis is measured from edge to centre. (b) Theoretically calculated approximation of I(2D) of a 9.6μm graphene, grey dot: raw data, red line: smooth fitting. (c) Comparison of experimental and theoretical peak position for 9.6μm and 12μm graphene.

3.1.5 Conclusions

In this chapter, Raman laser interaction within the cavity was projected onto a graphene sheet. This results in the formation of concentric rings in nanoscale on its Raman intensity mapping on the suspended graphene area, revealing Raman intensity oscillation from the edge of the suspended area to the central. Though no clear evidence shown for electronic modification on the graphene sheet in such drum architecture, we expect further application on graphene sheet to sense the underlying cavity structure. And same phenomena may be observed on other 2D materials with cavity structure and used to modify the electronic state of materials which are sensitive to thermal heating.

3.2 SLEEP-DEPENDENT MEMORY CONSOLIDATION IN AG@TIO₂ NANOWIRE NETWORK

3.2.1 Introduction to sleep-dependent memory consolidation

Formation and retrieval of memory are basic abilities of biological systems, which allow the individual to adapt to the changing environment and survive. The memory process consists of three stages： encoding, storage and retrieval. Encoding is the process of how information stores in the nervous system, during which a new memory trace (storage) is formed but could be easily interrupted or erased. Depending on the retention time, there are three main types of memory: sensory memory, short-term memory (STM) and long-term memory (LTM). When an organism perceives the environment, a certain amount of information enters the nervous system from the senses and is stored as sensory memory. Sensory memory has a very short retention time and can be easily lost, for example, human visual memory lasts only 0.25s~1s. The sensory memory can be transferred to short-term memory if special attention is paid to the information. Short term memory lasts from several seconds to several minutes. For example, if a new phone number is learned only a few times, it will be forgotten after several minutes. However, if the phone number is used very frequently, it will form a long-term memory that will retain for several weeks, several months and even a lifetime.

The process that memory transfers from a short one to a long one is known as memory consolidation, which involves cellular and system-level modification of neural structure and connection. In the standard two-stage process of the memory consolidation, information is first encoded as spike train to a rapid learning region (hippocampus) and then gradually consolidated into a slow learning region (neocortex) for long term storage. In the studies of the human brain's memory system, it is generally accepted that sleep plays a key role in memory consolidation. The sleep of human brain is composed of ~ 90-minute cycles, for each cycle consists of rapid-eye-movement sleep (REM) and non-REM sleep (NREM), with NREM containing stages 1 to 4 (a higher number indicates a deeper sleep involves)[206]. Neural activities in different sleep stage contain its typical electroencephalogram (EEG) signals, for example, ponto-occipitogeniculate waves and theta rhythm during REM, sleep spindles in stage 2 and slow oscillation during slow-wave sleep (stage 3 and stage 4). At the same time, eye movements, muscle tone, regional brain activation and communication between memory systems also show a difference in different sleep stages. Detection of such difference has been a powerful method to understand the brain's functionalities. More studies[207-210] have shown that during sleep brain will replay the learned information during awake, spatial-temporal patterns of neuronal activity become re-activated and assist the communication between hippocampus and neocortex (Figure 3.7). Neuroscientists found that total or partial sleep deprivation results in a reduction the learning improvement consistently though in different learning tasks and the failure of hippocampus directly prevents the formation of new long term memories[206, 208, 211-216].

The replay of information during sleep not only strength the memory traces quantitatively but also facilitates the formation of new associations and extraction of generalized features[217-218]. However, how replay promotes memory consolidation is still unclear at the cellular level. However, such a sleep-dependent memory consolidation process in a biological system could help to inspire the memory retention and memory trace re-organization in a physical neural network.
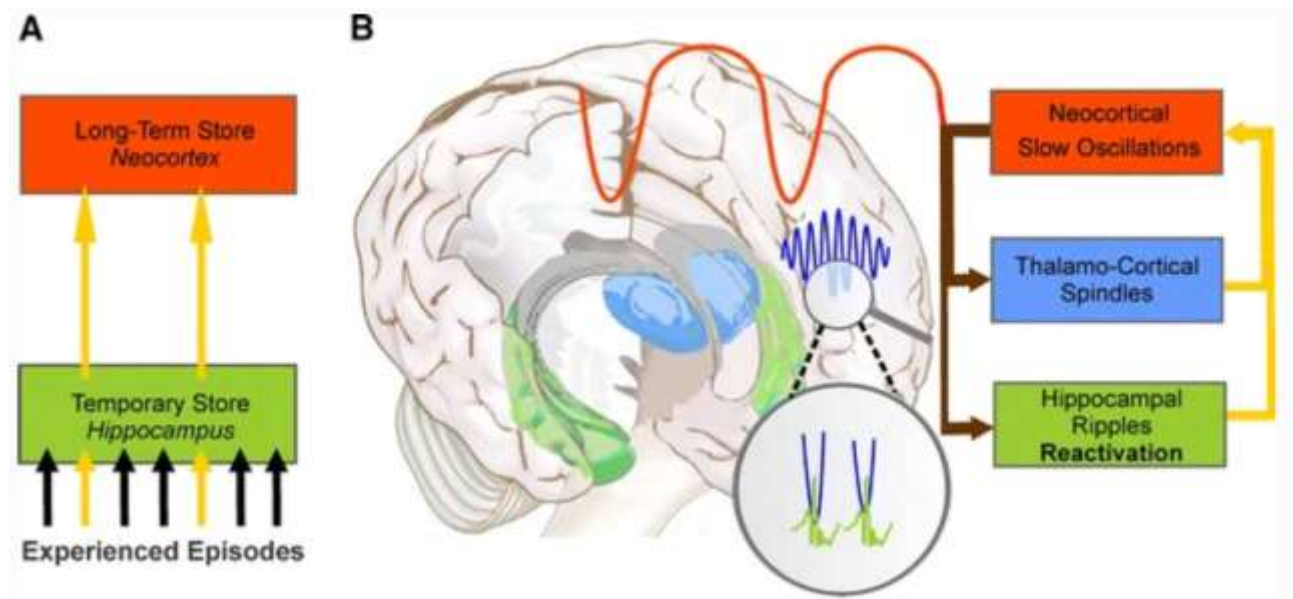
Figure 3.7. Sleep dependent memory consolidation. (a) Standard two-stage process of memory consolidation. (b) Sleep dependent memory consolidation relies on a dialogue between neocortex and hippocampus under top-down control by the neocortical slow oscillations (red). The depolarizing up phases of the slow oscillations drive the repeated reactivation of hippocampal memory representations together with sharp-wave ripples (green) in the hippocampus and thalamo-cortical spindles (blue). This synchronous drive allows for the formation of spindle-ripple events where sharp-wave ripples and associated reactivated memory information becomes nested into single troughs of a spindle (shown at larger scale).[219]

3.2.2 Characterization of Ag@TiO$_2$ nanowire

The structure and element distribution of the Ag@TiO$_2$ nanowires were characterized by transmission electron microscopy (TEM) with energy-dispersive X-ray spectroscopy (EDX) (Figure A-4). As shown in Figure 3.8, nanowires have uniform Ag cores covered with uniform polycrystalline TiO$_2$ coating. The inner Ag cores have an average diameter of 40 ± 6 nm, and the Ag@TiO$_2$ nanowires have an average diameter of 115 ± 17 nm (Figure 3.9). The length of nanowires follows a gamma distribution with an average length of 10 µm. The nanowire network device shows a functional nanowire network area of 40×40 µm^2 between two electrodes under an optical microscope (Figure 3.8c).
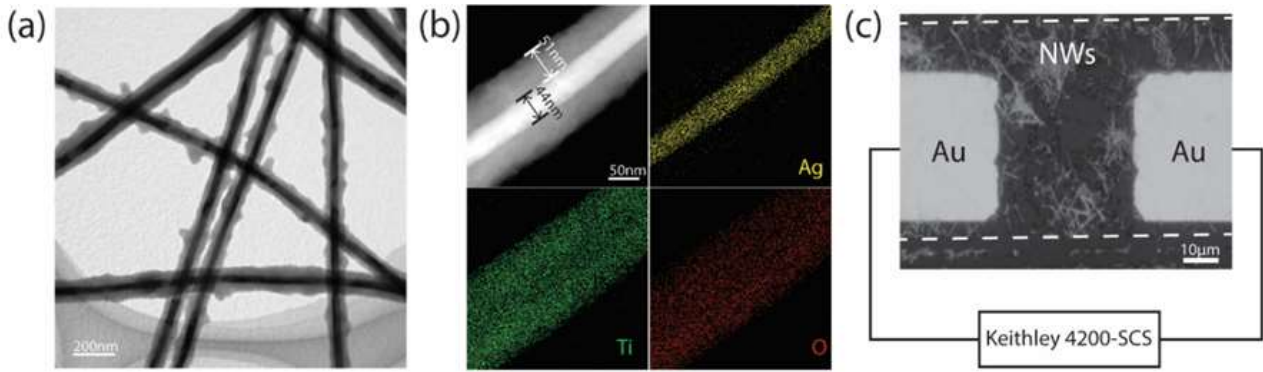
Figure 3.8. Characterization of Ag@TiO₂ nanowires. (a) Transmission electron microscope (TEM) image of the Ag@TiO₂ nanowires. (b) Energy-dispersive X-ray spectroscopy (EDX) mapping results on Ag@TiO₂ nanowire of three elements: Ag(yellow), Ti(green), and oxygen (red). (c)Optical images of the nanowire network device.
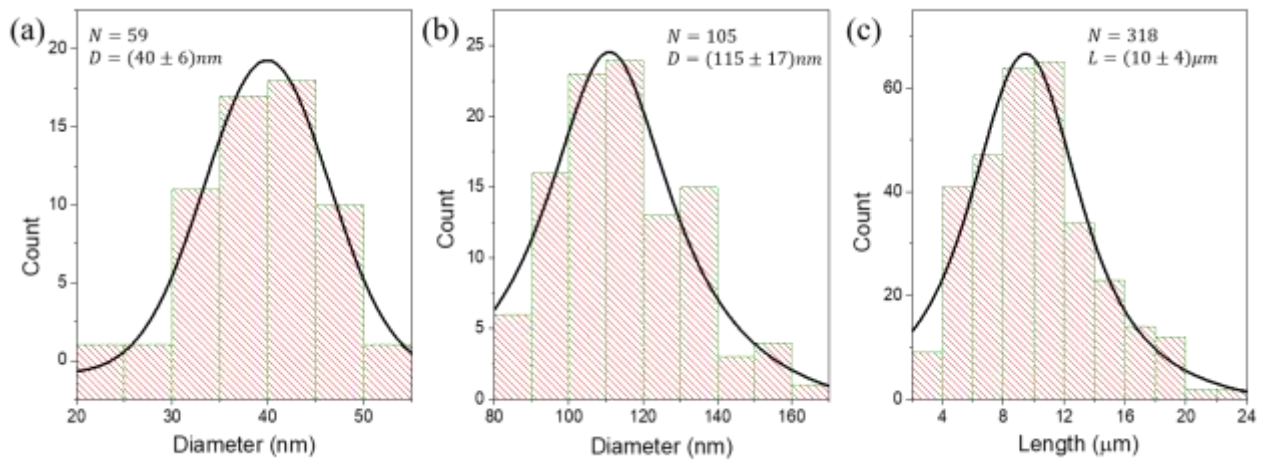
Figure 3.9. Statistics results of Ag@TiO₂ nanowire. (a) Diameter distribution of Ag core of Ag@TiO₂ nanowire. (b). Diameter distribution of Ag@TiO₂ nanowire. (c) Length distribution of Ag@TiO₂ nanowire.

3.2.3 Electrical properties of Ag@TiO₂ nanowire network

We performed continuous I-V sweeps with increasing compliance currents on these Ag@TiO₂ nanowire networks. The uniformity of the memristive device is important for future applications.[220] For our random networks, this can be achieved by controlling the network density. In Figure 3.10a, we show the results obtained from two networks which have a similar density. In the first sweep, the network initially remains at a nonconductive state and, as voltage increases, it switches to a conductive state at a threshold voltage (V_{th}). With decreasing voltage, the current decreases almost linearly from the compliance current (20 nA) and returns to the noise level (3 pA) at a voltage (V_{hold}) close to 0 V. Then, in the second sweep, the current compliance is set at 100 nA, and we observe both a decrease in V_{th} and an increase in the slope of the linear part. A similar behaviour appears for a voltage sweep in the opposite bias polarity. Such behaviour is known as a volatile threshold switching[147, 174]. Despite a slight shift of the V_{th} in the two networks, the IV behaviours for two networks are the same. In the case of the present nanowire networks, when the applied voltage increases, Ag aggregates are precipitated in TiO₂ regions at Ag/TiO₂/Ag junctions, eventually

evolving towards a conducting filament bridging the junctions (Figure 3.10 a, inset).[146, 221] This creates a collection of highly conductive junctions that link the nanowires together to a conductive pathway between the electrodes. When the voltage decreases, filaments between individual nanowire junctions are ruptured,[145, 222] reducing the flow of current as conducting pathways are disconnected. In the second sweep, the threshold voltage decreases, indicating that the connectivity of previously used pathways is to some extent retained within the network.
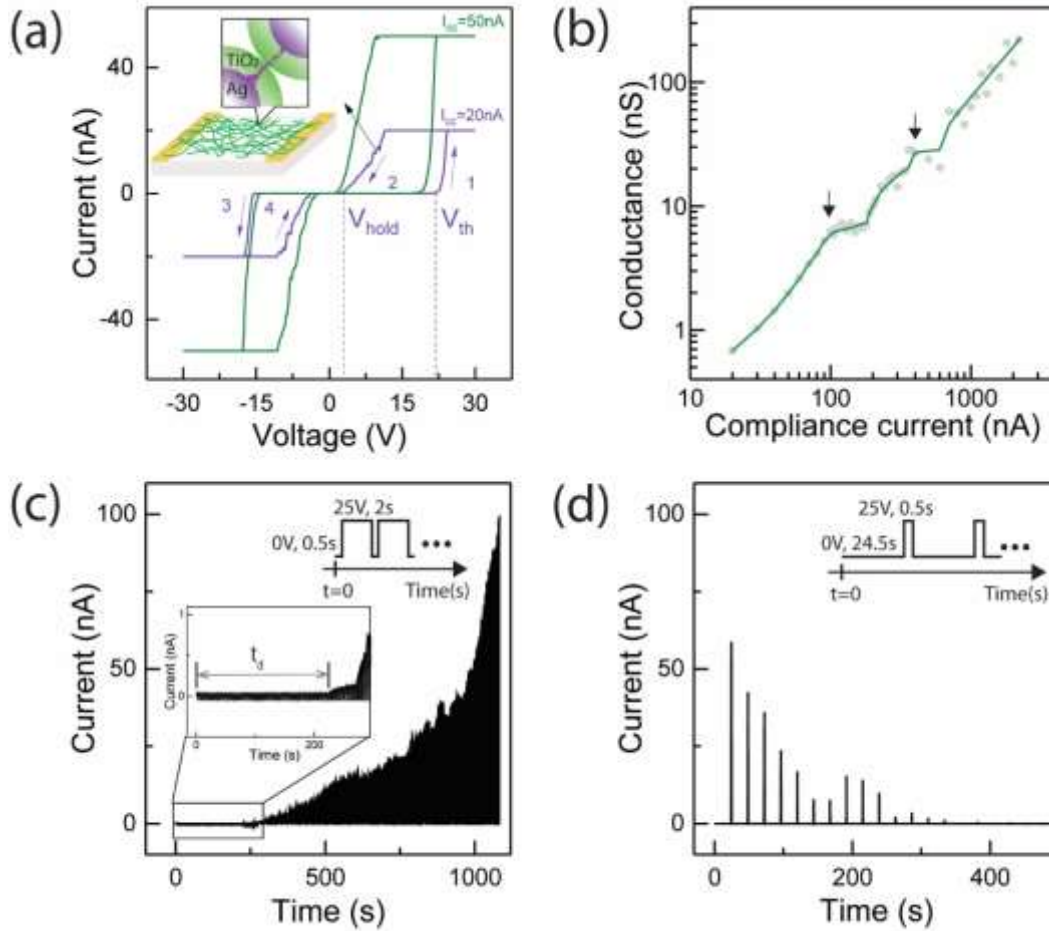
Figure 3.10. (a) Typical looped IV characterization of Ag@TiO₂ network for different programmed compliance currents. Inset: schematic of the experimental device where Ag@TiO₂ nanowires are connected by Ag aggregates in the TiO₂ shell. (b) Typical conductance plotted against the current compliance (log-log scale) in the network (grey dots) and its smoothed curve (green line). The conductance was calculated as the slope of the linear dependence region in the IV curve before V_{hold}. Clear plateaus appear as indicated by black arrows. (c) The current response of a network when a voltage pulse train with high power (0V, 0.5s; 25V, 2s) is applied between the electrodes. t_d represents a time scale when the current response is in the level of background noise. (d) The current response of the network immediately after (c) while a voltage pulse train with a lower power (0V, 24.5s; 25V, 0.5s) is applied.

We further explored the dynamical properties of current pathways in the network by tuning the compliance current (maximum flowing current), which was reported to be an efficient way of modifying the filament growth in a single memristor, leading to a volatile-to-nonvolatile switching transition.[145, 147, 223] The test was done by applying continuous positive voltage sweeps with increasing current compliance. As shown in Figure 3.10b, clear plateaus appear in conductance as current

compliance increases, indicating that energy barriers exist and some of the barriers are clearly higher than the others in the process of expanding a network of conductive junctions. An application of higher voltage and/or larger current establishes higher conductance state after activation, and longer retention time and stronger connection in the network is realized.[145, 224] The appearance of plateaus, suggesting the formation of multiple current pathways, is rather well observed under the present experimental conditions. Note that such plateaus are not observed in a single nanowire test,[181] in which usually one filament growth picture explains the memristive behaviour, and the same switching picture would also be plausible for the small memristive network.[145, 225] In the complex nanowire network, however, the stability of memory stored as current pathways was improved by increasing the number of conductive pathways. After lowering the compliance current to form a minimum number of pathways, the conductance state of the network became sensitive to random fluctuations of the physical state of some critical junctions distributed along the pathways. This behaviour was investigated after setting the maximum flowing current to 100 nA in our measurement system.

Figure 3.10 c and d show the current response of the network to the application of trains of voltage pulses with different frequencies and duty ratios. After the application of pulse train as illustrated in the inset of Figure 3.10c, the network initially remains at a low-conductance state for a time (t_d), which is necessary for Ag filaments to grow at individual junctions before opening a conductive pathway through the entire network. After t_d, the conductance exponentially increases to a high-conductance state. When the network reaches the compliance current, a voltage pulse was switched to that with a lower frequency and a smaller duty ratio as shown in the inset of Figure 3.10d. The network conductance decreases and is finally lost as seen in Figure 3.10d. The increase and decrease in the conductance of the network indicate that the physical process controlling the network connectivity can be tuned by the frequency and duty ratio of the voltage pulses applied to the network.

Next, we further explore the retention of the network conductance. Figure 3.11a and b show how the network responds to the consecutive application of pulse train stimuli with different frequencies/duty ratios and offset bias potentials (V_{bias}), respectively. Frequency and duty ratio were controlled by changing the interval time (t_i) between pulses and by keeping the ON time of the pulse to be 0.25 s. By setting V_{bias}, the network is always biased even during the interval between adjacent voltage pulses. Before each measurement, the network was activated to a high-conductance state in a similar way as in Figure 3.10c. Application of the voltage pulses with t_i=1.25 s results in an increase in current (Figure 3.11a, left), indicating that the network connectivity is consolidated. By increasing t_i, the increase in current is suppressed and finally the current decreases as seen in the cases of $t_i >$ 3.25 s, where the decrease in the current indicates a loss of network connectivity. A similar behaviour appears when decreasing V_{bias} as shown in Figure 3b. Apparent conductance growth (consolidation) is observed with V_{bias} = 15 V, while, lowing V_{bias} below 9V results in a loss of the network conductance.

The measured current values during the application of voltage pulses in Figure 3.11 a and b have been fitted using a time-dependent exponential equation:
$$I = I_0 e^{\alpha t}$$
Here, the sign of the α index, when it is positive (negative), indicates a consolidation (loss) of memory (conductive pathway) stored inside the network. It also corresponds to a growth or retention time constant, $\left|\frac{1}{\alpha}\right|$, of memory. As shown in Figure 3.11c, α shows a gradual shift from a negative to a positive value both with an increase in t_i or with a decrease in V_{bias}. The t_i- and V_{bias}-dependent curves cross at $\alpha = 0$, suggesting that it is the critical point in which the network could preserve the

conductance state optimally with minimum power. The connectivity stored in the nanowire network, with deliberate control, can be precisely maintained for an arbitrarily long duration if the network does not fluctuate at all.
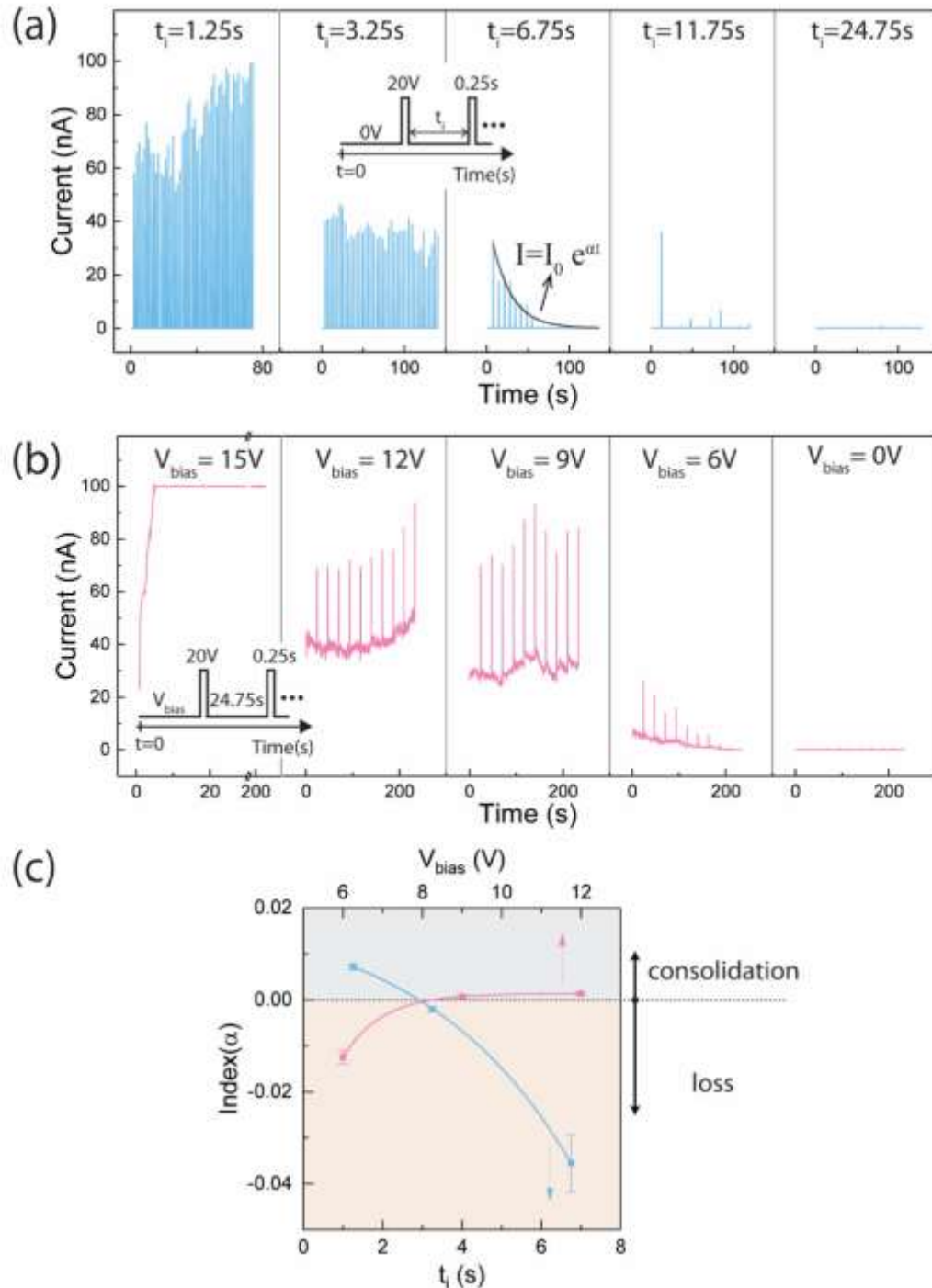
Figure 3.11. (a) Current responses of the network upon voltage pulse train stimulation with a different pulse time interval t_i. From left to right: 1.25 s, 3.25 s, 6.75 s, 11.75 s and 24.75 s. Each measurement was taken after activating the network to a current of 100nA with high-power voltage pulses (0 V, 0.5 s; 20 V, 2 s). (b) Current responses of network upon voltage pulse train stimulation with different bias potential V_{bias}. From left to right: 15 V, 12 V, 9 V, 6 V and 0 V. Each measurement was taken after the same preactivation process as in (a). (c) Index (α) vs. time interval (blue) and bias potential (red), extracted from (a) and (b), respectively.

Index α was calculated from the fitting curve of the current response as illustrated in (a). Two curves intersect at α=0.

3.2.4 Sleep-dependent memory consolidation in Ag@TiO₂ nanowire network

Inspired by the framework of sleep-dependent memory consolidation processes occurring in the human brain,[207, 210] the connectivity controllability during a period of the nonconductive state of the network was further investigated. We have designed a learning-sleep-recovery cycle to mimic the sleep-dependent memory consolidation process (Figure 3.12a). We have adopted two types of sleep mode: the active sleep (AS) mode that aims to mimic functional neural activities during the biological sleep period with the intermittent application of voltage stimuli, and the normal sleep (NS) mode in which no stimuli are applied to the network.

In Figure 3.12b, we show the current response of the network during a learning-sleep-recovery cycle with the sleep in the AS mode. Here, we used $V_{bias} = 0$ V, $t_i = 0.5$ s and pulse height and width of 8 V and 2 s, respectively [hereinafter, we simply describe such a condition as (0 V, 0.5 s; 8 V, 2 s)] for learning and recovery processes while we adopted (0V, 24.5 s; 8 V, 0.5 s) for the sleep in the AS mode. The initially nonconducting network was activated to a conducting state (Learning) with a high-frequency train of pulses and a large pulse voltage. Since the nanowire networks were prepared in a randomly assembling fashion, required pulse conditions for such learning were somewhat dependent on the samples. In the case of Figure 3.12b, a learning period, to form a conducting connection through the network, initially took a long time ($t_o = 545$s). Once the current reached a given compliance current of 100 nA, the AS-mode sleep was automatically triggered. It is very important to point out that, in each 8 V pulse application during the sleep period (AS^1), the network response is flat and only current below the background noise is detected, indicating that the memory of the high-conductance pathway is lost. Then the recovery process started (Recovery^1) and the network again reached the compliance current in a significantly shorter time (t_r^1 =64s). This implies that, although the network conductance drops to the low state during sleep, the connection of the current pathway (memory) was somewhat maintained in the network. Interestingly, this behaviour is repeatable and controllable. Gradually increasing the total sleep time while maintaining the same pulse train parameters results in increases in the recovery time as seen in AS^2 and Recovery^2 processes in Figure 3.12b, for example. If no control pulse train is applied to the network during sleep (the NS mode), the recovery times are longer. Figure 3.12c summarizes the recovery time versus the sleep time for both the AS and NS modes, and we observe a linear dependence in both but with a larger slope for AS mode. Every data point is averaged over 6 AS and 2 NS cycles within the same network. For sleep-recovery cycles both in the AS and NS modes, the recovery time becomes smaller when the sleep time is short. It is also recognized that, as the sleep time increases, the difference between the AS and NS modes becomes smaller.

The results in Figure 3.12 suggest two similar behaviours of our Ag@TiO₂ nanowire network to the human memory system. First, recent memory is easily recalled. Second, sparse stimuli during sleep help to consolidate the memory. To account for the origin of these behaviours in our network device, at first, we have to consider the processes occurring in individual nanowire-nanowire junctions during current transmission. In a typical metal/oxide/metal memristor with a similar stacking structure of junctions in our network, mobile metal ions drift towards the cathode and are neutralized and precipitated in the oxide layer when an electric field is applied, which leads to a diffusive growth of a metal filament along the ion drifting pathway.[139-140, 222] The growing speed of

the filament depends on the electric field as well as the ion mobility inside the oxide layer.[140, 147] As the end of filament approaches to the cathode, a tunnelling current starts to flow through the junction and a conducting channel is formed inside the junction followed by the further increase in conductance owing to further growth of the filament physically bridging the gap between the anode to cathode. However, when the electric field is removed, the metal filament starts to rupture and, depending on the interfacial energy between the oxide layer and metal filament and thermal effect induced by joule heat, retention of the filament differs.[145, 226] Wang et al. have reported the rupture of filament after 0.7 s in a planar $Au/SiO_xN_y:Ag/Au$ device,[222] the broken filament later reshaped to long-lifetime clusters that contribute to the volatile characteristics of memory as observed in our network.
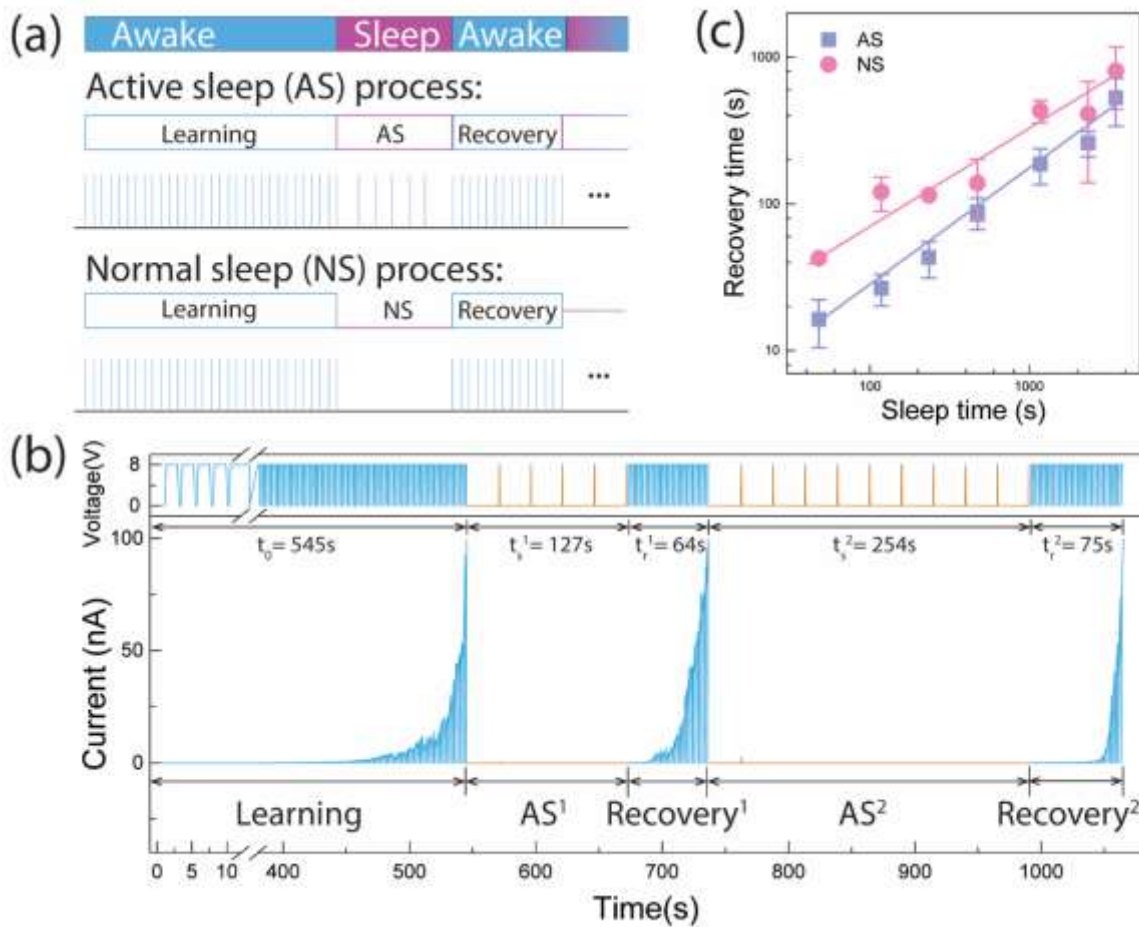
Figure 3.12. (a) Illustration of the learning-sleep-recovery scheme where an active sleep (AS) process or a normal sleep (NS) process is integrated. (b) Current response during learning-sleep-recovery cycle when AS process was embedded. During the learning and recovery periods (blue lines) continuous intensive pulses (0 V, 0.5 s; 8 V, 2 s) were applied, whereas during the sleep periods (orange lines), reduced pulses (0 V, 24.5 s; 8 V, 0.5 s) were applied. (c) Plots of recovery time vs. sleep time for measurement cycles with AS or NS process.

3.2.5 Theoretical simulation and discussions

We used python (Appendix C) to build a theoretical model of the nanowire network to further understand the process of sleep-dependent memory consolation at level of individual level, with

assuming a volatile switching caused by the growth and reduction of the Ag filament at every junction between nanowires. The dynamical equation that defines the evolution of the filament with time in the presence of an electrical field is :

$$\frac{dw(t)}{dt} = \mu \frac{v}{t_g} - \frac{w(t)}{t_r}$$
$$w(t + dt) = w(t) + dw$$

where $w \in [0,1]$ is the width of Ag filament in one junction at the current time and μ is the Ag ion mobility inside a polycrystalline TiO$_2$ layer. τ_g and τ_r are the characteristic constants of filament growth and reduction, respectively. The conduction equation relating to voltage v and current i is defined as:

$$i = G(w) \cdot v$$
$$G = \frac{G_{on} - G_{off}}{e^{\frac{1}{\tau_0}} - 1}\left(e^{\frac{w}{\tau_0}} - 1\right) + G_{off}$$

where G_{on}, G_{off} are the conductance of junction when filament width is 0 or 1, respectively, and τ_0 is a predefined parameter. The result conductance of one junction is exponentially growing with filament width. We use $\frac{\tau_g}{\mu} = 3\,s, \tau_r = 5s, G_{on}(w = 1) = 1 * 10^{-7}S, G_{off}(w = 0) = 10^{-12}\,S$ and $\tau_0 = 0.02$ in the simulation.
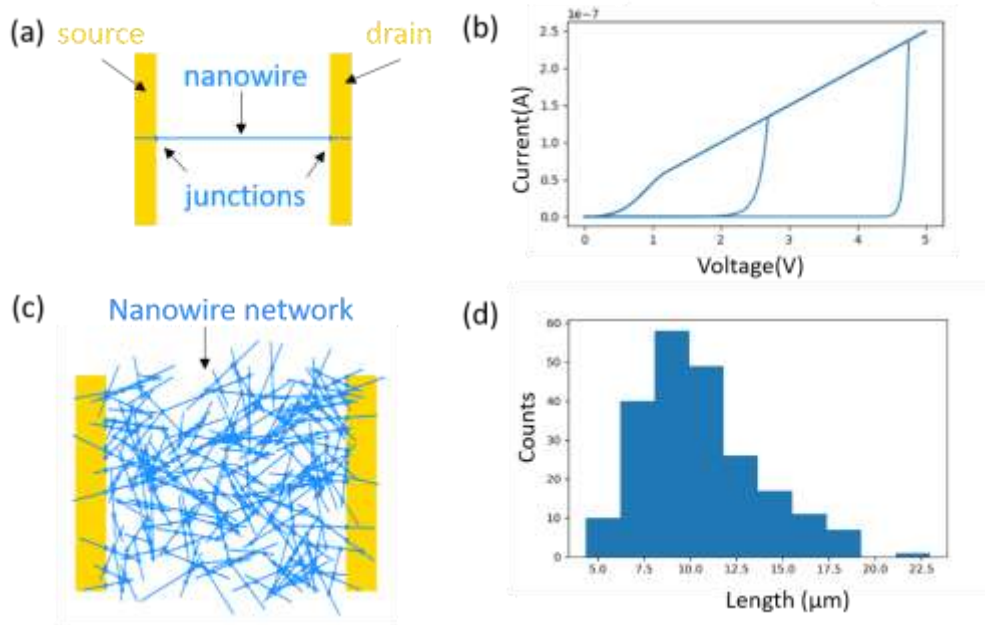
Figure 3.13. (a) Setup illustration for single nanowire simulation, consists of two electrodes (gold rectangular boxes) and one nanowire (blue line). The contact points are marked with blue dots are the positions of the junctions. (b) Simulated IV characteristic of the single nanowire. (c) Morphology of the nanowire network in the simulation. (d) Nanowire length distribution in (c).

A threshold switching activation dynamics for single nanowire was equally observed with this simulation, as shown in Figures 3.13 a and b. With continuous voltage sweeps applied between the source and drain in the simulation, the switching voltage decrease. We constructed a nanowire network following the experimental network, with same nanowire density (0.137 /μm^2) and length distribution (Figures 3.13 c and d). The dynamical simulation of current and filament distribution in

the network was conducted with general nodal analysis (1)a)Appendix B), in which the current fluctuation in each junction node was calculated based on the Kirchhoff's law.

In the simulation, a voltage pulse train with same voltage value in the experiment (0.05s, 0V; 0.05s, 15V) was first applied to activate the network to a high conductance state (current reach 150 nA) (Learning). Then two schemes were performed for 20s: normal sleep (NS) process and an active sleep (AS) process. During normal sleep period, no external voltage was applied, while during the AS period, a spare voltage pulse train (1.76s,0V; 0.24s, 15V) was applied. After that, the same pulse train as in the learning process was applied to reactive the network to the same high conductance state (Recovery).

Figure 3.14a shows the simulated current responses during the learning-sleep-recovery cycles with sleep in the NS and AS modes. The behaviour illustrated in Figure 3.12 is well retrieved from the network simulation, that is, the sleep in the AS mode results in a shorter time to recover the conductance than in the NS mode after the same sleep time. Here, we show a snapshot of the simulated network at time t1, just before sleep. At t1, several current pathways are active within the network, as graphically shown in Figure 3.14b. The histogram of the Ag filament widths over the network at this time is shown in Figure 3.14c. When the external voltage is shut down during the sleep, current stops flowing and the filament width starts to decay, as shown in Figure 3.14 d-f. If the sleep duration in the NS mode is longer than the lifetime of all the grown Ag filaments, the network will reset to the original condition before learning. This is indeed observed in Figure 3.14f where all the widths of the Ag filaments are reset to zero. However, even for the same sleep duration, if the sleep is in the AS mode, the volatility of junctions is compensated by the intermittent regrowth of the Ag filaments as seen in Figure 3.14g-k. Therefore, the information of the conductance pathway is not completely lost and recovery requires a shorter time.

It is very interesting to compare Figure 3.14 c just before sleep and Figure 3.14 g-k during the sleep in the AS mode: Most of the junctions within the network have not completely decayed but those with a large width (w > 0.8) have disappeared. This explains why the conductance of the network disappears during the sleep in the AS mode even when many of the Ag filaments are still surviving as we have seen in the experiment (Figure 3.14 b) and the simulation (Figure 3.14 a). In other words, when the network is activated after the learning process (t1), there is a broad and dispersed distribution in filament width, and several filaments grow and largely contribute to current transport throughout the network, namely, there are critical junctions formed in the network.
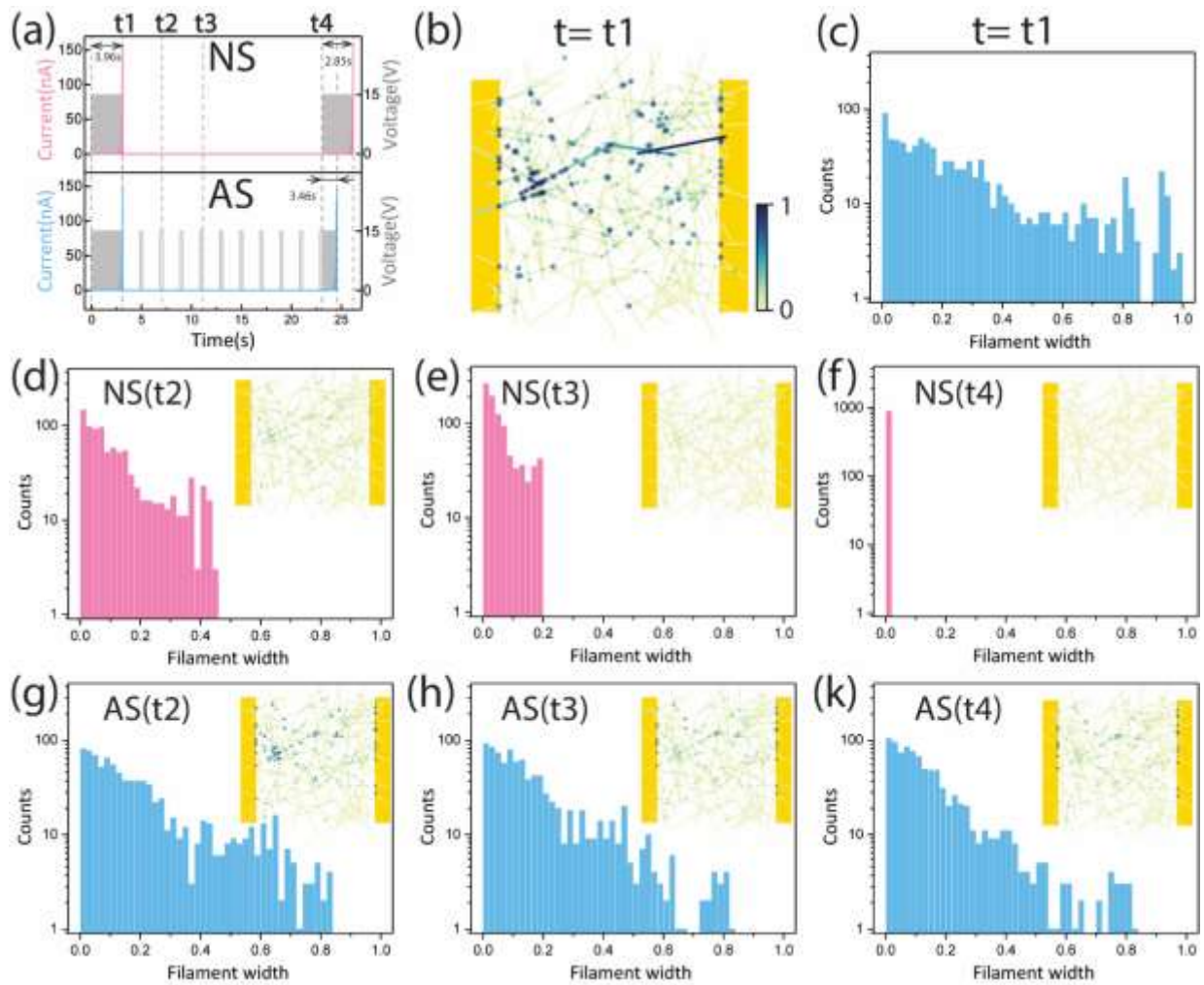
Figure 3.14. (a) Current responses during learning-sleep-recovery tests for a NS process or AS process in a simulated nanowire network. The network reaches the same state at time t1 in two cases under high-frequency voltage pulses (0 V, 0.05 s; 15 V, 0.05 s). During AS, a low frequency voltage pulse train (0 V, 1.76 s; 15 V, 0.24 s) was applied. (b) Map of current and filament width distributions in the simulated network after the learning process (time t1, both values were normalized to the same color bar scale). (c) Histogram of filament width distribution in (b). (d-f) Filament width distributions during NS process at different times (indicated in (a)). Inset: corresponding map of distribution. (g-k) Filament width distributions during the AS process at different times. Inset: corresponding map of distribution.

If we consider that all the Ag filaments decay at the same rate, filaments at critical junctions do not disappear spontaneously but effectively shut off the current through the network. During the sleep in the AS mode, a Ag filament at a junction intermittently grows and dissolves in response to the intermittently applied bias voltages, and finally, its length starts to oscillate (Figure 3.15). This situation is the same for the filaments that formed along the current pathways, but they can stay as relatively long filaments even after sleep time. The sleep in the AS mode does have the effect of selectively stabilizing junctions along the previous current pathway, so that the consolidation of the memory occurs. As a consequence, when the recovery cycle is performed, the previously established pathway tends to be readily restored instead of opening another pathway.

The simulation results have revealed a self-adaptive behaviour of individual junctions with the sparse stimulus during sleep, which leads to the selective retention of connectivity in the network. This effect is significantly important when handling a multi-terminal information process in such a

complex structure. Compared with one single nanowire device or other metal/insulate/metal stacking devices, the memory consolidation process observed in the present network ensures that the information is only stored within a minimum number of junctions. The active sleep consolidates the memory to stabilize the information storage for a long time and also to improve the recovery efficiency compared with the normal sleep, being somehow a similar process of memory consolidation in the human memory system.

In this nanowire network system, the TiO_2 layer was used as the diffusive media for Ag ions. Compared with Ag@PVP nanowire[224] or metal oxide nanowire,[175-176, 183] relatively thick TiO_2 coating increased the diffusive barrier for Ag ions and a higher voltage and lower operation current were used to drive the network in our study. However, these conditions can be controlled by tuning the network density and topological structure. It is worthwhile to point out that the TiO_2 layer in this work enables a volatile switching process at each nanowire-nanowire junction, which allows the system to stay with high connectivity but with high resistance, and therefore avoiding the jumbled conductance association between different pathways in the network.[184, 224] Conductance correlation between neighbours sites in either a crossbar-type neural network or a random neural network has been a practical problem towards a highly accurate and efficient process in neuromorphic cognition or computation devices. Materials design of the diffusive memristor with high switching on/off ration, low switching energy and long endurance are certainly important issues for further advancing neuromorphic technologies.
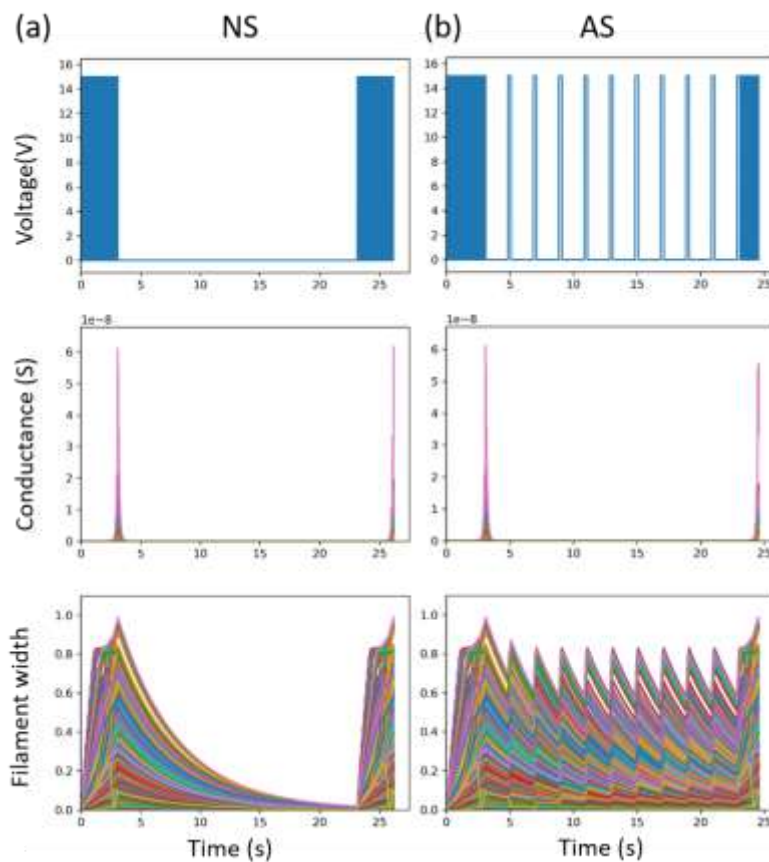
Figure 3.15. Voltage, conductance and filament width evolutions with time for an NS process (a) and AS process (b) in the network.

3.2.6 Conclusions

In this work, we demonstrated a sleep-dependent memory consolidation in a neuromorphic network formed by Ag@TiO$_2$ nanowires. In analogy with biological neuronal systems, memory arises as a complex interplay between the topological constraints imposed by a complex network and the plasticity of its constituting elements, the memristive nanowire junctions comprising of metal/dielectric/metal interfaces. We investigated a long-term decay of the connectivity in the network by controlling the voltage pulses of different amplitudes and duty ratios. Furthermore, on the basis of the regulated activity cycles during sleep used by the human brain to consolidate memories, we investigated the controllability of the established pathway in the neuromorphic network by introducing a learning-sleep-recovery cycle. We found that the network can quickly restore previous states of conductance after switching off the power source (sleep) when sparse voltage pulses are regularly applied during the sleep. Moreover, controlling the filament decay with periodic pulses during the sleep has the effect of selectively enhancing critical junctions within the network, which were part of a previously used pathway. This allows us to restore the same pathways when a learning or recovery process is resumed. These results provide clues to new learning designs in neuromorphic networks for achieving longer memory retention. By introducing appropriate sleep while providing a sparse but controlled voltage pulse, we may realize parts of a large network with strengthened junctions and effectively retain information, and finally, improve the ability to capture and store information within neuromorphic networks.

3.3 ASSOCIATIVE CURRENT PATHWAY FORMATION IN AG@TIO₂ NANOWIRE NETWORK

3.3.1 Introduction to associative memory

Memories in the brain are not isolated stored but ensemble into associative network[227-229]. In the cellular level, they show synchronous neural activities though in different regions of the brain, indicating linked pathways between memories[230] (neurons wire together fire together). Such association can occur naturally. When memories are encoded close in time, first memory encoding triggers a temporary increase in neuronal excitability that biases the subsequent memory to integrate the memory encoding to the first memory[231-233]. From this, we can easily understand that events happened on the same day are naturally linked together in the human brain. On the other hand, the association can be generated artificially, by consciously training the brain to integrate different memories, for example, classical conditioning and instrumental conditioning [234-235]. One famous physiological study of classical conditioning is known as Pavlov's dog, where the dog shows response (salivation) to the sound of a bell (unconditional stimulus, US) after repeatedly pairing the presentation of the meat (conditional stimulus, CS) with the sound of the bell (Figure 3.16). This study shows the association of memory from the viewpoint of behavioural response where an increased response of the US after pairing it with CS. In a study of cellular responses in mice, associated memories showed overlapped memory trace (the engram cell ensemble which indicates the location of corresponding memory)[234] where shared memory cells link different memory events together. Either naturally generated or artificially generated, we can see, one essential requirement to form memory association is the temporal close stimulus involved during memory encoding, by which the enhanced synaptic strength opens the possibility to link neurons firing together and increases the neuronal connectivity as feedback.
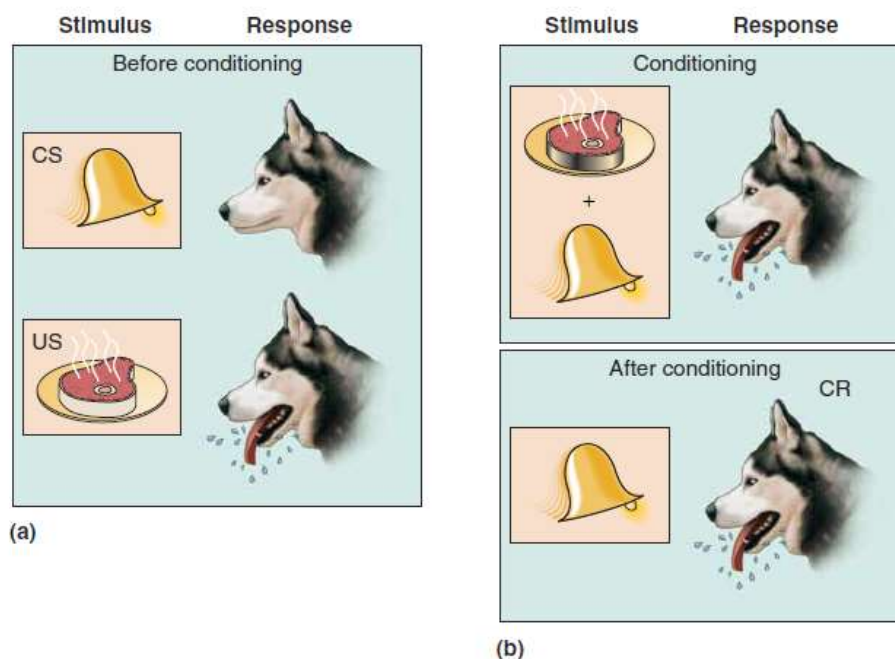
Figure 3.16. Classical conditioning-Pavlov's dog model. (a) Before conditioning, the dog salivates by the sight of a piece of meat (the unconditional stimulus, NS) but has no response by the sound of a bell (the

conditional stimulus, CS). (b) After conditioning, the dog learns to associate sound of bell with meat and will salivate when the bell rings without the meat.[236]
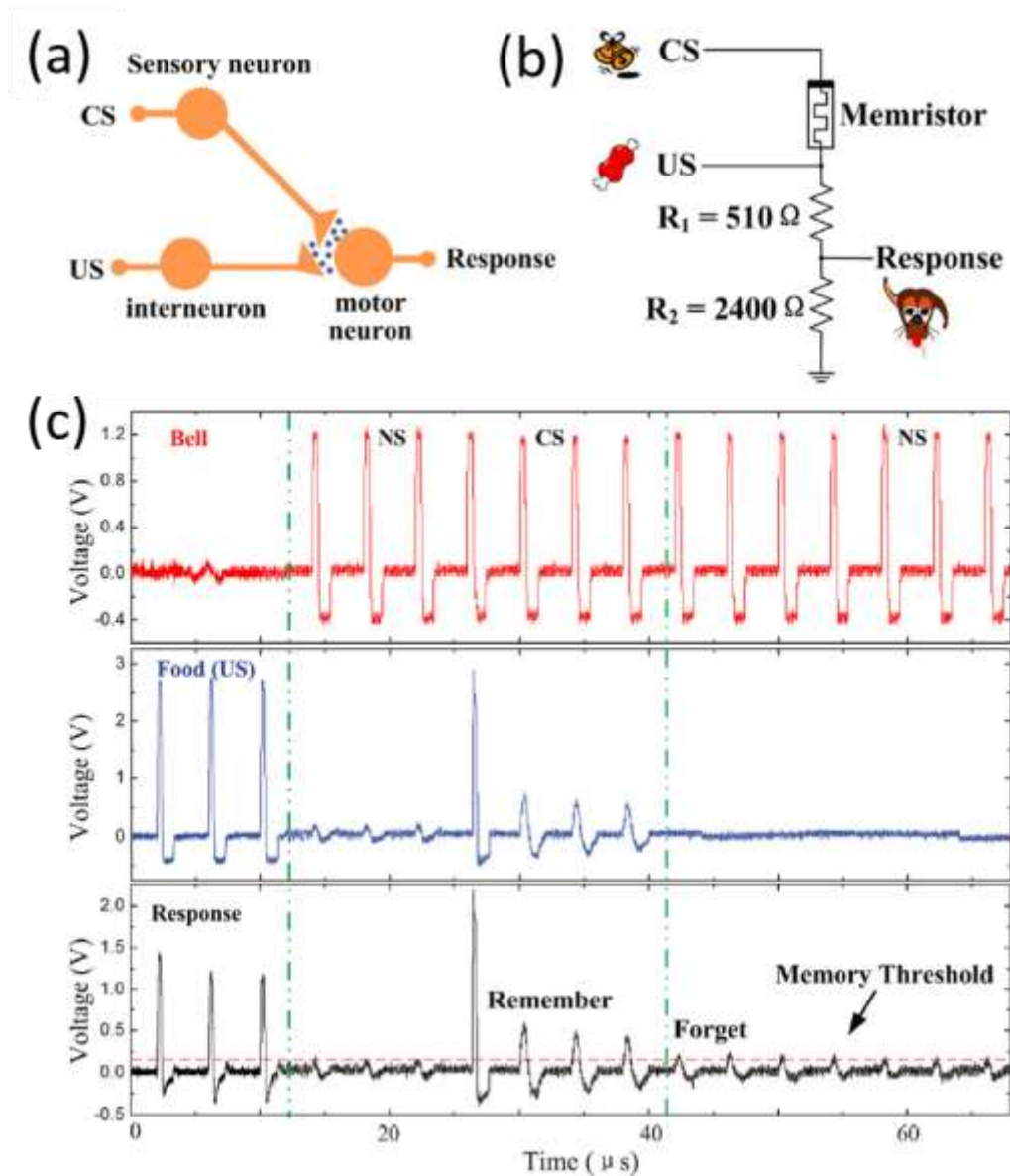
Figure 3.17. Electronic realization of Pavlov's dog learning scheme with one memristor. (a) Illustration of the learning model. (b) The proposed electronic version of the model in (a). (c) Time-dependent voltage inputs (CS and US) and output (response) demonstrating the associative learning scheme in the circuit.[237]

The concept of associative memory already has application in computer science, known as content-addressable memory where memory searching is not based on the physical address but on the similarity or correlation of the content, which allows fast searching and fuzzing address match. In recent years, with the development of artificial intelligence, researches have been seeking possible hardware integration of associative memory[237-244], mainly focusing on the classical conditioning. Figure 3.17 shows the commonly used physical architecture for Pavlov's dog learning scheme integrated with one memristor[237]. The association of the US and NS is established within a temporal window ruled by the STDP and only if the NS inputs after the US the association takes place, which

is in consistence with biological Pavlov's dog learning results. Such architecture requires specially voltage waveform encodings for NS and US to generate a functional threshold voltage-time window to switch on the memristor (Figure 3.17. Electronic realization of Pavlov's dog learning scheme with one memristor. (a) Illustration of the learning model. (b) The proposed electronic version of the model in (a). (c) Time-dependent voltage inputs (CS and US) and output (response) demonstrating the associative learning scheme in the circuit.[237]). Previously in our group, we used artificial neural network formed by memristive nanowire network and achieved associative memory storage and retrieval for 9-bit image[184]. In the random network, nanowires connect randomly, and the memory pattern only depends on the previous spatiotemporal input, these are largely in parallel with associative memory in biological brain morphologically and functionally. It is of fundamental importance to understand how memory associated in the nanowire network. Previous studies have used scanning emission microscopy and thermography for such propose[180-181]. But it was either performed in a high vacuum environment or had low resolutions where current transmission observation even between small groups is not reachable.

In this section, we further introduce a LIT study on visualizing the memory trace in the same memristive nanowire network but with a larger size, in which memory association is naturally formed within the time-dependent training scheme. Lock-in thermography gives high-resolution and sensitive detection of thermal irradiation distribution by lock-in correlating the input periodically pulsed electrical signal with the infrared emission signal from the sample surface. It is a non-destructive method which can perform under different experimental environments. We applied this technique to visualize the infrared irradiation distribution from the Ag@TiO$_2$ nanowire network under electrical stimulation in the ambient condition. The two stimulus input from two different channels and there is one output from the same channel. We show that current pathways, indicating the memory trace, naturally associates partly and modified the memory trace structure at the adjacent point sometimes. With continuous lock-in imaging, we show the dynamical fluctuation of the current pathway and controlling of pathway weight by enhanced stimulus time. The results manifest that pathway association naturally forms in such memristive nanowire network.

3.3.2 Characterization of the nanowire network

The nanowire networks were spin-coated onto glass substrates with pre-patterned Au/Ti electrodes (Figure 3.18). The distance between the counter electrodes is 500 µm, and the electrode width is 40 µm. From the images, we can see most nanowires are forming small or big ensembles and connected by several critical nanowires, together establish multiple connection pathways from one electrode to another.
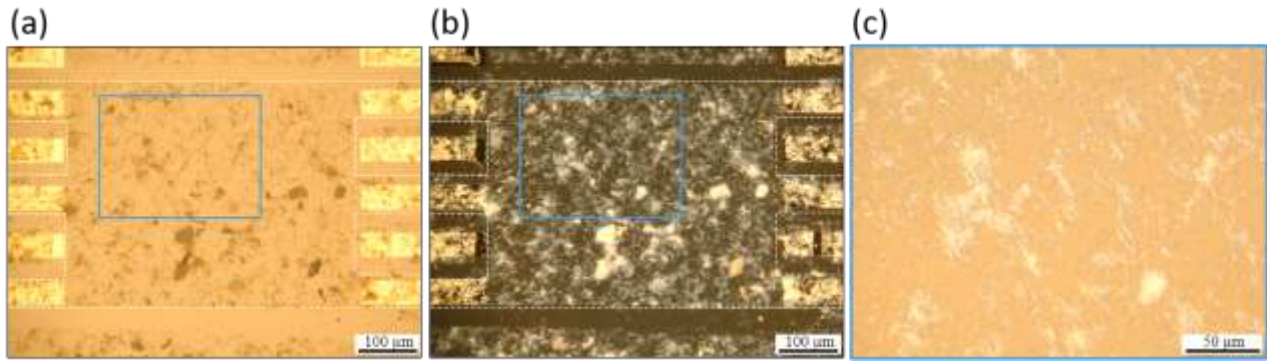
Figure 3.18. Microscopic images of the Ag@TiO₂ nanowire network. (a-b) Bright-field image and corresponding dark filed image. The white dash lines indicate the functional network area. (c) Enlarge image of the blue rectangular part in both (a) and (b).

3.3.3 Visualize current pathway formation with LIT

We took sequential thermal images on the Ag@TiO$_2$ nanowire networks under current stimulus with LIT (Figure A-1)[245-246]. Figure 3.19a shows the experimental setup, and periodical current pulses are injected to the nanowire network, during which a thermal camera images the network continuously and send the signals to the computer to perform lock-in process. In a typical LIT test, we can obtain three images simultaneously for each imaging process: steady-state thermograph which give topographic information of the device under test, lock-in thermal amplitude image which indicates the sensitive thermal distribution and a lock-in phase image demonstrating the thermal dissipation in the device. Figure 3.19 c-d show the corresponding images of our Ag@TiO$_2$ nanowire network under periodical current stimulus with a spatial resolution of 2 µm. The current inputs switched equally between 1 µA and 0 µA with a speed of 10 Hz (Keithley 2410 SourceMeter). Voltage compliance of 1000 V was applied to avoid break-down the nanowires, and the integration time for each image process was 10 s. From lock-in amplitude (phase images), exact collective red spots (green feature) connect the source and the ground in the network, implying there is current transmission through the network. When current inputs from one side of the nanowire network, Ag aggregates in the TiO$_2$ of the nanowire-nanowire junctions (in the form of Ag/TiO$_2$/Ag) to form conductive filaments and connect nanowires to form a current pathway between electrodes. This results in an increase of thermal temperature of nanowires along the current pathway due to joule heat, leading high intensity of infrared emissions along the current transmission ways. For junctions along the current pathway with high resistances, under Joule-Lenz law, generate larger heat and irradiate higher intensity of infrared light. This can be observed after overlapping the lock-in amplitude image to the topographic image (Figure 3.19d) that at red spots locate at low density area and seem to bridge the nearby nanowire clusters to form a complete pathway. We conclude that lock-in thermal images show parallel information of the current transmission in our Ag@TiO$_2$ nanowire network.
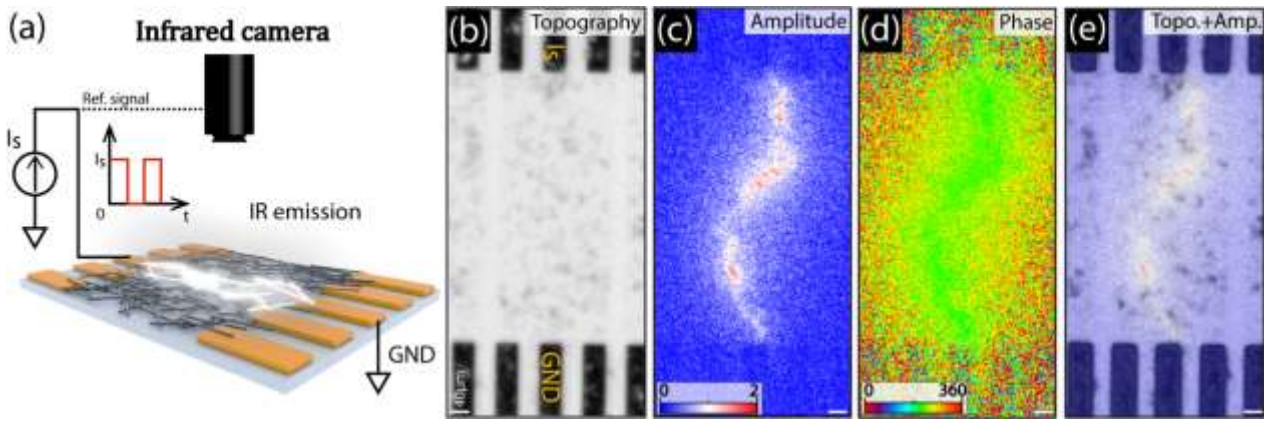
Figure 3.19. Lock-in thermography to visualize current pathway. (a) Experimental set-up. Nanowire network on glass substrate were terminated by one periodical current source and ground. Nanowires along the current transmission pathway are colored as white. An infrared camera collects the infrared emissions from the network surface and sends the signals to computer for lock-in process. (b-d) Images obtained during LIT test of the Ag@TiO₂ nanowire network: topography (steady-state thermal image) (b), lock-in amplitude image (c) and lock-in phase image (d). I_s = 1μA (1 Hz, duty: 50%), voltage compliance = 1000V and the image integration time = 10 s. (e) Overlapped image of topography and amplitude. Scale bar: 40μm.
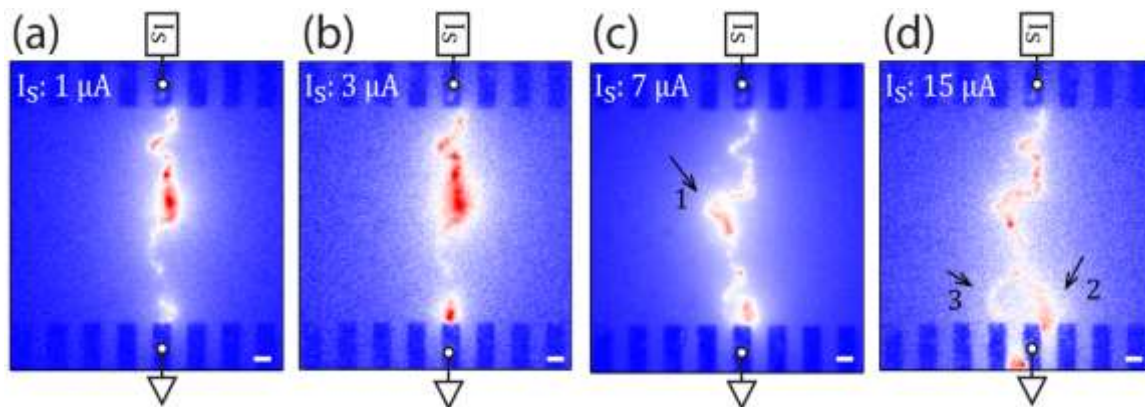
Figure 3.20. Formation and expansion of current pathway. Lock-in amplitude images with an increase in current source of the Ag@TiO₂ nanowire network. I_s = 1 μA(a), 3 μA(b), 7 μA(c), 15 μA(d) (1 Hz, duty: 50%), voltage compliance = 1000 V and the image integration time = 10 s. Scale bar: 40 μm.

With LIT, we first explored the formation and expansion of current pathway in a new network with an increase in current source input, the results are shown in Figure 3.20. When the input current source is small, only one steady current pathway appears (Figure 3.20 a and b). As the input current increases, new pathway branches appear (indicated by arrows 1, 2 and 3). The old pathway branches could not be observed clearly in the images, which may be limited by the spatial resolution of the camera. The observed features can be expected by considering the growing number of conductive Ag/TiO₂/Ag junctions in the network (Figure 3.14 in section 3.2). With the different field potentials actual working in the different junctions, Ag filaments grow in different speed. Therefore pathway which needs the lowest activation energy will form first, in the lock-in amplitude image it shows up first. The results are consistent with the "winner-takes-all" model proposed by Manning et al[181]. As the current flow in the network reaches the setting value, the voltage applied between the source and the ground starts to decrease. The decreasing voltage keeps the Ag filaments that are in the junctions along the current transmission pathway but prohibits or reduces the growth of Ag filaments in other

junctions, resulting in current transmission only through pathways first reach conductive state (winner-takes-all).

3.3.4 Associative current pathways in Ag@TiO$_2$ nanowire network

Memory association is one primary function and naturally happens in the biological brains, owing to the high connectivity between neurons and time-dependent plasticity at each neuronal contact point -- synapse. During association, the memory traces, an exciting neuronal ensemble which is believed as the location where memory stores, for different learning events merge partially or open new connecting paths, depending on the learning scheme[229-230, 233-234]. Our Ag@TiO$_2$ nanowire network exhibits complex connectivity feature similar to the biological brain and has functional time-dependent connectivity plasticity at the nanowire-nanowire junction, is a promising platform to study the memory association in a physical device. We did the study on the nanowire network with two input terminals by altering the current input channel(s) sequentially and recording dynamical lock-in thermal images simultaneously. The nanowire network acts as the nervous system and its two terminals accepting stimulus signals (periodical current pulses) can be considered as different senses (for example, eyes and nose) receiving information encoding. The current pathways imaged by the LIT can be considered as the memory trace which stores the sensing stimulus information.

The results are shown in Figure 3.21. The current was first injected from terminal X, opening current pathways as showing in Figure 3.21b. When altering the input channel to a different terminal Y (immediately after X), the current transmission did not open a completely new one but shared partial pathway with previous activated one (X) from the middle part to the ground electrode (Figure 3.21c). The pathway overlap between two individual tests indicates a memory association between two signals from the two terminals. After activating the network from terminal X, Ag filaments formed in the junctions along the current pathway and retained, biasing the current transmission from terminal Y to flow along the existing high conductive pathway. A similar mechanism can be applied when the current inputted from both terminals after Y, the lock-in thermal image (Figure 3.21d) merges the feature of the two individually obtained pathways due to pathway retention from historical stimulations in the network. The results show many equivalent features as the time-correlated memory association in the biological systems, especially for memories stored morphologically close.

Figure 3.21d also indicates parallel current transmission from both terminals, which usually occurs when conductance states of the pathways are comparable. This is a rare case in our nanowire network tests. Furthermore, in the biological system, since the first learning memory can be easily interrupted or erased by new coming information, a strong association of memories requires repeated learning, for example, classical conditional learning. We show below that the asymmetric conductive pathways between two terminals can be improved by increasing the stimulation period from the weak terminal.

Figure 3.22 show sequential lock-in amplitude images for a training test. The current transmission pathway was formed after continuous injecting periodical current pulse for 40 s from terminal Y. One intermediate sate is shown in Figure 3.22 b, with only several thermal dots observed. The associated pathway was formed immediately after switching the input terminal (to X), similar to Figure 3.21 c. However, when input from both terminals (Figure 3.22 e) current pathways only copied the shape from terminal Y, indicating current only transmitted from this terminal. The technique used to strengthen the pathway from terminal X was by continues applying current stimulus from the terminal (for 55 s), to imitate the highly concentrated forced learning in the human learning

experience. The result was quite efficient as shown in Figure 3.22 h that parallel pathways observed from both terminals.

We showed above how forced training changes the current transmission pattern from two inputs. However, the mechanism lying behind our Ag@TiO$_2$ nanowire network is quite different from that of a biological system. Current transmission in our network obeys strict physical laws, from high electrical potential to low electrical potential, while in nervous system signal transmission combines chemical-physical conversion acting under the integrate-and-firing scheme. However, at the individual junction (synapse), the time-dependent plasticity plays the crucial role in pathway (memory trace) formation, the same in the two systems.
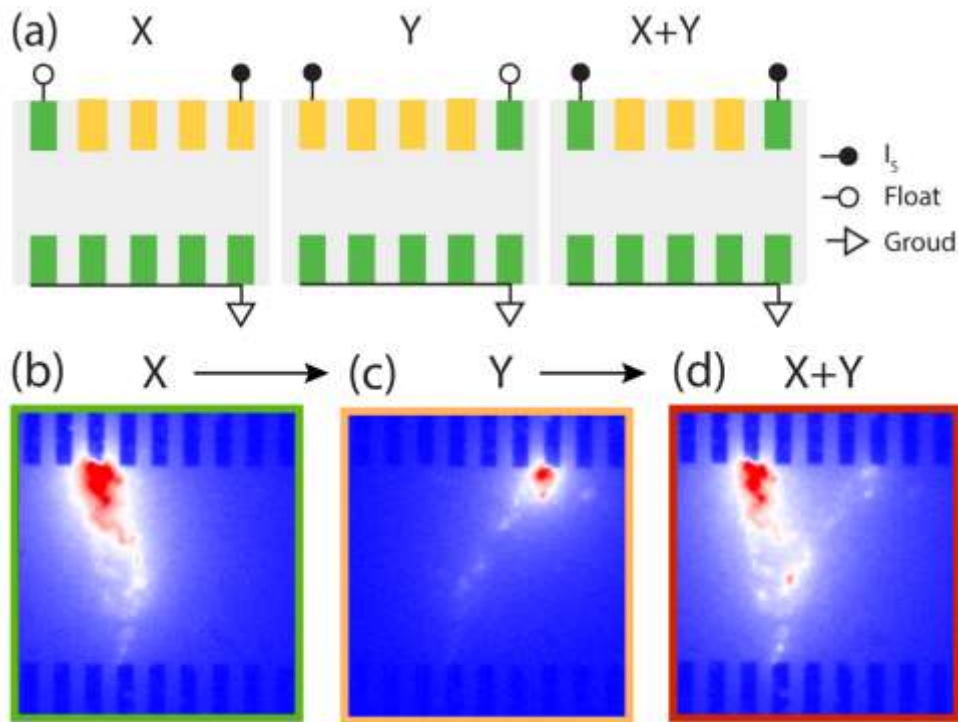
Figure 3.21. Lock-in amplitude images of the network while switching the input between two input electrodes. (a) Electrical setups for different measurements. From left to right: input only from channel X, input only from channel Y and input from both X and Y channels. All the counter electrodes were grounded. (b-d) Associative routing between two input channels. The source channel was changed sequentially as image order. $I_s = 5\mu A$ (1 Hz, duty: 50%), voltage compliance = 800V and the image integration time = 5 s.
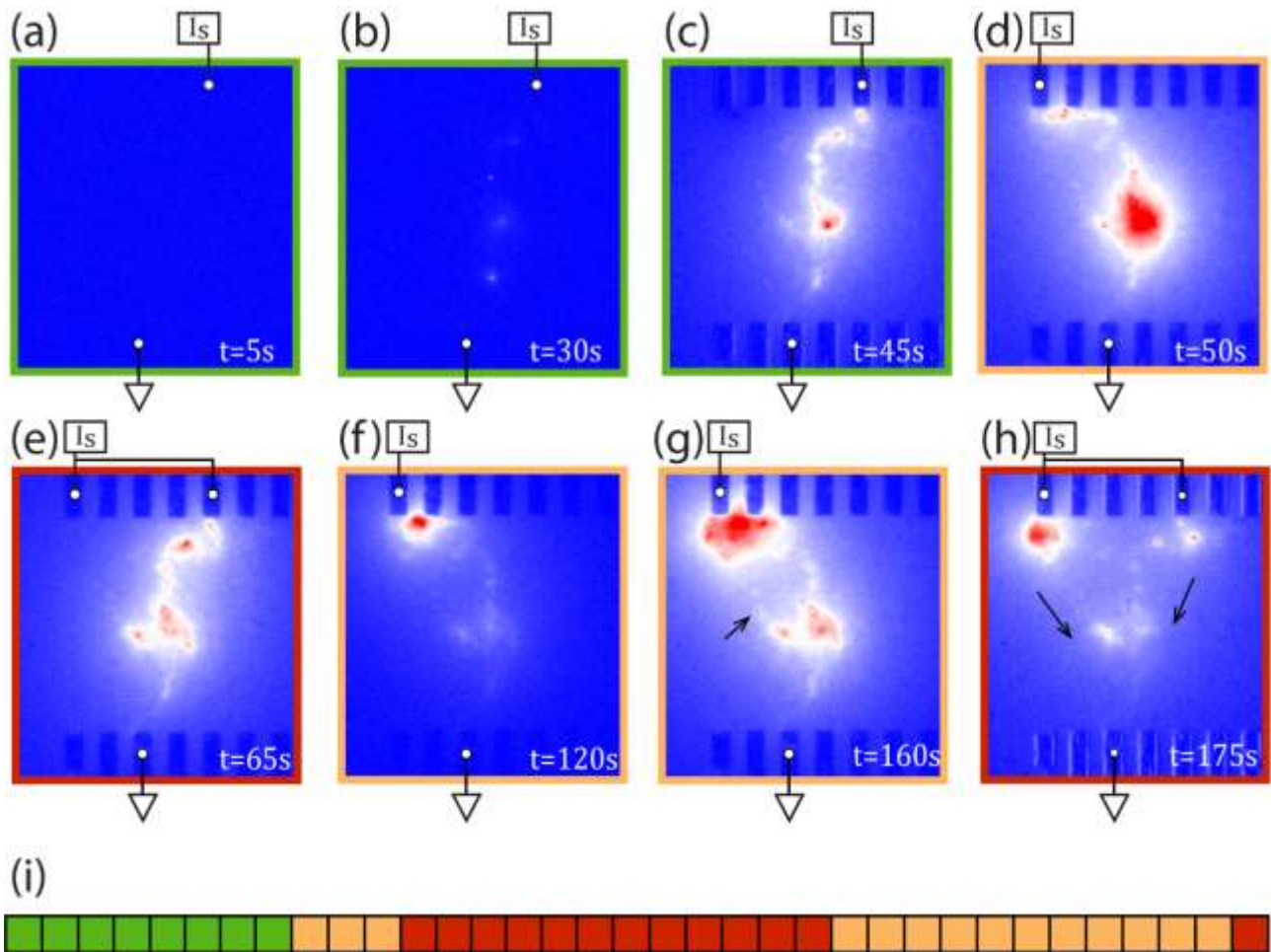
Figure 3.22. A record of lock-in amplitude images of the network while switching the input between two input electrodes. Image edge and its input correlate in the following way: green(X), orange(Y) and red-(X+Y). (a-c) A pathway is formed between source and ground electrodes. (d) New pathway is formed quickly after switching the input electrode. (e) Only pathway from one channel was shown when input from 2 channels. (f-g) Training one channel by continues input current for a time period. (h) Pathways from both channels were shown when input from 2 channels. $I_s = 5$ µA (1 Hz, duty: 50%), voltage compliance = 600 V and the image integration time = 5 s. (i) Input time line for the record. Each color pixel indicate corresponding input event for 5 s.

3.3.5 Conclusions

In this section, we imaged the current pathway in the Ag@TiO$_2$ nanowire network with the high-performance LIT. We demonstrated the current expansion in the network, revealing a "winner-takes-all" formation scheme. By terminating the nanowire network with two inputs, we observed clear current pathway association in the network structure. Pathway association formed naturally, and the strength of association can be modified by forced training.

Chapter 4: Summary and prospect

Integration of nanomaterials would be necessary for all ranges of nanomaterials that have or not have been discovered. The outstanding or ordinary features in these integrated systems pave the way for high performance and energy-efficient systems in the future. In this thesis, I picked up two different integrated nanosystems, graphene integrated with the microstructured substrate and self-assembled memristive nanowire system, for each is a representative integration architecture in this field. In chapter 1, we introduced the background of the general integrated nanomaterials and reviewed a short history and specific aspects of the application related to our integrated nanosystems. In chapter 2, we presented the experimental methods applied in this thesis. A wet transfer method of graphene to any substrate and a hydrothermal method to synthesis high-quality Ag@TiO$_2$ nanowires were included. For the physical measurement part, we briefly introduce the mechanism of Raman spectroscopy and two-wire method for the electrical test; these two are frequently used for material characterization and electrical properties measurement. We showed more detailed information on the working principle of LIT, which is a sensitive thermal detection technique emerging in recent years and we first applied it in the thesis to detect the current fluctuation with high spatial resolution in the memristive system. Chapters 1 and 2 give a general understanding of the two integrated systems and lead the reader to specified physical properties we mainly contributed in chapter 3.

In chapter 3, three emergent physical properties of the integrated systems were presented. The first section describes the micro-Raman study of graphene/micro-cavity system, including five parts from background to experimental and theoretical discussions. The second and third sections are about the Ag@TiO$_2$ nanowire network system. We had a relatively comprehensive study on such system, showing the sample characterization, memristive IV behaviours and spiking-time memory learning and forgetting. Besides, we particularly studied the sleep-dependent memory consolidation process and associative memory in such network system, to mimic the biological brain's functionalities. The main results in chapter 3 are as follows:

★ Raman laser interaction within the cavity was projected onto the graphene sheet. This results in the formation of concentric rings in nanoscale on its Raman intensity mapping on the suspended graphene area, revealing Raman intensity oscillation from the edge of the suspended area to the central. Though no clear evidence shown for electronic modification on the graphene sheet in such drum architecture, we expect further application on graphene sheet to sense the underlying cavity structure. Furthermore, the same phenomena may be observed on other 2D materials with cavity structure and used to modify the electronic state of materials which are sensitive to thermal heating.

★ We demonstrated a sleep-dependent memory consolidation in a neuromorphic network formed by Ag@TiO$_2$ nanowires. In analogy with biological neuronal systems, memory arises as a complex interplay between the topological constraints imposed by a complex network and the plasticity of its constituting elements, the memristive nanowire junctions comprising of metal/dielectric/metal interfaces. We investigated a long-term decay of the connectivity in the network by controlling the voltage pulses of different amplitudes and duty ratios. Furthermore, based on the regulated activity cycles during sleep used by the human brain to consolidate memories, we investigated the controllability of the established pathway in the neuromorphic network by introducing a learning-sleep-recovery cycle. We found that the network can quickly restore previous

states of conductance after switching off the power source (sleep) when sparse voltage pulses are regularly applied during the sleep. Moreover, controlling the filament decay with periodic pulses during the sleep has the effect of selectively enhancing critical junctions within the network, which were part of a previously used pathway. This allows us to restore the same pathways when a learning or recovery process is resumed. These results provide clues to new learning designs in neuromorphic networks for achieving longer memory retention. By introducing appropriate sleep while providing a sparse but controlled voltage pulse, we may realize parts of a large network with strengthened junctions and effectively retain information, and finally, improve the ability to capture and store information within neuromorphic networks.

★ We visualized the current pathway in the Ag@TiO$_2$ nanowire network with the high-performance LIT. We demonstrated the current expansion in the network, revealing a "winner-takes-all" formation scheme. By terminating the nanowire network with two inputs, we observed clear current pathway association in the network structure. Pathway association formed naturally and the strength of association can be modified by forced training.

In conclusion, through my PhD research works on the two different integrated nanosystems, I have convinced that integrating or self-assembling different nanomaterials and other materials/structures is an important and promising direction we should take for the future. Although this thesis describes only a part of possibilities, I believe that the results and discussion would contribute to a new realm of nanotechnology and nano architectonics. However, in the future research on these two integrated systems, there are several points we should carefully consider:

★ Graphene as the first experimental obtained 2D materials has attracted numerous attention and been widely studied in the past decades. It has been marked as the materials of the future and triggered the research boom of other 2D materials like transition metal dichalcogenides (MoS2). However, practical applications of the graphene-integrated system in electronic device are still under debate, which due to its intrinsic semi-metal feature. Approaches to integrated graphene with other materials or other morphology have opened a new aspect to graphene engineering. Taking account the Raman oscillation rings observed on graphene/micro-cavity structure, substrate engineering in graphene or 2D materials can be a promising direction.

★ For the memristive nanowire system, we should state that in biological neural system neuron and synapse has more complex structure and functions. The out layer of the axon is covered with myelin which is insulating. Neural synapse can be either inhibitive or excitatory, increase the complexity of the whole neural system. Our efforts to use memristive nanowire network to achieve brain-like functionalities are only very small or preliminary results of the approach. Materials designing should not only limit in solid-state materials, but interdisciplinary material integration and method should also be considered. On the other side, circuit designing to emulate the function to different types of biological synapse/neurons could also help for achieving neuromorphic computing.

★ Another aspect of neuromorphic computing, for cross-bar architecture and random network architecture, both applications are based on the development of soft AI, where training frame and algorithm play an essential role. To the specific reservoir computing, the promising LIF or Hodgkin-Huxley model is not applicable for current memristive materials. More efforts on such direction should be considered.

★ However, we would see the potential of the random network in understating or emulating the brain's functionalities, in the future work, we may more focus on the biological emulating and take it as a platform to grasp the secrets of the biological brain.

Reference

1. Prum, R. O.; Quinn, T.; Torres, R. H., Anatomically diverse butterfly scales all produce structural colours by coherent scattering. *Journal of Experimental Biology* **2006,** *209* (4), 748-765.

2. Butt, H.; Yetisen, A. K.; Mistry, D.; Khan, S. A.; Hassan, M. U.; Yun, S. H., Morpho Butterfly-Inspired Nanostructures. *Adv Opt Mater* **2016,** *4* (4), 497-504.

3. Autumn, K.; Liang, Y. A.; Hsieh, S. T.; Zesch, W.; Chan, W. P.; Kenny, T. W.; Fearing, R.; Full, R. J., Adhesive force of a single gecko foot-hair. *Nature* **2000,** *405* (6787), 681-685.

4. Autumn, K.; Majidi, C.; Groff, R. E.; Dittmore, A.; Fearing, R., Effective elastic modulus of isolated gecko setal arrays. *Journal of Experimental Biology* **2006,** *209* (18), 3558-3568.

5. Geim, A. K.; Dubonos, S. V.; Grigorieva, I. V.; Novoselov, K. S.; Zhukov, A. A.; Shapoval, S. Y., Microfabricated adhesive mimicking gecko foot-hair. *Nature Materials* **2003,** *2* (7), 461-463.

6. Boehm, H. P.; Setton, R.; Stumpp, E., Nomenclature and terminology of graphite intercalation compounds. *Carbon* **1986,** *24* (2), 241-245.

7. Wallace, P. R., The Band Theory of Graphite. *Physical Review* **1947,** *71* (9), 622-634.

8. Semenoff, G. W., Condensed-Matter Simulation of a Three-Dimensional Anomaly. *Phys Rev Lett* **1984,** *53* (26), 2449-2452.

9. Haldane, F. D. M., Model for a Quantum Hall Effect without Landau Levels: Condensed-Matter Realization of the "Parity Anomaly". *Phys Rev Lett* **1988,** *61* (18), 2015-2018.

10. Evans, J. W.; Thiel, P. A.; Bartelt, M. C., Morphological evolution during epitaxial thin film growth: Formation of 2D islands and 3D mounds. *Surf Sci Rep* **2006,** *61* (1), 1-128.

11. Novoselov, K. S.; Geim, A. K.; Morozov, S. V.; Jiang, D.; Zhang, Y.; Dubonos, S. V.; Grigorieva, I. V.; Firsov, A. A., Electric Field Effect in Atomically Thin Carbon Films. *Science* **2004,** *306* (5696), 666-669.

12. Novoselov, K. S., Nobel Lecture: Graphene: Materials in the Flatland. *Rev Mod Phys* **2011,** *83* (3), 837-849.

13. Bolotin, K. I.; Sikes, K. J.; Jiang, Z.; Klima, M.; Fudenberg, G.; Hone, J.; Kim, P.; Stormer, H. L., Ultrahigh electron mobility in suspended graphene. *Solid State Commun* **2008,** *146* (9), 351-355.

14. Ghosh, S.; Calizo, I.; Teweldebrhan, D.; Pokatilov, E. P.; Nika, D. L.; Balandin, A. A.; Bao, W.; Miao, F.; Lau, C. N., Extremely high thermal conductivity of graphene: Prospects for thermal management applications in nanoelectronic circuits. *Applied Physics Letters* **2008,** *92* (15), 151911.

15. Balandin, A. A.; Ghosh, S.; Bao, W.; Calizo, I.; Teweldebrhan, D.; Miao, F.; Lau, C. N., Superior Thermal Conductivity of Single-Layer Graphene. *Nano Letters* **2008,** *8* (3), 902-907.

16. Lee, C.; Wei, X.; Kysar, J. W.; Hone, J., Measurement of the Elastic Properties and Intrinsic Strength of Monolayer Graphene. *Science* **2008,** *321* (5887), 385-388.

17. Jiang, D.-e.; Cooper, V. R.; Dai, S., Porous Graphene as the Ultimate Membrane for Gas Separation. *Nano Letters* **2009,** *9* (12), 4019-4024.

18. Nair, R. R.; Blake, P.; Grigorenko, A. N.; Novoselov, K. S.; Booth, T. J.; Stauber, T.; Peres, N. M. R.; Geim, A. K., Fine Structure Constant Defines Visual Transparency of Graphene. *Science* **2008,** *320* (5881), 1308-1308.

19. Yi, M.; Shen, Z., A review on mechanical exfoliation for the scalable production of graphene. *Journal of Materials Chemistry A* **2015,** *3* (22), 11700-11715.

20. Hernandez, Y.; Nicolosi, V.; Lotya, M.; Blighe, F. M.; Sun, Z.; De, S.; McGovern, I. T.; Holland, B.; Byrne, M.; Gun'Ko, Y. K.; Boland, J. J.; Niraj, P.; Duesberg, G.; Krishnamurthy, S.; Goodhue, R.; Hutchison, J.; Scardaci, V.; Ferrari, A. C.; Coleman, J. N., High-yield production of graphene by liquid-phase exfoliation of graphite. *Nature Nanotechnology* **2008,** *3* (9), 563-568.

21. Wang, M.; Jang, S. K.; Jang, W.-J.; Kim, M.; Park, S.-Y.; Kim, S.-W.; Kahng, S.-J.; Choi, J.-Y.; Ruoff, R. S.; Song, Y. J.; Lee, S., A Platform for Large-Scale Graphene Electronics – CVD Growth of Single-Layer Graphene on CVD-Grown Hexagonal Boron Nitride. *Advanced Materials* **2013,** *25* (19), 2746-2752.

22. Wu, T.; Zhang, X.; Yuan, Q.; Xue, J.; Lu, G.; Liu, Z.; Wang, H.; Wang, H.; Ding, F.; Yu, Q.; Xie, X.; Jiang, M., Fast growth of inch-sized single-crystalline graphene from a controlled single nucleus on Cu–Ni alloys. *Nature Materials* **2016,** *15* (1), 43-47.

23. Tang, S.; Wang, H.; Wang, H. S.; Sun, Q.; Zhang, X.; Cong, C.; Xie, H.; Liu, X.; Zhou, X.; Huang, F.; Chen, X.; Yu, T.; Ding, F.; Xie, X.; Jiang, M., Silane-catalysed fast growth of large single-crystalline graphene on hexagonal boron nitride. *Nature Communications* **2015,** *6* (1), 6499.

24. Dean, C. R.; Young, A. F.; Meric, I.; Lee, C.; Wang, L.; Sorgenfrei, S.; Watanabe, K.; Taniguchi, T.; Kim, P.; Shepard, K. L.; Hone, J., Boron nitride substrates for high-quality graphene electronics. *Nature Nanotechnology* **2010,** *5* (10), 722-726.

25. Neumaier, D.; Pindl, S.; Lemme, M. C., Integrating graphene into semiconductor fabrication lines. *Nature Materials* **2019,** *18* (6), 525-529.

26. Wang, T.; Huang, D.; Yang, Z.; Xu, S.; He, G.; Li, X.; Hu, N.; Yin, G.; He, D.; Zhang, L., A Review on Graphene-Based Gas/Vapor Sensors with Unique Properties and Potential Applications. *Nano-Micro Letters* **2016,** *8* (2), 95-119.

27. Liao, L.; Duan, X., Graphene for radio frequency electronics. *Mater Today* **2012,** *15* (7), 328-338.

28. Secor, E. B.; Lim, S.; Zhang, H.; Frisbie, C. D.; Francis, L. F.; Hersam, M. C., Gravure Printing of Graphene for Large-area Flexible Electronics. *Advanced Materials* **2014,** *26* (26), 4533-4538.

29. Stanford, M. G.; Zhang, C.; Fowlkes, J. D.; Hoffman, A.; Ivanov, I. N.; Rack, P. D.; Tour, J. M., High-Resolution Laser-Induced Graphene. Flexible Electronics beyond the Visible Limit. *ACS Applied Materials & Interfaces* **2020,** *12* (9), 10902-10907.

30. Smith, A. D.; Niklaus, F.; Paussa, A.; Vaziri, S.; Fischer, A. C.; Sterner, M.; Forsberg, F.; Delin, A.; Esseni, D.; Palestri, P.; Östling, M.; Lemme, M. C., Electromechanical Piezoresistive Sensing in Suspended Graphene Membranes. *Nano Letters* **2013,** *13* (7), 3237-3242.

31. Romagnoli, M. In *Graphene Photonics for Optical Communications*, 2019 Optical Fiber Communications Conference and Exhibition (OFC), 3-7 March 2019; 2019; pp 1-3.

32. Yu, T.; Ni, Z.; Du, C.; You, Y.; Wang, Y.; Shen, Z., Raman Mapping Investigation of Graphene on Transparent Flexible Substrate: The Strain Effect. *The Journal of Physical Chemistry C* **2008,** *112* (33), 12602-12605.

33. Lanza, M.; Wang, Y.; Bayerl, A.; Gao, T.; Porti, M.; Nafria, M.; Liang, H.; Jing, G.; Liu, Z.; Zhang, Y.; Tong, Y.; Duan, H., Tuning graphene morphology by substrate towards wrinkle-free devices: Experiment and simulation. *Journal of Applied Physics* **2013,** *113* (10), 104301.

34. Ong, Z.-Y.; Pop, E., Effect of substrate modes on thermal transport in supported graphene. *Phys Rev B* **2011,** *84* (7), 075471.

35. Zhou, S. Y.; Gweon, G. H.; Fedorov, A. V.; First, P. N.; de Heer, W. A.; Lee, D. H.; Guinea, F.; Castro Neto, A. H.; Lanzara, A., Substrate-induced bandgap opening in epitaxial graphene. *Nature Materials* **2007,** *6* (10), 770-775.

36. Plutnar, J.; Pumera, M.; Sofer, Z., The chemistry of CVD graphene. *Journal of Materials Chemistry C* **2018,** *6* (23), 6082-6101.

37. Losurdo, M.; Giangregorio, M. M.; Capezzuto, P.; Bruno, G., Graphene CVD growth on copper and nickel: role of hydrogen in kinetics and structure. *Physical Chemistry Chemical Physics* **2011,** *13* (46), 20836-20843.

38. Yan, Z.; Lin, J.; Peng, Z.; Sun, Z.; Zhu, Y.; Li, L.; Xiang, C.; Samuel, E. L.; Kittrell, C.; Tour, J. M., Toward the Synthesis of Wafer-Scale Single-Crystal Graphene on Copper Foils. *ACS Nano* **2012,** *6* (10), 9110-9117.

39. Kang, C.; Jung, D. H.; Lee, J. S., Atmospheric Pressure Chemical Vapor Deposition of Graphene Using a Liquid Benzene Precursor. *Journal of nanoscience and nanotechnology* **2015,** *15* (11), 9098-9103.

40. Zhang, B.; Lee, W. H.; Piner, R.; Kholmanov, I.; Wu, Y.; Li, H.; Ji, H.; Ruoff, R. S., Low-Temperature Chemical Vapor Deposition Growth of Graphene from Toluene on Electropolished Copper Foils. *ACS Nano* **2012,** *6* (3), 2471-2476.

41. Jang, J.; Son, M.; Chung, S.; Kim, K.; Cho, C.; Lee, B. H.; Ham, M.-H., Low-temperature-grown continuous graphene films from benzene by chemical vapor deposition at ambient pressure. *Scientific Reports* **2015,** *5* (1), 17955.

42. Reina, A.; Thiele, S.; Jia, X.; Bhaviripudi, S.; Dresselhaus, M. S.; Schaefer, J. A.; Kong, J., Growth of large-area single- and Bi-layer graphene by controlled carbon precipitation on polycrystalline Ni surfaces. *Nano Research* **2009,** *2* (6), 509-516.

43. Zhang, Y.; Gomez, L.; Ishikawa, F. N.; Madaria, A.; Ryu, K.; Wang, C.; Badmaev, A.; Zhou, C., Comparison of Graphene Growth on Single-Crystalline and Polycrystalline Ni by Chemical Vapor Deposition. *The Journal of Physical Chemistry Letters* **2010,** *1* (20), 3101-3107.

44. Weatherup, R. S.; Dlubak, B.; Hofmann, S., Kinetic Control of Catalytic CVD for High-Quality Graphene at Low Temperatures. *ACS Nano* **2012,** *6* (11), 9996-10003.

45. Liu, N.; Fu, L.; Dai, B.; Yan, K.; Liu, X.; Zhao, R.; Zhang, Y.; Liu, Z., Universal Segregation Growth Approach to Wafer-Size Graphene from Non-Noble Metals. *Nano Letters* **2011,** *11* (1), 297-303.

46. Chen, S.; Cai, W.; Piner, R. D.; Suk, J. W.; Wu, Y.; Ren, Y.; Kang, J.; Ruoff, R. S., Synthesis and Characterization of Large-Area Graphene and Graphite Films on Commercial Cu–Ni Alloy Foils. *Nano Letters* **2011,** *11* (9), 3519-3525.

47. Zhu, M.; Du, Z.; Yin, Z.; Zhou, W.; Liu, Z.; Tsang, S. H.; Teo, E. H. T., Low-Temperature in Situ Growth of Graphene on Metallic Substrates and Its Application in Anticorrosion. *ACS Applied Materials & Interfaces* **2016,** *8* (1), 502-510.

48. Grodecki, K.; Blaszczyk, J. A.; Strupinski, W.; Wysmolek, A.; Stępniewski, R.; Drabinska, A.; Sochacki, M.; Dominiak, A.; Baranowski, J. M., Pinned and unpinned epitaxial graphene layers on SiC studied by Raman spectroscopy. *Journal of Applied Physics* **2012,** *111* (11), 114307.

49. Strupinski, W.; Grodecki, K.; Wysmolek, A.; Stepniewski, R.; Szkopek, T.; Gaskell, P. E.; Grüneis, A.; Haberer, D.; Bozek, R.; Krupka, J.; Baranowski, J. M., Graphene Epitaxy by Chemical Vapor Deposition on SiC. *Nano Letters* **2011,** *11* (4), 1786-1791.

50. Michon, A.; Vézian, S.; Roudon, E.; Lefebvre, D.; Zielinski, M.; Chassagne, T.; Portail, M., Effects of pressure, temperature, and hydrogen during graphene growth on SiC(0001) using propane-hydrogen chemical vapor deposition. *Journal of Applied Physics* **2013,** *113* (20), 203501.

51. Zhuo, Q.-Q.; Wang, Q.; Zhang, Y.-P.; Zhang, D.; Li, Q.-L.; Gao, C.-H.; Sun, Y.-Q.; Ding, L.; Sun, Q.-J.; Wang, S.-D.; Zhong, J.; Sun, X.-H.; Lee, S.-T., Transfer-Free Synthesis of Doped and Patterned Graphene Films. *ACS Nano* **2015,** *9* (1), 594-601.

52. Ma, Y.; Jang, H.; Kim, S. J.; Pang, C.; Chae, H., Copper-Assisted Direct Growth of Vertical Graphene Nanosheets on Glass Substrates by Low-Temperature Plasma-Enhanced Chemical Vapour Deposition Process. *Nanoscale Res Lett* **2015,** *10* (1), 308.

53. Fujita, J.-i.; Hiyama, T.; Hirukawa, A.; Kondo, T.; Nakamura, J.; Ito, S.-i.; Araki, R.; Ito, Y.; Takeguchi, M.; Pai, W. W., Near room temperature chemical vapor deposition of graphene with diluted methane and molten gallium catalyst. *Scientific Reports* **2017,** *7* (1), 12371.

54. Dolleman, R. J.; Davidovikj, D.; Cartamil-Bueno, S. J.; van der Zant, H. S. J.; Steeneken, P. G., Graphene Squeeze-Film Pressure Sensors. *Nano Letters* **2016,** *16* (1), 568-571.

55. Chen, C.; Rosenblatt, S.; Bolotin, K. I.; Kalb, W.; Kim, P.; Kymissis, I.; Stormer, H. L.; Heinz, T. F.; Hone, J., Performance of monolayer graphene nanomechanical resonators with electrical readout. *Nature Nanotechnology* **2009,** *4* (12), 861-867.

56. Davidovikj, D.; Slim, J. J.; Cartamil-Bueno, S. J.; van der Zant, H. S. J.; Steeneken, P. G.; Venstra, W. J., Visualizing the Motion of Graphene Nanodrums. *Nano Letters* **2016,** *16* (4), 2768-2773.

57. De Alba, R.; Massel, F.; Storch, I. R.; Abhilash, T. S.; Hui, A.; McEuen, P. L.; Craighead, H. G.; Parpia, J. M., Tunable phonon-cavity coupling in graphene membranes. *Nature Nanotechnology* **2016,** *11*, 741.

58. Inoue, T.; Anno, Y.; Imakita, Y.; Takei, K.; Arie, T.; Akita, S., Resonance Control of a Graphene Drum Resonator in a Nonlinear Regime by a Standing Wave of Light. *ACS Omega* **2017,** *2* (9), 5792-5797.

59. Barton, R. A.; Storch, I. R.; Adiga, V. P.; Sakakibara, R.; Cipriany, B. R.; Ilic, B.; Wang, S. P.; Ong, P.; McEuen, P. L.; Parpia, J. M.; Craighead, H. G., Photothermal Self-Oscillation and Laser Cooling of Graphene Optomechanical Systems. *Nano Letters* **2012,** *12* (9), 4681-4686.

60. Davy, H., Additional experiments on galvanic elecricity. *A Journal of Natural Philosophy, Chemistry and the Arts* **1800,** *4*, 326.

61. Prodromakis, T.; Toumazou, C.; Chua, L., Two centuries of memristors. *Nature Materials* **2012,** *11* (6), 478-481.

62. Davy, H., *Phil. Trans. R. Soc. Lond.* **1810,** *C*, 232-257.

63. Davy, H., *Elements of Chemical Philosophy* **1812,** *1* (1).

64. Reich, H. J.; Depp, W. A., Dynamic Characteristics of Glow Discharge Tubes. *Journal of Applied Physics* **1938,** *9* (6), 421-426.

65. Francis, V. J., *Fundamentals of discharge tube circuits* **1948**.

66. Hickmott, T. W., Low-frequency negative resistance in thin anodic oxide films. *J. Appl. Phys.* **1962,** *33*.

67. Hickmott, T. W., Low-Frequency Negative Resistance in Thin Anodic Oxide Films. *Journal of Applied Physics* **1962,** *33* (9), 2669-2682.

68. Gibbons, J. F.; Beadle, W. E., Switching properties of thin Nio films. *Solid-State Electronics* **1964,** *7* (11), 785-790.

69. Dearnaley, G.; Stoneham, A. M.; Morgan, D. V., Electrical phenomena in amorphous oxide films. *Rep Prog Phys* **1970,** *33* (3), 1129-1191.

70. Hickmott, T. W., Potential Distribution and Negative Resistance in Thin Oxide Films. *Journal of Applied Physics* **1964,** *35* (9), 2679-2689.

71. Hickmott, T. W., Impurity Conduction and Negative Resistance in Thin Oxide Films. *Journal of Applied Physics* **1964,** *35* (7), 2118-2122.

72. Simmons, J. G.; Verderber, R. R.; Mott, N. F., New conduction and reversible memory phenomena in thin insulating films. *Proceedings of the Royal Society of London. Series A. Mathematical and Physical Sciences* **1967,** *301* (1464), 77-102.

73. Dearnaley, G.; Morgan, D. V.; Stoneham, A. M., A model for filament growth and switching in amorphous oxide films. *J Non-Cryst Solids* **1970,** *4*, 593-612.

74. Oxley, D. In *Electroforming, Switching and Memory Effects in Oxide Thin Films*, 1977.

75. Hill, R. M., Single carrier transport in thin dielectric films. *Thin Solid Films* **1967,** *1* (1), 39-68.

76. Duke, C. B., *Tunneling in solids*. Academic Press: New York, 1969.

77. Kaplan, T.; Adler, D., Thermal Effects in Amorphous-Semiconductor Switching. *Applied Physics Letters* **1971,** *19* (10), 418-420.

78. Pagnia, H.; Sotnik, N., Bistable switching in electroformed metal–insulator–metal devices. *physica status solidi (a)* **1988,** *108* (1), 11-65.

79. Asamitsu, A.; Tomioka, Y.; Kuwahara, H.; Tokura, Y., Current switching of resistive states in magnetoresistive manganites. *Nature* **1997,** *388* (6637), 50-52.

80. Sawa, A., Resistive switching in transition metal oxides. *Mater Today* **2008,** *11* (6), 28-36.

81. Liu, S. Q.; Wu, N. J.; Ignatiev, A., Electric-pulse-induced reversible resistance change effect in magnetoresistive films. *Applied Physics Letters* **2000,** *76* (19), 2749-2751.

82. Beck, A.; Bednorz, J. G.; Gerber, C.; Rossel, C.; Widmer, D., Reproducible switching effect in thin oxide films for memory applications. *Applied Physics Letters* **2000,** *77* (1), 139-141.

83. Wu, Y.; Lee, B.; Wong, H. P., $\hbox{Al}_{2}\hbox{O}_{3}$-Based RRAM Using Atomic Layer Deposition (ALD) With 1-$\mu\hbox{A}$ RESET Current. *IEEE Electron Device Letters* **2010,** *31* (12), 1449-1451.

84. Wei, Z.; Kanzawa, Y.; Arita, K.; Katoh, Y.; Kawai, K.; Muraoka, S.; Mitani, S.; Fujii, S.; Katayama, K.; Iijima, M.; Mikawa, T.; Ninomiya, T.; Miyanaga, R.; Kawashima, Y.; Tsuji, K.; Himeno, A.; Okada, T.; Azuma, R.; Shimakawa, K.; Sugaya, H.; Takagi, T.; Yasuhara, R.; Horiba, K.; Kumigashira, H.; Oshima, M. In *Highly reliable TaOx ReRAM and direct evidence of redox reaction mechanism*, 2008 IEEE International Electron Devices Meeting, 15-17 Dec. 2008; 2008; pp 1-4.

85. Dongsoo, L.; Hyejung, C.; Hyunjun, S.; Dooho, C.; Hyunsang, H.; Myoung-Jae, L.; Sun-Ae, S.; Yoo, I. K., Resistance switching of the nonstoichiometric zirconium oxide for nonvolatile memory applications. *IEEE Electron Device Letters* **2005,** *26* (10), 719-721.

86. Wu, X.; Zhou, P.; Li, J.; Chen, L. Y.; Lv, H. B.; Lin, Y. Y.; Tang, T. A., Reproducible unipolar resistance switching in stoichiometric ZrO2 films. *Applied Physics Letters* **2007,** *90* (18), 183507.

87. Dong, R.; Lee, D. S.; Xiang, W. F.; Oh, S. J.; Seong, D. J.; Heo, S. H.; Choi, H. J.; Kwon, M. J.; Seo, S. N.; Pyun, M. B.; Hasan, M.; Hwang, H., Reproducible hysteresis and resistive switching in metal-CuxO-metal heterostructures. *Applied Physics Letters* **2007,** *90* (4), 042107.

88. Szot, K.; Speier, W.; Bihlmayer, G.; Waser, R., Switching the electrical resistance of individual dislocations in single-crystalline SrTiO3. *Nature Materials* **2006,** *5* (4), 312-320.

89. Sakamoto, T.; Sunamura, H.; Kawaura, H.; Hasegawa, T.; Nakayama, T.; Aono, M., Nanometer-scale switches using copper sulfide. *Applied Physics Letters* **2003,** *82* (18), 3032-3034.

90. Terabe, K.; Hasegawa, T.; Nakayama, T.; Aono, M., Quantized conductance atomic switch. *Nature* **2005,** *433* (7021), 47-50.

91. Ma, L. P.; Liu, J.; Yang, Y., Organic electrical bistable devices and rewritable memory cells. *Applied Physics Letters* **2002,** *80* (16), 2997-2999.

92. Kano, M.; Orito, S.; Tsuruoka, Y.; Ueno, N., Nonvolatile memory effect of an Al/2-Amino-4,5-dicyanoimidazole/Al structure. *Synthetic Met* **2005,** *153* (1), 265-268.

93. Terai, M.; Fujita, K.; Tsutsui, T., Electrical Bistability of Organic Thin-Film Device Using Ag Electrode. *Jpn J Appl Phys* **2006,** *45* (4B), 3754-3757.

94. Mahapatro, A. K.; Agrawal, R.; Ghosh, S., Electric-field-induced conductance transition in 8-hydroxyquinoline aluminum (Alq3). *Journal of Applied Physics* **2004,** *96* (6), 3583-3585.

95. Verbakel, F.; Meskers, S. C. J.; Janssen, R. A. J., Electronic Memory Effects in a Sexithiophene−Poly(ethylene oxide) Block Copolymer Doped with NaCl. Combined Diode and Resistive Switching Behavior. *Chem Mater* **2006,** *18* (11), 2707-2712.

96. Strukov, D. B.; Snider, G. S.; Stewart, D. R.; Williams, R. S., The missing memristor found. *Nature* **2008,** *453* (7191), 80-83.

97. Chua, L., Memristor-The missing circuit element. *IEEE Transactions on Circuit Theory* **1971,** *18* (5), 507-519.

98. Strachan, J. P., Direct identification of the conducting channels in a functioning memristive device. *Adv. Mater.* **2010,** *22*.

99. Palma, G.; Vianello, E.; Molas, G.; Cagli, C.; Longnos, F.; Guy, J.; Reyboz, M.; Carabasse, C.; Bernard, M.; Dahmani, F.; Bretegnier, D.; Liebault, J.; Salvo, B. D., Effect of the Active Layer Thickness and Temperature on the Switching Kinetics of GeS2-Based Conductive Bridge Memories. *Jpn J Appl Phys* **2013,** *52* (4S), 04CD02.

100. Jameson, J. R.; Gilbert, N.; Koushan, F.; Saenz, J.; Wang, J.; Hollmer, S.; Kozicki, M. N., One-dimensional model of the programming kinetics of conductive-bridge memory cells. *Applied Physics Letters* **2011,** *99* (6), 063506.

101. Wang, Q.; Sun, H. J.; Zhang, J. J.; Xu, X. H.; Miao, X. S., Electrode Materials for Ge2Sb2Te5-Based Memristors. *J Electron Mater* **2012,** *41* (12), 3417-3422.

102. Tappertzhofen, S.; Valov, I.; Waser, R., Quantum conductance and switching kinetics of AgI-based microcrossbar cells. *Nanotechnology* **2012,** *23* (14), 145703.

103. Menzel, S.; Tappertzhofen, S.; Waser, R.; Valov, I., Switching kinetics of electrochemical metallization memory cells. *Physical Chemistry Chemical Physics* **2013,** *15* (18), 6945-6952.

104. Yu, S.; Guan, X.; Wong, H.-S. P., Conduction mechanism of TiN/HfOx/Pt resistive switching memory: A trap-assisted-tunneling model. *Applied Physics Letters* **2011,** *99* (6), 063507.

105. Kumar, S., Conduction channel formation and dissolution due to oxygen thermophoresis/diffusion in hafnium oxide memristors. *ACS Nano* **2016,** *10*.

106. Kumar, S., Direct observation of localized radial oxygen migration in functioning tantalum oxide memristors. *Adv. Mater.* **2016,** *28*.

107. Baeumer, C., Quantifying redox-induced Schottky barrier variations in memristive devices via in operando spectromicroscopy with graphene electrodes. *Nat. Commun.* **2016,** *7*.

108. Waser, R.; Aono, M., Nanoionics-based resistive switching memories. *Nat. Mater.* **2007,** *6*.

109. Waser, R.; Dittmann, R.; Staikov, G.; Szot, K., Redox-based resistive switching memories - nanoionic mechanisms, prospects, and challenges. *Adv. Mater.* **2009,** *21*.

110. Gallo, M.; Krebs, D.; Zipoli, F.; Salinga, M.; Sebastian, A., Collective structural relaxation in phase-change memory devices. *Adv. Electron. Mater.* **2018,** *4*.

111. Sebastian, A.; Gallo, M.; Krebs, D., Crystal growth within a phase change memory cell. *Nat. Commun.* **2014,** *5*.

112. Raoux, S., Phase change materials and their application to random access memory technology. *Microelectron. Eng.* **2008,** *85*.

113. Wong, H. S. P., Phase change memory. *Proc. IEEE* **2010,** *98*.

114. Burr, G. W., Phase change memory technology. *J. Vac. Sci. Technol. B* **2010,** *28*.

115. Burr, G. W., Recent progress in phase-change memory technology. *IEEE J. Emerg. Sel. Top. Circuits Syst.* **2016,** *6*.

116. Chappert, C.; Fert, A.; Dau, F. N., The emergence of spin electronics in data storage. *Nat. Mater.* **2007,** *6*.

117. Baibich, M. N., Giant magnetoresistance of (001) Fe/(001) Cr magnetic superlattices. *Phys. Rev. Lett.* **1988,** *61*.

118. Moodera, J. S.; Kinder, L. R.; Wong, T. M.; Meservey, R., Large magnetoresistance at room temperature in ferromagnetic thin film tunnel junctions. *Phys. Rev. Lett.* **1995,** *74*.

119. Parkin, S. S. P., Giant tunnelling magnetoresistance at room temperature with MgO (100) tunnel barriers. *Nat. Mater.* **2004,** *3*.

120. Yuasa, S.; Nagahama, T.; Fukushima, A.; Suzuki, Y.; Ando, K., Giant room-temperature magnetoresistance in single-crystal Fe/MgO/Fe magnetic tunnel junctions. *Nat. Mater.* **2004,** *3*.

121. Zhang, X. G.; Butler, W. H., Large magnetoresistance in bcc Co/MgO/Co and FeCo/MgO/FeCo tunnel junctions. *Phys. Rev. B* **2004,** *70*.

122. Berger, L., Emission of spin waves by a magnetic multilayer traversed by a current. *Phys. Rev. B* **1996,** *54*.

123. Slonczewski, J. C., Current-driven excitation of magnetic multilayers. *J. Magn. Magn. Mater.* **1996,** *159*.

124. Duan, C. G., Surface magnetoelectric effect in ferromagnetic metal films. *Phys. Rev. Lett.* **2008,** *101*.

125. Mihai Miron, I., Current-driven spin torque induced by the Rashba effect in a ferromagnetic metal layer. *Nat. Mater.* **2010,** *9*.

126. Liu, L., Spin-torque switching with the giant spin Hall effect of tantalum. *Science* **2012,** *336*.

127. Seidel, J., Conduction at domain walls in oxide multiferroics. *Nat. Mater.* **2009,** *8*.

128. Boyn, S., Learning through ferroelectric domain dynamics in solid-state synapses. *Nat. Commun.* **2017,** *8*.

129. Rojac, T., Domain-wall conduction in ferroelectric BiFeO3 controlled by accumulation of charged defects. *Nat. Mater.* **2017,** *16*.

130. Li, C.; Hu, M.; Li, Y. N.; Jiang, H.; Ge, N.; Montgomery, E.; Zhang, J. M.; Song, W. H.; Davila, N.; Graves, C. E.; Li, Z. Y.; Strachan, J. P.; Lin, P.; Wang, Z. R.; Barnell, M.; Wu, Q.; Williams, R. S.; Yang, J. J.; Xia, Q. F., Analogue signal and image processing with large memristor crossbars. *Nature Electronics* **2018,** *1* (1), 52-59.

131. Yang, J. J., Memristive switching mechanism for metal/oxide/metal nanodevices. *Nature Nanotech.* **2008,** *3*.

132. Chang, S. H., Effects of heat dissipation on unipolar resistance switching in Pt/NiO/Pt capacitors. *Appl. Phys. Lett.* **2008,** *92*.

133. Yang, J. J.; Strukov, D. B.; Stewart, D. R., Memristive devices for computing. *Nature Nanotechnology* **2012,** *8*, 13.

134. Kwon, D. H., Atomic structure of conducting nanofilaments in TiO2 resistive switching memory. *Nat. Nanotechnol.* **2010,** *5*.

135. Miao, F., Anatomy of a nanoscale conduction channel reveals the mechanism of a high-performance memristor. *Adv. Mater.* **2011,** *23*.

136. Kwon, D. H., Atomic structure of conducting nanofilaments in TiO2 resistive switching memory. *Nature Nanotech.* **2010,** *5*.

137. Pickett, M. D.; Borghetti, J.; Yang, J. J.; Medeiros-Ribeiro, G.; Williams, R. S., Coexistence of memristance and negative differential resistance in a nanoscale metal-oxide-metal system. *Adv. Mater.* **2011,** *23*.

138. Wong, H. S. P., Metal-oxide RRAM. *Proc. IEEE* **2012,** *100*.

139. Yang, Y.; Gao, P.; Gaba, S.; Chang, T.; Pan, X.; Lu, W., Observation of conducting filament growth in nanoscale resistive memories. *Nature Communications* **2012,** *3*, 732.

140. Yang, Y.; Gao, P.; Li, L.; Pan, X.; Tappertzhofen, S.; Choi, S.; Waser, R.; Valov, I.; Lu, W. D., Electrochemical dynamics of nanoscale metallic inclusions in dielectrics. *Nature Communications* **2014,** *5*, 4232.

141. Valov, I.; Kozicki, M. N., Cation-based resistance change memory. *J. Phys. D Appl. Phys.* **2013,** *46*.

142. Choi, S. J., In situ observation of voltage-induced multilevel resistive switching in solid electrolyte memory. *Adv. Mater.* **2011,** *23*.

143. Yang, Y., Observation of conducting filament growth in nanoscale resistive memories. *Nat. Commun.* **2012,** *3*.

144. Guo, X.; Schindler, C.; Menzel, S.; Waser, R., Understanding the switching-off mechanism in Ag+ migration based resistively switching model systems. *Applied Physics Letters* **2007,** *91* (13), 133513.

145. Wang, W.; Wang, M.; Ambrosi, E.; Bricalli, A.; Laudato, M.; Sun, Z.; Chen, X.; Ielmini, D., Surface diffusion-limited lifetime of silver and copper nanofilaments in resistive switching devices. *Nature Communications* **2019,** *10* (1), 81.

146. Manning, H. G.; Biswas, S.; Holmes, J. D.; Boland, J. J., Nonpolar Resistive Switching in Ag@TiO2 Core-Shell Nanowires. *ACS Appl Mater Interfaces* **2017,** *9* (44), 38959-38966.

147. Sun, H.; Liu, Q.; Li, C.; Long, S.; Lv, H.; Bi, C.; Huo, Z.; Li, L.; Liu, M., Direct Observation of Conversion Between Threshold Switching and Memory Switching Induced by Conductive Filament Morphology. *Adv Funct Mater* **2014,** *24* (36), 5679-5686.

148. Yuan, F.; Zhang, Z.; Liu, C.; Zhou, F.; Yau, H. M.; Lu, W.; Qiu, X.; Wong, H. S. P.; Dai, J.; Chai, Y., Real-Time Observation of the Electrode-Size-Dependent Evolution Dynamics of the Conducting Filaments in a SiO2 Layer. *ACS Nano* **2017,** *11* (4), 4097-4104.

149. Chua, L. O.; Sung Mo, K., Memristive devices and systems. *P Ieee* **1976,** *64* (2), 209-223.

150. Scott, J. C.; Bozano, L. D., Nonvolatile Memory Elements Based on Organic Materials. *Advanced Materials* **2007,** *19* (11), 1452-1463.

151. Nedaaee Oskoee, E.; Sahimi, M., Electric currents in networks of interconnected memristors. *Phys Rev E* **2011,** *83* (3), 031105.

152. Sillin, H. O.; Aguilera, R.; Shieh, H.-H.; Avizienis, A. V.; Aono, M.; Stieg, A. Z.; Gimzewski, J. K., A theoretical and experimental study of neuromorphic atomic switch networks for reservoir computing. *Nanotechnology* **2013,** *24* (38), 384004.

153. Waser, R.; Aono, M., Nanoionics-based resistive switching memories. *Nature Materials* **2007,** *6* (11), 833-840.

154. Williams, R. S., A short history of memristor development. **2014**.

155. Pickett, M. D.; Strukov, D. B.; Borghetti, J. L.; Yang, J. J.; Snider, G. S.; Stewart, D. R.; Williams, R. S., Switching dynamics in titanium dioxide memristive devices. *Journal of Applied Physics* **2009,** *106* (7), 074508.

156. Strukov, D. B.; Borghetti, J. L.; Williams, R. S., Coupled Ionic and Electronic Transport Model of Thin-Film Semiconductor Memristive Behavior. *Small* **2009,** *5* (9), 1058-1063.

157. Yu, S.; Wong, H. P., Compact Modeling of Conducting-Bridge Random-Access Memory (CBRAM). *Ieee T Electron Dev* **2011,** *58* (5), 1352-1360.

158. Wood, I. K., Neuroscience: Exploring the brain. *Journal of Child and Family Studies* **1996,** *5* (3), 377-379.

159. Bi, G.-q.; Poo, M.-m., Synaptic Modifications in Cultured Hippocampal Neurons: Dependence on Spike Timing, Synaptic Strength, and Postsynaptic Cell Type. *The Journal of Neuroscience* **1998,** *18* (24), 10464-10472.

160. Legenstein, R.; Naeger, C.; Maass, W., What Can a Neuron Learn with Spike-Timing-Dependent Plasticity? *Neural Comput* **2005,** *17* (11), 2337-2382.

161. Gerstner, W.; Kistler, W., *Spiking Neuron Models: An Introduction*. Cambridge University Press: 2002; p 400.

162. McCulloch, W. S.; Pitts, W., A logical calculus of the ideas immanent in nervous activity. *The bulletin of mathematical biophysics* **1943,** *5* (4), 115-133.

163. Silver, D.; Huang, A.; Maddison, C. J.; Guez, A.; Sifre, L.; van den Driessche, G.; Schrittwieser, J.; Antonoglou, I.; Panneershelvam, V.; Lanctot, M.; Dieleman, S.; Grewe, D.; Nham, J.; Kalchbrenner, N.; Sutskever, I.; Lillicrap, T.; Leach, M.; Kavukcuoglu, K.; Graepel, T.; Hassabis, D., Mastering the game of Go with deep neural networks and tree search. *Nature* **2016,** *529* (7587), 484-489.

164. Silver, D.; Schrittwieser, J.; Simonyan, K.; Antonoglou, I.; Huang, A.; Guez, A.; Hubert, T.; Baker, L.; Lai, M.; Bolton, A.; Chen, Y.; Lillicrap, T.; Hui, F.; Sifre, L.; van den Driessche, G.; Graepel, T.; Hassabis, D., Mastering the game of Go without human knowledge. *Nature* **2017,** *550* (7676), 354-359.

165. Merolla, P. A.; Arthur, J. V.; Alvarez-Icaza, R.; Cassidy, A. S.; Sawada, J.; Akopyan, F.; Jackson, B. L.; Imam, N.; Guo, C.; Nakamura, Y.; Brezzo, B.; Vo, I.; Esser, S. K.; Appuswamy, R.; Taba, B.; Amir, A.; Flickner, M. D.; Risk, W. P.; Manohar, R.; Modha, D. S., A million spiking-neuron integrated circuit with a scalable communication network and interface. *Science* **2014,** *345* (6197), 668-673.

166. Davies, M.; Srinivasa, N.; Lin, T.; Chinya, G.; Cao, Y.; Choday, S. H.; Dimou, G.; Joshi, P.; Imam, N.; Jain, S.; Liao, Y.; Lin, C.; Lines, A.; Liu, R.; Mathaikutty, D.; McCoy, S.; Paul, A.; Tse, J.; Venkataramanan, G.; Weng, Y.; Wild, A.; Yang, Y.; Wang, H., Loihi: A Neuromorphic Manycore Processor with On-Chip Learning. *IEEE Micro* **2018,** *38* (1), 82-99.

167. Pei, J.; Deng, L.; Song, S.; Zhao, M.; Zhang, Y.; Wu, S.; Wang, G.; Zou, Z.; Wu, Z.; He, W.; Chen, F.; Deng, N.; Wu, S.; Wang, Y.; Wu, Y.; Yang, Z.; Ma, C.; Li, G.; Han, W.; Li, H.; Wu, H.; Zhao, R.; Xie, Y.; Shi, L., Towards artificial general intelligence with hybrid Tianjic chip architecture. *Nature* **2019,** *572* (7767), 106-111.

168. Roy, K.; Jaiswal, A.; Panda, P., Towards spike-based machine intelligence with neuromorphic computing. *Nature* **2019,** *575* (7784), 607-617.

169. Prezioso, M.; Merrikh-Bayat, F.; Hoskins, B. D.; Adam, G. C.; Likharev, K. K.; Strukov, D. B., Training and operation of an integrated neuromorphic network based on metal-oxide memristors. *Nature* **2015,** *521* (7550), 61-64.

170. Du, C.; Cai, F.; Zidan, M. A.; Ma, W.; Lee, S. H.; Lu, W. D., Reservoir computing using dynamic memristors for temporal information processing. *Nature Communications* **2017,** *8* (1), 2204.

171. Avizienis, A. V.; Sillin, H. O.; Martin-Olmos, C.; Shieh, H. H.; Aono, M.; Stieg, A. Z.; Gimzewski, J. K., Neuromorphic Atomic Switch Networks. *Plos One* **2012,** *7* (8), e42772.

172. Bellew, A. T.; Bell, A. P.; McCarthy, E. K.; Fairfield, J. A.; Boland, J. J., Programmability of nanowire networks. *Nanoscale* **2014,** *6* (16), 9632-9639.

173. Bellew, A. T.; Manning, H. G.; da Rocha, C. G.; Ferreira, M. S.; Boland, J. J., Resistance of Single Ag Nanowire Junctions and Their Role in the Conductivity of Nanowire Networks. *Acs Nano* **2015,** *9* (11), 11422-11429.

174. Du, H.; Wan, T.; Qu, B.; Cao, F.; Lin, Q.; Chen, N.; Lin, X.; Chu, D., Engineering Silver Nanowire Networks: From Transparent Electrodes to Resistive Switching Devices. *ACS Appl Mater Interfaces* **2017,** *9* (24), 20762-20770.

175. Cagli, C.; Nardi, F.; Harteneck, B.; Tan, Z. K.; Zhang, Y. G.; Ielmini, D., Resistive-Switching Crossbar Memory Based on Ni-NiO Core-Shell Nanowires. *Small* **2011,** *7* (20), 2899-2905.

176. Liang, K.-D.; Huang, C.-H.; Lai, C.-C.; Huang, J.-S.; Tsai, H.-W.; Wang, Y.-C.; Shih, Y.-C.; Chang, M.-T.; Lo, S.-C.; Chueh, Y.-L., Single CuOx Nanowire Memristor: Forming-Free Resistive Switching Behavior. *ACS Applied Materials & Interfaces* **2014,** *6* (19), 16537-16544.

177. De, S.; Higgins, T. M.; Lyons, P. E.; Doherty, E. M.; Nirmalraj, P. N.; Blau, W. J.; Boland, J. J.; Coleman, J. N., Silver Nanowire Networks as Flexible, Transparent, Conducting Films: Extremely High DC to Optical Conductivity Ratios. *Acs Nano* **2009,** *3* (7), 1767-1774.

178. Barabási, A.-L.; Albert, R., Emergence of Scaling in Random Networks. *Science* **1999,** *286* (5439), 509-512.

179. Loeffler, A.; Zhu, R.; Hochstetter, J.; Li, M.; Fu, K.; Diaz-Alvarez, A.; Nakayama, T.; Shine, J. M.; Kuncic, Z., Topological Properties of Neuromorphic Nanowire Networks. *Frontiers in Neuroscience* **2020,** *14* (184).

180. Stieg, A. Z.; Avizienis, A. V.; Sillin, H. O.; Martin-Olmos, C.; Aono, M.; Gimzewski, J. K., Emergent Criticality in Complex Turing B-Type Atomic Switch Networks. *Advanced Materials* **2012,** *24* (2), 286-293.

181. Manning, H. G.; Niosi, F.; da Rocha, C. G.; Bellew, A. T.; O'Callaghan, C.; Biswas, S.; Flowers, P. F.; Wiley, B. J.; Holmes, J. D.; Ferreira, M. S.; Boland, J. J., Emergence of winner-takes-all connectivity paths in random nanowire networks. *Nature Communications* **2018,** *9* (1), 3219.

182. Diaz-Alvarez, A.; Higuchi, R.; Sanz-Leon, P.; Marcus, I.; Shingaya, Y.; Stieg, A. Z.; Gimzewski, J. K.; Kuncic, Z.; Nakayama, T., Emergent dynamics of neuromorphic nanowire networks. *Scientific Reports* **2019,** *9* (1), 14920.

183. Nirmalraj, P. N.; Bellew, A. T.; Bell, A. P.; Fairfield, J. A.; McCarthy, E. K.; O'Kelly, C.; Pereira, L. F. C.; Sorel, S.; Morosan, D.; Coleman, J. N.; Ferreira, M. S.; Boland, J. J., Manipulating Connectivity and Electrical Conductivity in Metallic Nanowire Networks. *Nano Letters* **2012,** *12* (11), 5966-5971.

184. Diaz-Alvarez, A.; Higuchi, R.; Li, Q.; Shingaya, Y.; Nakayama, T., Associative routing through neuromorphic nanowire networks. *Aip Adv* **2020,** *10* (2), 025134.

185. Yan, Z.; Lin, J.; Peng, Z. W.; Sun, Z. Z.; Zhu, Y.; Li, L.; Xiang, C. S.; Samuel, E. L.; Kittrell, C.; Tour, J. M., Toward the Synthesis of Wafer-Scale Single-Crystal Graphene on Copper Foils. *Acs Nano* **2012,** *6* (10), 9110-9117.

186. Li, X. S.; Zhu, Y. W.; Cai, W. W.; Borysiak, M.; Han, B. Y.; Chen, D.; Piner, R. D.; Colombo, L.; Ruoff, R. S., Transfer of Large-Area Graphene Films for High-Performance Transparent Conductive Electrodes. *Nano Letters* **2009,** *9* (12), 4359-4363.

187. Wang, S. H.; Zhang, X.; Zhao, W. W., Flexible, Transparent, and Conductive Film Based on Random Networks of Ag Nanowires. *J Nanomater* **2013**.

188. Cheng, B.; Le, Y.; Yu, J. G., Preparation and enhanced photocatalytic activity of Ag@TiO2 core-shell nanocomposite nanowires. *J Hazard Mater* **2010,** *177* (1-3), 971-977.

189. Chin, S. F.; Pang, S. C.; Dom, F. E. I., Sol-gel synthesis of silver/titanium dioxide (Ag/TiO2) core-shell nanowires for photocatalytic applications. *Materials Letters* **2011,** *65* (17), 2673-2675.

190. Sun, M.; Fu, W.; Yang, H.; Sui, Y.; Zhao, B.; Yin, G.; Li, Q.; Zhao, H.; Zou, G., One-step synthesis of coaxial Ag/TiO2 nanowire arrays on transparent conducting substrates: Enhanced electron collection in dye-sensitized solar cells. *Electrochemistry Communications* **2011,** *13* (12), 1324-1327.

191. Smith, E.; Dent, G., *Modern Raman Spectroscopy: A Practical Approach*. Wiley: 2019.

192. Breitenstein, O.; Warta, W.; Langenkamp, M., Physical and Technical Basics. In *Lock-in Thermography: Basics and Use for Evaluating Electronic Devices and Materials*, Springer Berlin Heidelberg: Berlin, Heidelberg, 2010; pp 7-59.

193. Monnier, C. A.; Lattuada, M.; Burnand, D.; Crippa, F.; Martinez-Garcia, J. C.; Hirt, A. M.; Rothen-Rutishauser, B.; Bonmarin, M.; Petri-Fink, A., A lock-in-based method to examine the thermal signatures of magnetic nanoparticles in the liquid, solid and aggregated states. *Nanoscale* **2016,** *8* (27), 13321-13332.

194. Lemal, P.; Geers, C.; Monnier, C. A.; Crippa, F.; Daum, L.; Urban, D. A.; Rothen-Rutishauser, B.; Bonmarin, M.; Petri-Fink, A.; Moore, T. L., Lock-in thermography as a rapid and reproducible thermal characterization method for magnetic nanoparticles. *Journal of Magnetism and Magnetic Materials* **2017,** *427*, 206-211.

195. Nakajima, H.; Morimoto, T.; Okigawa, Y.; Yamada, T.; Ikuta, Y.; Kawahara, K.; Ago, H.; Okazaki, T., Imaging of local structures affecting electrical transport properties of large graphene sheets by lock-in thermography. *Science Advances* **2019,** *5* (2), eaau3407.

196. Mohiuddin, T. M. G.; Lombardo, A.; Nair, R. R.; Bonetti, A.; Savini, G.; Jalil, R.; Bonini, N.; Basko, D. M.; Galiotis, C.; Marzari, N.; Novoselov, K. S.; Geim, A. K.; Ferrari, A. C., Uniaxial strain in graphene by Raman spectroscopy: G peak splitting, Gr\"uneisen parameters, and sample orientation. *Phys Rev B* **2009,** *79* (20), 205433.

197. Metzger, C.; Rémi, S.; Liu, M.; Kusminskiy, S. V.; Castro Neto, A. H.; Swan, A. K.; Goldberg, B. B., Biaxial Strain in Graphene Adhered to Shallow Depressions. *Nano Letters* **2010,** *10* (1), 6-10.

198. Yoon, D.; Son, Y.-W.; Cheong, H., Strain-Dependent Splitting of the Double-Resonance Raman Scattering Band in Graphene. *Phys Rev Lett* **2011,** *106* (15), 155502.

199. Das, A.; Pisana, S.; Chakraborty, B.; Piscanec, S.; Saha, S. K.; Waghmare, U. V.; Novoselov, K. S.; Krishnamurthy, H. R.; Geim, A. K.; Ferrari, A. C.; Sood, A. K., Monitoring dopants by Raman scattering in an electrochemically top-gated graphene transistor. *Nature Nanotechnology* **2008,** *3*, 210.

200. Ferrari, A. C.; Meyer, J. C.; Scardaci, V.; Casiraghi, C.; Lazzeri, M.; Mauri, F.; Piscanec, S.; Jiang, D.; Novoselov, K. S.; Roth, S.; Geim, A. K., Raman Spectrum of Graphene and Graphene Layers. *Phys Rev Lett* **2006,** *97* (18), 187401.

201. Yoon, D.; Son, Y. W.; Cheong, H., Negative thermal expansion coefficient of graphene measured by Raman spectroscopy. *Nano Lett* **2011,** *11* (8), 3227-31.

202. Lee, J. E.; Ahn, G.; Shim, J.; Lee, Y. S.; Ryu, S., Optical separation of mechanical strain from charge doping in graphene. *Nature Communications* **2012,** *3*, 1024.

203. Huang, Y.; Wang, X.; Zhang, X.; Chen, X.; Li, B.; Wang, B.; Huang, M.; Zhu, C.; Zhang, X.; Bacsa, W. S.; Ding, F.; Ruoff, R. S., Raman Spectral Band Oscillations in Large Graphene Bubbles. *Phys Rev Lett* **2018,** *120* (18), 186104.

204. Bunch, J. S.; Verbridge, S. S.; Alden, J. S.; van der Zande, A. M.; Parpia, J. M.; Craighead, H. G.; McEuen, P. L., Impermeable Atomic Membranes from Graphene Sheets. *Nano Letters* **2008,** *8* (8), 2458-2462.

205. Metten, D.; Federspiel, F.; Romeo, M.; Berciaud, S., All-Optical Blister Test of Suspended Graphene Using Micro-Raman Spectroscopy. *Phys Rev Appl* **2014,** *2* (5), 054008.

206. Rasch, B.; Born, J., About sleep's role in memory. *Physiol Rev* **2013,** *93* (2), 681-766.

207. Staresina, B. P.; Bergmann, T. O.; Bonnefond, M.; van der Meij, R.; Jensen, O.; Deuker, L.; Elger, C. E.; Axmacher, N.; Fell, J., Hierarchical nesting of slow oscillations, spindles and ripples in the human hippocampus during sleep. *Nat Neurosci* **2015,** *18* (11), 1679-1686.

208. O'Neill, J.; Pleydell-Bouverie, B.; Dupret, D.; Csicsvari, J., Play it again: reactivation of waking experience and memory. *Trends in Neurosciences* **2010,** *33* (5), 220-229.

209. Breton, J.; Robertson, Edwin M., Memory Processing: The Critical Role of Neuronal Replay during Sleep. *Current Biology* **2013,** *23* (18), R836-R838.

210. Cross, Z. R.; Kohler, M. J.; Schlesewsky, M.; Gaskell, M. G.; Bornkessel-Schlesewsky, I., Sleep-Dependent Memory Consolidation and Incremental Sentence Comprehension: Computational Dependencies during Language Learning as Revealed by Neuronal Oscillations. *Frontiers in Human Neuroscience* **2018,** *12* (18).

211. Stickgold, R.; James, L.; Hobson, J. A., Visual discrimination learning requires sleep after training. *Nat Neurosci* **2000,** *3* (12), 1237-1238.

212. Stickgold, R.; Whidbee, D.; Schirmer, B.; Patel, V.; Hobson, J. A., Visual Discrimination Task Improvement: A Multi-Step Process Occurring During Sleep. *Journal of Cognitive Neuroscience* **2000,** *12* (2), 246-254.

213. Fischer, S.; Hallschmid, M.; Elsner, A. L.; Born, J., Sleep forms memory for finger skills. *Proceedings of the National Academy of Sciences* **2002,** *99* (18), 11987-11991.

214. RAUCHS, G.; DESGRANGES, B.; FORET, J.; EUSTACHE, F., The relationships between memory systems and sleep stages. *Journal of Sleep Research* **2005,** *14* (2), 123-140.

215. Stickgold, R., Sleep-dependent memory consolidation. *Nature* **2005,** *437* (7063), 1272-1278.

216. Sawangjit, A.; Oyanedel, C. N.; Niethard, N.; Salazar, C.; Born, J.; Inostroza, M., The hippocampus is crucial for forming non-hippocampal long-term memory during sleep. *Nature* **2018,** *564* (7734), 109-113.

217. Diekelmann, S.; Born, J., The memory function of sleep. *Nature Reviews Neuroscience* **2010,** *11* (2), 114-126.

218. Tronson, N. C.; Taylor, J. R., Molecular mechanisms of memory reconsolidation. *Nature Reviews Neuroscience* **2007,** *8* (4), 262-275.

219. Born, J.; Wilhelm, I., System consolidation of memory during sleep. *Psychological Research* **2012,** *76* (2), 192-203.

220. Liu, L.; Xiong, W.; Liu, Y.; Chen, K.; Xu, Z.; Zhou, Y.; Han, J.; Ye, C.; Chen, X.; Song, Z.; Zhu, M., Designing High-Performance Storage in $HfO_2/BiFeO_3$ Memristor for Artificial Synapse Applications. *Adv Electron Mater* **2020,** *6* (2), 1901012.

221. Yan, X. B.; Zhao, J. H.; Liu, S.; Zhou, Z. Y.; Liu, Q.; Chen, J. S.; Liu, X. Y., Memristor with Ag-Cluster-Doped TiO_2 Films as Artificial Synapse for Neuroinspired Computing. *Adv Funct Mater* **2018,** *28* (1).

222. Wang, Z.; Joshi, S.; Savel'ev, S. E.; Jiang, H.; Midya, R.; Lin, P.; Hu, M.; Ge, N.; Strachan, J. P.; Li, Z.; Wu, Q.; Barnell, M.; Li, G.-L.; Xin, H. L.; Williams, R. S.; Xia, Q.; Yang, J. J., Memristors with diffusive dynamics as synaptic emulators for neuromorphic computing. *Nature Materials* **2017,** *16* (1), 101-108.

223. Li, Y.; Fang, P.; Fan, X.; Pei, Y., NiO-based memristor with three resistive switching modes. *Semicond Sci Tech* **2020,** *35* (5), 055004.

224. Milano, G.; Pedretti, G.; Fretto, M.; Boarino, L.; Benfenati, F.; Ielmini, D.; Valov, I.; Ricciardi, C., Brain-Inspired Structural Plasticity through Reweighting and Rewiring in Multi-Terminal Self-Organizing Memristive Nanowire Networks. *Advanced Intelligent Systems n/a* (n/a), 2000096.

225. Fu, T.; Liu, X.; Gao, H.; Ward, J. E.; Liu, X.; Yin, B.; Wang, Z.; Zhuo, Y.; Walker, D. J. F.; Joshua Yang, J.; Chen, J.; Lovley, D. R.; Yao, J., Bioinspired bio-voltage memristors. *Nature Communications* **2020,** *11* (1), 1861.

226. Shukla, N.; Ghosh, R. K.; Grisafe, B.; Datta, S. In *Fundamental mechanism behind volatile and non-volatile switching in metallic conducting bridge RAM*, 2017 IEEE International Electron Devices Meeting (IEDM), 2-6 Dec. 2017; 2017; pp 4.3.1-4.3.4.

227. Rogerson, T.; Cai, D. J.; Frank, A.; Sano, Y.; Shobe, J.; Lopez-Aranda, M. F.; Silva, A. J., Synaptic tagging during memory allocation. *Nature Reviews Neuroscience* **2014,** *15* (3), 157-169.

228. Wang, J. X.; Rogers, L. M.; Gross, E. Z.; Ryals, A. J.; Dokucu, M. E.; Brandstatt, K. L.; Hermiller, M. S.; Voss, J. L., Targeted enhancement of cortical-hippocampal brain networks and associative memory. *Science* **2014,** *345* (6200), 1054-1057.

229. Grewe, B. F.; Gründemann, J.; Kitch, L. J.; Lecoq, J. A.; Parker, J. G.; Marshall, J. D.; Larkin, M. C.; Jercog, P. E.; Grenier, F.; Li, J. Z.; Lüthi, A.; Schnitzer, M. J., Neural ensemble dynamics underlying a long-term associative memory. *Nature* **2017,** *543* (7647), 670-675.

230. Josselyn, S. A.; Tonegawa, S., Memory engrams: Recalling the past and imagining the future. *Science* **2020,** *367* (6473), eaaw4325.

231. Moyer Jr., J. R.; Thompson, L. T.; Disterhoft, J. F., Trace Eyeblink Conditioning Increases CA1 Excitability in a Transient and Learning-Specific Manner. *The Journal of Neuroscience* **1996,** *16* (17), 5536-5546.

232. McKay, B. M.; Matthews, E. A.; Oliveira, F. A.; Disterhoft, J. F., Intrinsic Neuronal Excitability Is Reversibly Altered by a Single Experience in Fear Conditioning. *J Neurophysiol* **2009,** *102* (5), 2763-2770.

233. Cai, D. J.; Aharoni, D.; Shuman, T.; Shobe, J.; Biane, J.; Song, W.; Wei, B.; Veshkini, M.; La-Vu, M.; Lou, J.; Flores, S. E.; Kim, I.; Sano, Y.; Zhou, M.; Baumgaertel, K.; Lavi, A.; Kamata, M.; Tuszynski, M.; Mayford, M.; Golshani, P.; Silva, A. J., A shared neural ensemble links distinct contextual memories encoded close in time. *Nature* **2016,** *534* (7605), 115-118.

234. Yokose, J.; Okubo-Suzuki, R.; Nomoto, M.; Ohkawa, N.; Nishizono, H.; Suzuki, A.; Matsuo, M.; Tsujimura, S.; Takahashi, Y.; Nagase, M.; Watabe, A. M.; Sasahara, M.; Kato, F.; Inokuchi, K., Overlapping memory trace indispensable for linking, but not recalling, individual memories. *Science* **2017,** *355* (6323), 398-403.

235. Spinelli, D.; Jensen, F., Plasticity: the mirror of experience. *Science* **1979,** *203* (4375), 75-78.

236. Bear, M. F.; Connors, B. W.; Paradiso, M. A., *Neuroscience: Exploring the Brain*. Wolters Kluwer: 2016.

237. Li, Y.; Xu, L.; Zhong, Y.-P.; Zhou, Y.-X.; Zhong, S.-J.; Hu, Y.-Z.; Chua, L. O.; Miao, X.-S., Associative Learning with Temporal Contiguity in a Memristive Circuit for Large-Scale Neuromorphic Networks. *Adv Electron Mater* **2015,** *1* (8), 1500125.

238. Pershin, Y.; Di Ventra, M., Experimental demonstration of associative memory with memristive neural networks. *Nature Precedings* **2009**.

239. Bichler, O.; Zhao, W.; Alibart, F.; Pleutin, S.; Lenfant, S.; Vuillaume, D.; Gamrat, C., Pavlov's Dog Associative Learning Demonstrated on Synaptic-Like Organic Transistors. *Neural Comput* **2013,** *25* (2), 549-566.

240. Ziegler, M.; Soni, R.; Patelczyk, T.; Ignatov, M.; Bartsch, T.; Meuffels, P.; Kohlstedt, H., An Electronic Version of Pavlov's Dog. *Adv Funct Mater* **2012,** *22* (13), 2744-2749.

241. Maier, P.; Hartmann, F.; Emmerling, M.; Schneider, C.; Kamp, M.; Worschech, L.; Höfling, S., Associative learning with Y-shaped floating gate transistors operated in memristive modes. *Applied Physics Letters* **2017,** *110* (5), 053503.

242. Yu, F.; Zhu, L. Q.; Xiao, H.; Gao, W. T.; Guo, Y. B., Restickable Oxide Neuromorphic Transistors with Spike-Timing-Dependent Plasticity and Pavlovian Associative Learning Activities. *Adv Funct Mater* **2018,** *28* (44), 1804025.

243. Suh, D. I.; Kil, J. P.; Choi, Y.; Bae, G. Y.; Park, W., An Associative Memory Device Using a Magnetic Tunnel Junction. *IEEE Transactions on Magnetics* **2015,** *51* (11), 1-4.

244. Hu, S. G.; Liu, Y.; Liu, Z.; Chen, T. P.; Wang, J. J.; Yu, Q.; Deng, L. J.; Yin, Y.; Hosaka, S., Associative memory realized by a reconfigurable memristive Hopfield neural network. *Nature Communications* **2015,** *6* (1), 7522.

245. Daimon, S.; Iguchi, R.; Hioki, T.; Saitoh, E.; Uchida, K.-i., Thermal imaging of spin Peltier effect. *Nature Communications* **2016,** *7* (1), 13754.

246. Uchida, K.-i.; Daimon, S.; Iguchi, R.; Saitoh, E., Observation of anisotropic magneto-Peltier effect in nickel. *Nature* **2018,** *558* (7708), 95-99.

Appendices

Appendix A   **Measurement facilities**

1. Lock-in thermography

Figure A-1. Image of Enhanced Lock-in Thermal Emisson (ELITE) system (DCG Systems, Inc.) for lock-in thermography measurement. The camera head contains a high-performance indium antimonide (InSb) focal plane array (FPA) detector. The FPA is cooled by a rotary stirling cooler.

2. Keithley 4200 Semicondutor Characterization System (SCS)
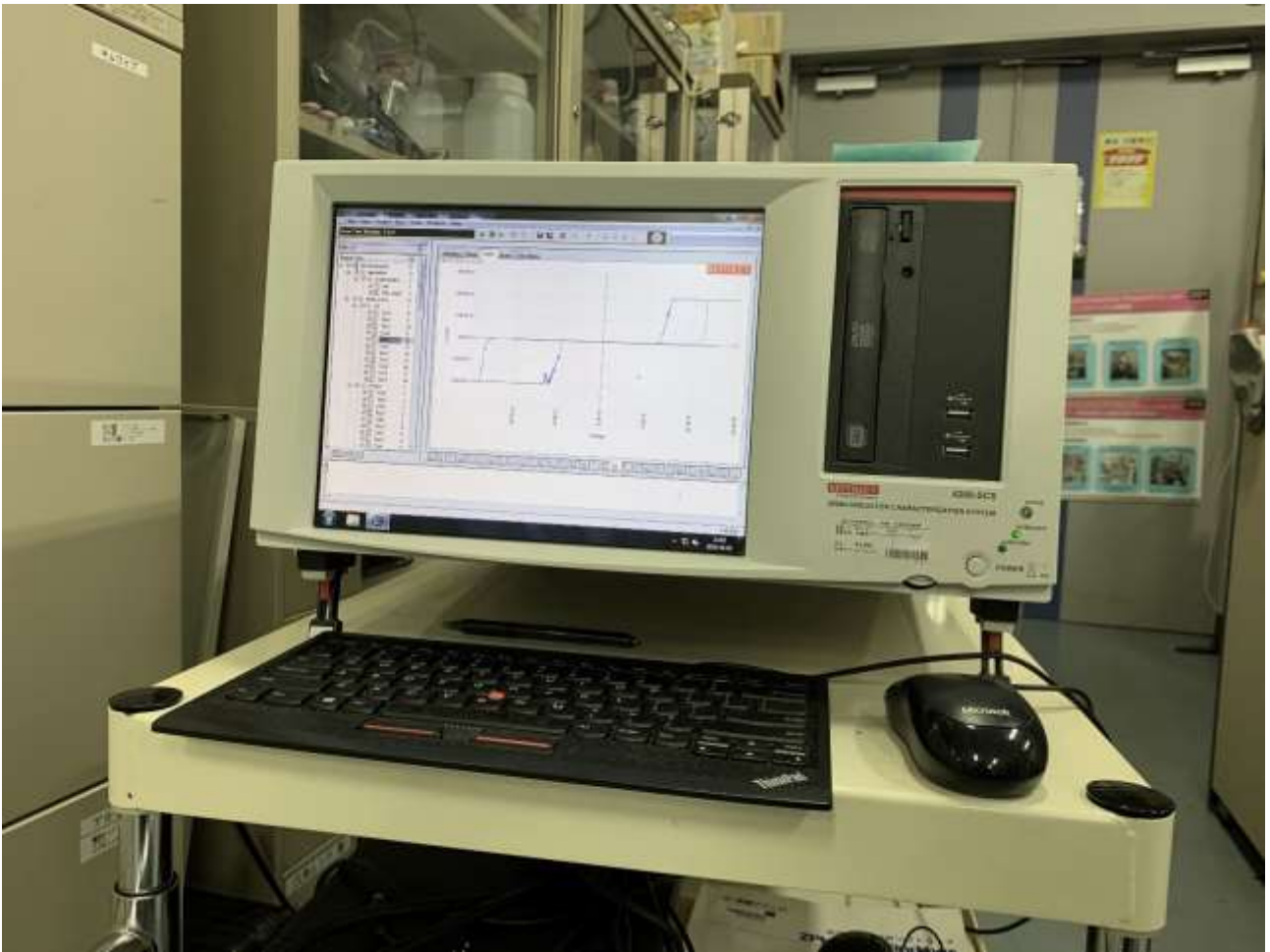
Figure A-2. Keithley 4200 semiconductor characterization system (SCS) for electrical measurement.

3. Raman spectroscopy

*Figure A-3. Confocal HR800 micro-Ramman spectrometer (Horiba Jovin Yvon), having a 100×
objective (NA= 0.8), 532 nm diode-pumped laser (2.8mW) with the spot diameter is around 1um and a piezo-
actuated XY scanner.*

4. Transmission electron microscope (TEM)

Figure A-4. JEM-2100F field emission transmission electron microscope (FE-TEM), equipped with Energy dispersive X-ray spectrometer (EDX) and electron energy loss spectrometer (EELS). The acceleration voltage is 200 kV to give an ultrahigh spatial resolution of 0.1 nm.

5. Scanning electron microscope (SEM)

Figure A-5. Hitachi SU8230 FE-SEM with EDX. It employs a novel cold field emission gun to improve the imaging and analytical performance. The spatial resolution can be 0.8 nm (@15 kV) and 1.1 nm (@ 1kV).

Figure A-6. Hitachi SU8000 FE-SEM with EDX (Bruker Quantax FQ5060). The accelerate voltage is 0.5 ~ 5 kV with a maximum magnification of 800k.

Appendix B   Nodal Analysis

For the theoretical simulation used in section 3.2, we applied nodal analysis to solve the time-dependent current evolution problem in the network. Here we employ a simple model which consists one voltage source and three resistors to demonstrate this method.
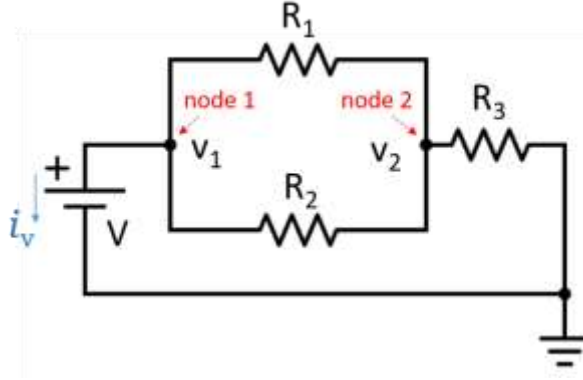
Figure B-1. A circuit with one voltage source and three resistors.

Consider the circuit in Figure B-1, taking the ground as reference, with Kirchhoff's current law, at each node we have:

$$Noda\ 1:\ i_v + \frac{v_1 - v_2}{R_1} + \frac{v_1 - v_2}{R_2} = 0$$

$$Noda\ 2:\ \frac{v_2 - v_1}{R_1} + \frac{v_2 - v_1}{R_2} + \frac{v_2}{R_3} = 0$$

and with

$$v_1 = V$$

.The equations are equivalent to:

$$\begin{bmatrix} \frac{1}{R_1} + \frac{1}{R_2} & -\frac{1}{R_1} - \frac{1}{R_2} & 1 \\ -\frac{1}{R_1} - \frac{1}{R_2} & \frac{1}{R_1} + \frac{1}{R_2} + \frac{1}{R_3} & 0 \\ 1 & 0 & 0 \end{bmatrix} \begin{bmatrix} v_1 \\ v_2 \\ i_v \end{bmatrix} = \begin{bmatrix} 0 \\ 0 \\ V \end{bmatrix}$$

.

The matrix equation has a form of:

$$Ax = z$$

This form is the general form for all circuits composed by only passive elements and independent current and voltage source. For the simulation model for voltage biased nanowire network, there was only one voltage source (assume it connects to node 1 with value V). We can construct the matrix in the following way:

$$A_{(m+1)\times(m+1)} = \begin{bmatrix} G_{m\times m} & B_{m\times 1} \\ C_{1\times m} & 0 \end{bmatrix}, x = \begin{bmatrix} v_{m\times 1} \\ i \end{bmatrix}, z = \begin{bmatrix} 0_{m\times 1} \\ V \end{bmatrix}$$

For the circuit above, we have

$$G = \begin{bmatrix} \dfrac{1}{R_1} + \dfrac{1}{R_2} & -\dfrac{1}{R_1} - \dfrac{1}{R_2} \\ -\dfrac{1}{R_1} - \dfrac{1}{R_2} & \dfrac{1}{R_1} + \dfrac{1}{R_2} + \dfrac{1}{R_3} \end{bmatrix}$$

$$B = C^T = \begin{bmatrix} 1 \\ 0 \end{bmatrix}$$

$$x = \begin{bmatrix} v_1 \\ v_2 \\ i_v \end{bmatrix}$$

$$z = \begin{bmatrix} 0 \\ 0 \\ V \end{bmatrix}$$

. If we carefully examine the form of G, we know each element in the diagonal matrix is equal to the sum of the conductance of the each element connected to the corresponding node, and the off diagonal elements are the negative conductance of the element connected between the pair of corresponding node. B and C are m dimensional matrix of 0 except the first element as 1. Then unknown x matrix can be calculated by

$$x = A^{-1}z$$

.

Appendix C Python code for simulation

creat_network.py

```python
1.  # import any external libraries
2.
3.  import math as math# several basic trigonometric functions
4.  import random as random# generate random nanowire positions, etc.
5.  import scipy.stats as stats # generate gamma-distributed nanowire lengths
6.  import numpy as np # linear algebra routines
7.  import matplotlib.pyplot as plt # graphing library
8.  import matplotlib.patches as patches # to graph electrodes
9.  import networkx as nx
10. import Savelib
11.
12. # define network parts
13. filepath=[]
14. density = 0.317
15. box_x = 100
16. box_y = 100
17. elec_len = 40
18. s_num=2
19.
20. def single_nanowire(center_x, center_y, length, angle):
21.     end_x = center_x + math.cos(angle)*length/2
22.     start_x = center_x - math.cos(angle)*length/2
23.     end_y = center_y + math.sin(angle)*length/2
24.     start_y = center_y - math.sin(angle)*length/2
25.     single_nw = np.array(((start_x,start_y),(end_x, end_y)))
26.     return single_nw
27.
28. def create_electrodes(box_x, box_y, length):
29.     source = single_nanowire(0,box_y/2,length,math.pi/2)
30.     drain = single_nanowire(box_x, box_y/2,length,math.pi/2)
31.     return source, drain
32.
33. def create_wires(box_x, box_y, density, lalpha, lloc, lbeta):
34.     nws_number = int( density*box_x*box_y)
35.     wire_length = stats.gamma.rvs(lalpha,lloc, lbeta, size=nws_number)
36.     wires=[]
37.     source, drain = create_electrodes(box_x, box_y, elec_len)
38.     wires.append(source)
39.     for i in range(nws_number):
40.         new_nw_length = abs(wire_length[i])
41.         new_nw_angle = random.uniform(0, math.pi)    #0
42.         new_nw_cx=random.uniform(0, box_x)
43.         new_nw_cy = random.uniform(0, box_y)
44.         new_nw = single_nanowire(new_nw_cx, new_nw_cy,new_nw_length,new_nw_angle)
45.         wires.append(new_nw)
46.     wires.append(drain)
47.     plt.hist(wire_length,10)
48.     plt.savefig(filepath+'nanowire_distribution',dpi=300)
49. #    plt.show()
50.     plt.clf()
51.     plt.close()
52.     data_saveDirectory = Savelib.createSaveDirectory(filepath,'nanowire_distribution')
53.     Savelib.saveExperiment(data_saveDirectory,wire_length= wire_length)
54.     return wires
55.
56. def line_intersection(line1, line2):
57.     xdiff = (line1[0][0] - line1[1][0], line2[0][0] - line2[1][0])
58.     ydiff = (line1[0][1] - line1[1][1], line2[0][1] - line2[1][1])
59.
60.     def det(a, b):
61.         return a[0] * b[1] - a[1] * b[0]
```

```python
62.
63.     div = det(xdiff, ydiff)
64.     boole_cross = False
65.     new_junction=[]
66.     if not div == 0:
67.         d = (det(*line1), det(*line2))
68.         new_junction = np.array((det(d, xdiff) / div, det(d, ydiff) / div))
69.         if (np.all((new_junction[0]-line1[0][0])*(new_junction[0]-line1[1][0])<=0)
70.             and np.all((new_junction[0]-line2[0][0])*(new_junction[0]-line2[1][0])<=0)
71.             and np.all((new_junction[1]-line1[0][1])*(new_junction[1]-line1[1][1])<=0)
72.             and np.all((new_junction[1]-line2[0][1])*(new_junction[1]-line2[1][1])<=0)):
73.             boole_cross = True
74.     return boole_cross, new_junction
75.
76. def create_junctions(wires):
77.     col = len(wires)
78.     junctions=[]
79.     junction_matrix=[]
80.     network_map = np.zeros((col,col))
81.     for i, nwa in enumerate(wires):
82.         for j, nwb in enumerate(wires):
83.             if i<j:
84.                 boole_cross, new_junction= line_intersection(nwa,nwb)
85.                 if boole_cross:
86.                     network_map[i][j]=network_map[j][i]=1
87.                     junctions.append(new_junction)
88.                     junction_matrix.append([i,j])
89.     return network_map, junctions, junction_matrix
90.
91.
92. def plot_network(wires, junctions,ax):
93.     """Plot a network."""
94.     ax.set_axis_off()
95.     sE=patches.Rectangle((0.,(box_y-elec_len)/2),-
    10,elec_len,facecolor='gold') #set electrode transparent  add alpha=0.5
96.     ax.add_patch(sE)
97.     dE=patches.Rectangle((box_x,(box_y-elec_len)/2),10,elec_len,facecolor='gold')
98.     ax.add_patch(dE)
99.     for i ,wire in enumerate(wires):
100.        #color = 'blue' if network else 'red'
101.        if i==0 or i == len(wires)-1:
102.            plt.plot([wire[0][0],wire[1][0]],[wire[0][1],wire[1][1]], color='gold',linewid
    th=1)
103.
104.        else:
105.            plt.plot([wire[0][0],wire[1][0]],[wire[0][1],wire[1][1]], color='dodgerblue',l
    inewidth=1.2)
106.    for _,junction in enumerate(junctions):
107.        plt.plot([junction[0]], [junction[1]], 'o',color='dodgerblue',markersize=3)
108.
109.def isolate_wire(wires,network_map):
110.    isolate_list=[]
111.    sim_wires = wires.copy()
112.    sim_map = network_map.copy()
113.    wires_number = len(sim_wires)
114.    for loop in range(int(wires_number/2)):
115.        for i in range(wires_number):
116.            if np.sum(sim_map[i])<2 and i not in [0, wires_number-1]:
117.                isolate_list.append(i)
118.                sim_wires[i]='0'
119.                sim_map[i]=sim_map[:,i]=np.zeros(wires_number)
120.    while '0' in sim_wires:
121.        sim_wires.remove('0')
122.    return  sim_wires, isolate_list,sim_map
123.
124.def create_map():
125.    lalpha = 12 #12
```

```
126.    lloc = 0.05 #0.05
127.    lbeta= 0.85  #0.99
128.    wires = create_wires(box_x, box_y, density, lalpha, lloc, lbeta)
129.    network_map, junctions,junction_matrix= create_junctions(wires)
130.    print('N(nanowire)=', len(wires),'; N(junction)=', len(junctions))
131.    _,ax=plt.subplots()
132.    plt.title('original network')
133.    ax.set_xlim(-10,box_x+10)
134.    ax.set_ylim(-5,box_y+5)
135.    plot_network(wires,junctions,ax)
136.    plt.savefig(filepath+'original_network',dpi=300)
137.#   plt.show()
138.    plt.clf()
139.    plt.close()
140.
141.    sim_wires,isolate_list,sim_map = isolate_wire(wires,network_map)
142.    input_map, sim_junctions,sim_junction_matrix = create_junctions(sim_wires)
143.    print('N(nanowire)=', len(sim_wires),'; N(junction)=', len(sim_junctions))
144.    _,ax2=plt.subplots()
145.    plt.title('simulated network D='+str(density))
146.    ax.set_xlim(-10,box_x+10)
147.    ax.set_ylim(-5,box_y+5)
148.    plot_network(sim_wires,sim_junctions,ax2)
149.    plt.savefig(filepath+'isolated_network',dpi=300)
150.    #plt.show()
151.    plt.clf()
152.    plt.close()
153.    return input_map, sim_wires, sim_junctions,sim_junction_matrix
```

network_simulation_config.py

```
1.   import networkx as nx
2.   import numpy as np
3.   import math
4.   import matplotlib.pyplot as plt
5.   from numpy import genfromtxt
6.   import create_network as create_nw
7.   from decimal import Decimal as de
8.   import scipy.stats as stats # generate gamma-distributed width distribution
9.   import Savelib
10.  '''''
11.  define initial parameters:
12.     w_in: length of filament at t0
13.     w_out: length of filament at t1
14.     V_diff: voltage drop across one junction
15.     t_rise: time constant of filament growth
16.     t_fall: time constant of filament disolve
17.     w_len: insulator thickness at each junction
18.
19.  '''
20.  class simulation_config(object):
21.      def __init__(self):
22.          self.input_map, self.wires, self.junctions, self.sim_junction_matrix= create_nw.cr
     eate_map()
23.          self.P = nx.MultiGraph(self.input_map)
24.
25.
26.          self.w_ini = 0.001       #define width initial value
27.          self.wl_ini = 40         #defin width lenth initial value
28.          self.E_cut = 0.005    #thermal break down of single junction, E_default = 0.000005
29.          self.filepath=[]
30.
31.          self.w_cut = 100      #width cut for conductance functon
32.          self.t_rise = 5
33.          self.t_fall = 20
34.          self.t_con=0.1
35.
36.          self.walpha = 2
37.          self.wloc = 0.05
38.          self.wscale = 0.8
39.
40.          self.G_comp=1E7
41.          self.G_on = 1E-7
42.          self.G_off = 1E-12
43.          self.m = self.P.number_of_nodes() #node number, nanowires
44.          self.n = self.P.number_of_edges() #edge number, junctions
45.          print('N(nanowire)=', self.m,'; N(junction)=', self.n)
46.      #define functions:
47.      def V_func(self, V_high,k,time_len): #voltage input waveform
48.          if k==1:
49.              v_input=V_high*np.ones(time_len)
50.          elif k == 2:
51.              v_input=np.linspace(0,V_high,time_len//2)
52.              v_input=np.append(v_input,np.linspace(V_high,0,time_len//2))
53.          elif k == 3:
54.              v_input=np.linspace(0,V_high,time_len//4)
55.              v_input = np.append(v_input,np.linspace(V_high,-V_high,time_len//2))
56.              v_input = np.append(v_input, np.linspace(-V_high,0,time_len//4))
57.          elif k==4:
58.              v_input=V_high*np.ones(time_len//2)
59.              # v_input = np.append(v_input,0.1*V_high*np.ones(time_len//2))
60.              v_input = np.append(v_input,np.zeros(time_len//2-2))
61.              v_input = np.append(v_input,V_high*np.ones(2))
62.          return v_input
63.
```

```python
64.     def pulse_V(self, V_high, V_low, t_high, t_low, t_res):
65.         v_input = V_low*np.ones(int(de(str(t_low))/de(str(t_res))))
66.         v_input = np.append(v_input, V_high*np.ones(int(de(str(t_high))/de(str(t_res)))))

67.         return v_input
68.
69.     def pulse_train(self, write_V_high,write_V_low,read_V_high,read_V_low, write_n, read_n
    , write_t_high, write_t_low, read_t_high, read_t_low, t_res):
70.         v_input=[]
71.         Time=[]
72.         T = (de(str(write_t_high))+de(str(write_t_low)))*write_n+(de(str(read_t_low))+de(s
    tr(read_t_high)))*read_n
73.         for i in range(write_n):
74.             v_input = np.append(v_input,self.pulse_V(write_V_high,write_V_low,write_t_high
    , write_t_low,t_res ))
75.         for i in range(read_n):
76.             v_input = np.append(v_input,self.pulse_V(read_V_high,read_V_low,read_t_high, r
    ead_t_low,t_res ))
77.         Time = np.linspace(0, float(T),len(v_input))
78.         return v_input, Time
79.
80.     def pulse_train_rw(self, write_V_high,write_V_low,read_V_high,read_V_low, write_n, rea
    d_n, write_t_high, write_t_low, read_t_high, read_t_low, t_res):
81.         v_input=[]
82.         Time=[]
83.         T = (de(str(write_t_high))+de(str(write_t_low)))*write_n+(de(str(read_t_low))+de(s
    tr(read_t_high)))*read_n
84.         for i in range(read_n):
85.             v_input = np.append(v_input,self.pulse_V(read_V_high,read_V_low,read_t_high, r
    ead_t_low,t_res ))
86.         for i in range(write_n):
87.             v_input = np.append(v_input,self.pulse_V(write_V_high,write_V_low,write_t_high
    , write_t_low,t_res ))
88.         Time = np.linspace(0, float(T),len(v_input))
89.         return v_input, Time
90.
91.     def pulse_train2(self, write_V_high,write_V_low,read_V_high,read_V_low, write_n, read_
    n, write_t_high, write_t_low, read_t_high, read_t_low, t_res):
92.         v_input=[]
93.         T= (de(str(write_t_high))+de(str(write_t_low)))*write_n*2+(de(str(read_t_low))+de(
    str(read_t_high)))*read_n
94.         for i in range(write_n):
95.             v_input = np.append(v_input,self.pulse_V(write_V_high,write_V_low,write_t_high
    , write_t_low,t_res ))
96.         for i in range(read_n):
97.             v_input = np.append(v_input,self.pulse_V(read_V_high,read_V_low,read_t_high, r
    ead_t_low,t_res ))
98.         for i in range(write_n):
99.             v_input = np.append(v_input,self.pulse_V(write_V_high,write_V_low,write_t_high
    , write_t_low,t_res ))
100.        Time = np.linspace(0, float(T),len(v_input))
101.        return v_input, Time
102.
103.        #generate width_ini and Conductance_ini
104.    def ini_cond(self):
105.        width_ini = np.zeros((self.m,self.m))
106.        cond_ini = np.zeros((self.m,self.m))
107.        l=0
108.        for i in range(self.m):
109.            for j in range(self.m):
110.                if j>i and self.input_map[i][j]>0:
111.                    width_ini[i][j]=width_ini[j][i] = np.random.normal(self.w_ini,0.001,se
    lf.n)[l]
112.                    cond_ini[i][j]=cond_ini[j][i] = self.condc(width_ini[i][j],1)
113.                    l+=1
114.        return cond_ini, width_ini
115.
```

```python
116.    def width_distribute(self):
117.        width_array = np.zeros((self.m,self.m))
118.        w_array = stats.gamma.rvs(self.walpha,self.wloc, self.wscale, size=self.n)
119.        l=0
120.        for i in range(self.m):
121.            for j in range(self.m):
122.                if j>i and self.input_map[i][j]>0:
123.                    width_array[i][j]=width_array[j][i] = w_array[l]
124.                    l+=1
125.        plt.hist(w_array,10)
126.        plt.savefig(self.filepath+'junction_length_distribution',dpi=100)
127.        plt.clf()
128.        plt.close()
129.        data_saveDirectory = Savelib.createSaveDirectory(self.filepath,'junction_length_di
    stribution')
130.        Savelib.saveExperiment(data_saveDirectory,width= w_array)
131.        return width_array
132.
133.    def width_grow(self, w_in,V_diff, delt_t, w_len):
134.
135.        delt_w1 = delt_t*V_diff/self.t_rise
136.        delt_w2= -delt_t*math.fabs(w_in)/self.t_fall
137.        w_out = math.copysign(math.fabs(w_in + delt_w1)+ delt_w2,w_in+delt_w1)
138.
139.        if math.fabs(w_out)>w_len:
140.            w_out = math.copysign(w_len,w_out)
141.        elif math.fabs(w_out)-math.fabs(w_in)<0 and w_in*V_diff>0 and w_out*V_diff<0 :
142.            w_out=0
143.            # print('weight erro')
144.        return w_out
145.
146.    def width_G_convert(self,width,w_len):
147.        func1 = self.G_on*math.fabs(width)+self.G_off*(w_len-math.fabs(width))
148.        return func1
149.
150.    def condc(self, width, w_len):
151.        width=math.fabs(width)
152.        if width<self.w_cut:
153.            func = self.width_G_convert(width, w_len)
154.        elif width >= self.w_cut:
155.            G_cut = self.width_G_convert(self.w_cut, w_len)
156.            g_para1=(self.G_on-G_cut)/(math.exp(1/self.t_con)-
    math.exp(self.w_cut/self.t_con))
157.            g_para2=self.G_on-g_para1*math.exp(1/self.t_con)
158.            func = g_para1*math.exp(math.fabs(width)/self.t_con)+g_para2
159.        return func
160.
161.    def v_array(self, G_pre,I_input):
162.        G=np.zeros((self.m,self.m))
163.        for i in range(self.m):
164.            for j in range(self.m):
165.                if self.input_map[i][j]>0:
166.                    G[i][i]+=G_pre[i][j]
167.                    G[i][j]=-G_pre[i][j]
168.        G[0][0]+=self.G_comp
169.        G=G[:self.m-1,:self.m-1]
170.        B=np.zeros((self.m-1,1))
171.        B[0]=1
172.        C=B.transpose()
173.        A = np.zeros((self.m,self.m))
174.        A[:-1,:-1]=G
175.        Z= np.zeros((self.m,1))
176.        Z[0]=I_input
177.
178.        X=np.linalg.solve(A,Z)
179.        v_sum = -np.copy(X[0])
180.        v_node =np.copy(X)
```

```
181.          v_node[-1]=0
182.          v_node = np.transpose(v_node)
183.          return v_node, v_sum
184.
185.      def v_convert(self, X):
186.          vmap=np.zeros((self.m,self.m))
187.          for i in range(self.m):
188.              for j in range(self.m):
189.                  if self.input_map[i][j]>0 and i<j:
190.                      vmap[i][j]=vmap[j][i]=(X[i]-X[j])
191.          return vmap
192.
193.      def weigh_convert(self, W):
194.          W_out = np.zeros((W.shape[0],self.n))
195.          for k in range(W.shape[0]):
196.              l=0
197.              for i in range(W.shape[1]):
198.                  for j in range(W.shape[2]):
199.                      if j>i and self.input_map[i][j]>0:
200.                          W_out[k][l]=math.fabs(W[k][i][j])
201.                          l+=1
202.          return W_out
203.
204.      def i_convert(self, I):
205.          i_out = np.zeros((I.shape[0], self.m))
206.          for k in range(I.shape[0]):
207.              for i in range(self.m):
208.                  for j in range(self.m):
209.                      if I[k][i][j]>0:
210.                          i_out[k][i]+= I[k][i][j]
211.
212.          return i_out
213.      #start simulation with G_grow
214.      def sim_net(self,v_input,Time):
215.          time_len = len(Time)
216.          width = np.zeros((time_len,self.m,self.m))
217.          I=np.zeros((time_len,self.m,self.m))
218.          G=np.zeros((time_len,self.m,self.m))
219.          V=np.zeros((time_len,self.m,self.m))
220.          E=np.zeros((self.m,self.m))
221.          delt_t = Time[1]-Time[0]
222.          v_node=np.zeros((time_len,self.m))
223.          cond_ini, width_ini = self.ini_cond()
224.          width_len = self.width_distribute()
225.          I_sum = np.zeros(time_len)
226.          #get G_t1, I_map!!!
227.          for k,t in enumerate(Time):
228.              G[k]=cond_ini
229.              v_node[k,:], I_sum[k] = self.v_array(cond_ini, v_input[k])
230.              V[k]=self.v_convert(v_node[k])
231.              for i in range(self.m):
232.                  for j in range(self.m):
233.                      I[k][i][j]=V[k][i][j]*G[k][i][j]
234.                      if j>i and self.input_map[i][j]>0:
235.                          E[i][j] += I[k][i][j]*V[k][i][j]*delt_t
236.                          if E[i][j]> self.E_cut:
237.                              width[k][i][j]= width[k][j][i]= width_ini[i][j]=0
238.                              cond_ini[i][j]=cond_ini[j][i] = self.condc(width_ini[i][j],wid
    th_len[i][j])
239.                              E[i][j]=0
240.                          else:
241.                              width[k][i][j]= width[k][j][i]=width_ini[i][j]

242.                              width_ini[i][j]=self.width_grow(width_ini[i][j],V[k][i][j],del
    t_t,width_len[i][j])
243.                              cond_ini[i][j]=cond_ini[j][i] = self.condc(width_ini[i][j],wid
    th_len[i][j])
```

```python
244.         I_edge = self.weigh_convert(I)
245.         I_node = self.i_convert(I)
246.         G_edge = self.weigh_convert(G)
247.         W_edge = self.weigh_convert(width)
248.         return I, V, G ,E, width, v_node,I_sum, I_edge, G_edge, W_edge,I_node
249.
250.     def sim_net2(self,v_input,Time,cond_ini,width_ini):
251.         time_len = len(Time)
252.         width = np.zeros((time_len,self.m,self.m))
253.         I=np.zeros((time_len,self.m,self.m))
254.         G=np.zeros((time_len,self.m,self.m))
255.         V=np.zeros((time_len,self.m,self.m))
256.         E=np.zeros((self.m,self.m))
257.         delt_t = Time[1]-Time[0]
258.         v_node=np.zeros((time_len,self.m))
259.         I_sum = np.zeros(time_len)
260.         width_len = self.width_distribute()
261.         #get G_t1, I_map!!!
262.         for k,t in enumerate(Time):
263.             G[k]=cond_ini
264.             v_node[k,:], I_sum[k] = self.v_array(cond_ini, v_input[k])
265.             V[k]=self.v_convert(v_node[k])
266.             for i in range(self.m):
267.                 for j in range(self.m):
268.                     I[k][i][j]=V[k][i][j]*G[k][i][j]
269.                     if j>i and self.input_map[i][j]>0:
270.                         E[i][j] += I[k][i][j]*V[k][i][j]*delt_t
271.                         width[k][i][j]= width[k][j][i]=width_ini[i][j]
272.                         width_ini[i][j]=self.width_grow(width_ini[i][j],V[k][i][j],delt_t,
    width_len[i][j])
273.                         cond_ini[i][j]=cond_ini[j][i] = self.condc(width_ini[i][j],width_l
    en[i][j])
274.         I_edge = self.weigh_convert(I)
275.         I_node = self.i_convert(I)
276.         G_edge = self.weigh_convert(G)
277.         W_edge = self.weigh_convert(width)
278.         return I, V, G ,E, width, v_node,I_sum, I_edge, G_edge, W_edge,I_node
```

simulation.py

```
1.  import network_simulation_config as config
2.  import networkx as nx
3.  import numpy as np
4.  import matplotlib.pyplot as plt
5.  from decimal import Decimal as de
6.  import Savelib
7.  import matplotlib.colors as pcolors
8.  import matplotlib.patches as patches # to graph electrodes
9.  import create_network as create_nw
10.
11. filepath = 'data/net_p89/'
12.
13. create_nw.filepath =  filepath
14. create_nw.density = 0.1
15. create_nw.box_x=60
16. create_nw.box_y=60
17.
18. dataname =  'datafile'
19. data_saveDirectory = Savelib.createSaveDirectory(filepath, dataname)
20. Savelib.copyFiles(filepath)
21. cf = config.simulation_config()
22. cf.w_cut =0
23. cf.E_cut = 5000  #thermal break down of single junction, E_default = 0.000005
24.
25.
26. pos = nx.spring_layout(cf.P)
27. #pos = nx.circular_layout(cf.P)
28. options = {'node_color':'black','node_size':10, 'width': 1, 'pos':pos, 'edge_camp':plt.cm.
    spring}
29. nx.draw(cf.P,**options,)
30. nx.draw_networkx_nodes(cf.P,pos,nodelist=[0],node_color = 'red', node_size = 150, alpha =
    0.8)
31. nx.draw_networkx_nodes(cf.P,pos,nodelist=[cf.m-
    1],node_color = 'blue', node_size = 150, alpha = 0.8)
32. plt.savefig(filepath+'map'+'.png',dpi=300)
33. #plt.show()
34. plt.clf()
35.
36. input_map = cf.input_map
37. con_ini, width_ini= cf.ini_cond()
38.
39. V_high = np.array([25])
40. t_fall = np.array([5])
41. t_rise = np.array([3,2.5,2])
42. t_con = np.array([0.02,0.05,0.1])
43.
44. t_low= np.array([2])
45. t_high = np.array([0.2])
46. t_sleep = np.array([20])
47. t_res = 0.005
48.
49. def create_data(write_V_high,write_V_low,read_V_high,read_V_low, write_n, read_n, write_t_
    high, write_t_low,read_t_high,read_t_low,t_res,con_ini, width_ini):
50.     ''''''define pulse train'''
51.     v_input, Time = cf.pulse_train_rw(write_V_high,write_V_low,read_V_high,read_V_low, wri
    te_n, read_n, write_t_high, write_t_low,read_t_high,read_t_low,t_res)
52.     ''''''start simulation'''
53.     print('measure time = ', Time[-1], ' frame = ', len(v_input))
54.     I, V, G ,E, width, v_node,I_sum, I_edge, G_edge, W_edge,I_node= cf.sim_net2(v_input,Ti
    me, con_ini, width_ini)
55.     return I, V, G ,E, width, v_node,I_sum, I_edge, G_edge, W_edge,I_node, Time, v_input
56.
57. def fd_save(Time,v_input,v_node,I_sum, I_edge, G_edge, W_edge,I_node,savename):
```

```python
58.     subtitle_name ='V:'+str(write_V_high)+'V/mesT:'+"{:.1f}".format(Time[-
    1])+'s\n'+'tau:R='+"{:.1f}".format(rise)+',F='+"{:.1f}".format(fall)+' ,tcon='+"{:.2f}".fo
    rmat(tcon)
59.     plt.figure(figsize=(5,20))
60.
61.     plt.subplot(611)
62.     plt.plot(Time, v_input)
63.     plt.title('V-t\n'+subtitle_name)
64.     plt.subplot(612)
65.     plt.plot(Time,I_sum)
66.     plt.title('I-t\n'+ subtitle_name)
67.     plt.subplot(613)
68.     plt.plot(v_input,I_sum)
69.     plt.title('I-V\n'+subtitle_name)
70.     plt.subplot(614)
71.     plt.plot(Time,I_node)
72.     plt.title('I_node-t\n'+subtitle_name)
73.     plt.subplot(615)
74.     plt.plot(Time,G_edge)
75.     plt.title('G_edge-t\n'+subtitle_name)
76.     plt.subplot(616)
77.     plt.plot(Time,W_edge)
78.     plt.title('width-t\n'+subtitle_name)
79.     plt.tight_layout()
80.     plt.savefig(filepath+savename+'.png')
81.     plt.clf()
82.
83.     #save data
84.     data_saveDirectory = Savelib.createSaveDirectory(filepath, savename)
85.     Savelib.saveExperiment(data_saveDirectory,input_map = cf.input_map, I_edge=I_edge, G_e
    dge=G_edge, v_input =v_input, W_edge=W_edge, Time = Time, I_sum = I_sum,v_node = v_node,I_
    node=I_node, wires = cf.wires, junctions = cf.junctions)
86.
87. def CSS_sim(write_V_high,savename,t_high,t_low,fall, rise, tcon):
88.     cf.t_fall = fall
89.     cf.t_rise = rise
90.     cf.t_con=tcon
91.
92.     '''''define pulse train'''
93.     write_V_low = 0
94.     write_t_high = 0.1
95.     write_t_low = 0.1
96.     write_n= int(de('10')/(de(str(write_t_high))+de(str(write_t_low))))
97.
98.
99.     read_V_low = 0
100.    read_V_high = write_V_high
101.
102.    '''''get write_n'''
103.    con_ini0=np.copy(con_ini)
104.    width_ini0=np.copy(width_ini)
105.    I0, V0, G0 ,E0, width0, v_node0,I_sum0, I_edge0, G_edge0, W_edge0,I_node0, Time, v_in
    put0 = create_data(write_V_high,write_V_low,0,read_V_low, write_n, 0, write_t_high, write_
    t_low,0,0,t_res,con_ini0, width_ini0)
106.    fd_save(Time0, v_input0,v_node0,I_sum0, I_edge0, G_edge0, W_edge0,I_node0,savename)

107.    write_n_list=[]
108.    for f in range(len(I_sum0)):
109.        if 0.96E-7<I_sum0[f]<2E-7:
110.            write_n_list.append(int(f*de(str(t_res)))/(de(str(write_t_high))+de(str(write_t
    _low)))))
111.    write_n = write_n_list[0]
112.    print(write_n,f, I_sum0[f])
113.
114.    '''''learning innput'''
115.    con_ini1=np.copy(con_ini)
116.    width_ini1=np.copy(width_ini)
```

```python
117.     I1, V1, G1 ,E1, width1, v_node1,I_sum1, I_edge1, G_edge1, W_edge1,I_node1, Time1, v_in
   put1 = create_data(write_V_high,write_V_low,0,0, write_n,0, write_t_high, write_t_low,0,0,
   t_res,con_ini1, width_ini1)
118.
119.     def css(read_V,read_t_high,read_t_low, appendname):
120.         t_rel=0
121.         con_ini2=np.copy(G1[-1])
122.         width_ini2=np.copy(width1[-1])
123.         I2, V2, G2 ,E2, width2, v_node2,I_sum2, I_edge2, G_edge2, W_edge2,I_node2, Time2,
   v_input2 = create_data(write_V_high,write_V_low,read_V,read_V_low, write_n, read_n, write_
   t_high, write_t_low,read_t_high,read_t_low,t_res,con_ini2, width_ini2)
124.
125.         for p in range(len(I_sum2)):
126.             if I_sum1[-1]*0.7<I_sum2[p]<=I_sum1[-1]:
127.                 t_rel = int(p*de(str(t_res)))
128.
129.         I_sum = np.append(I_sum1, I_sum2)
130.         I_edge=np.zeros((len(I_sum),cf.n))
131.         G_edge=np.zeros((len(I_sum),cf.n))
132.         W_edge=np.zeros((len(I_sum),cf.n))
133.         I_node=np.zeros((len(I_sum),cf.m))
134.         v_node=np.zeros((len(I_sum),cf.m))
135.         I_edge[:len(Time1),:]=I_edge1
136.         I_edge[len(Time1):,:]=I_edge2
137.         G_edge[:len(Time1),:]=G_edge1
138.         G_edge[len(Time1):,:]=G_edge2
139.         W_edge[:len(Time1),:]=W_edge1
140.         W_edge[len(Time1):,:]=W_edge2
141.         I_node[:len(Time1),:]=I_node1
142.         I_node[len(Time1):,:]=I_node2
143.         v_node[:len(Time1),:]=v_node1
144.         v_node[len(Time1):,:]=v_node2
145.         Time = np.append(Time1, Time2+Time1[-1])
146.         v_input= np.append(v_input1,v_input2)
147.
148.         fd_save(Time,v_input,v_node,I_sum, I_edge, G_edge, W_edge,I_node,savename+appendna
   me)
149.         return Time1[-1], t_rel
150.
151.
152.     t_scale=[]
153.     for g, read_t_high in enumerate(t_high):
154.         for j, t_s in enumerate(t_sleep):
155.             for l, read_t_low in enumerate(t_low):
156.                 read_t_low=read_t_low-read_t_high
157.                 read_n = int(de(str(t_s))/(de(str(read_t_low))+de(str(read_t_high))))
158.                 t_l, t_rl = css(read_V_high,read_t_high,read_t_low,'_'+str(g)+'_'+str(j)+'
   _'+str(l)+'CSS')
159.                 t_rl=t_rl-t_s
160.                 t_scale.append((read_t_high, t_s,read_t_low,1, t_l,t_rl))
161.     print(t_scale)
162.     return t_scale
163.
164.for n, tcon in enumerate(t_con):
165.     for i, write_V_high in enumerate(V_high):
166.         for k, fall in enumerate(t_fall):
167.             for m,rise in enumerate(t_rise):
168.                 savename=dataname +'_'+str(n)+'_'+str(i)+'_'+str(k)+'_'+str(m)
169.                 time_scale = CSS_sim(write_V_high,savename,t_high,t_low,fall, rise, tcon)
```

Appendix D Achievements

Publications:

1. <u>Q. Li</u>, A. Diaz-Alvarez, D. Tang, R. Higuchi, Y. Shingaya and T. Nakayama, "Sleep-dependent memory consolidation in a neuromorphic nanowire network." (accepted) ACS Applied Materials & Interface.
2. <u>Q. Li</u> & A. Diaz-Alvarez, R. Iguchi, J. Hochstetter, A. Loeffler, R. Zhu, Y. Shingaya, Z. Kuncic, K. Uchida and T. Nakayama (2020). "Dynamic electrical pathway tuning in neuromorphic nanowire networks." Advanced Functional Materials.
3. <u>Q. Li</u>, X. F. Zhang, D. Jiang, Y. Shingaya, D. Tsuya and T. Nakayama (2020). "Raman intensity oscillation of graphene over SiO_2/Si micro-cavity." Japanese Journal of Applied Physics 59(2): 4.
4. A. Diaz-Alvarez, R. Higuchi, <u>Q. Li</u>, Y. Shingaya and T. Nakayama (2020). "Associative routing through neuromorphic nanowire networks." AIP Advances 10(2): 025134.
5. Y. F. Wu, H. Xiao, <u>Q. Li</u>, X. Li, Z. Li, G. Mu, D. Jiang, T. Hu and X. M. Xie (2019). "The transport properties in graphene/single-unit-cell cuprates van der Waals heterostructure." Superconductor Science and Technology 32(8): 085007.

Award:

Excellent Poster Presentation Award
"Connectivity memory in $Ag@TiO_2$ nanowire network" @ The 11th MANA International Symposium 2018, Tsukuba, Japan

Oral presentations:

1. Q. Li, Y. Shingaya, D. Tsuya and T. Nakayama, "Effect of controlled isotropic strain on the electrical resistance of suspended graphene", The 76th JSAP Autumn meeting, 2015, Nagoya, Japan
2. Q. Li, Y. Shingaya, D. Tsuya and T. Nakayama, "Observing surface plasmons on suspended graphene by Raman Spectroscopy", The 77th JSAP Autumn meeting, 2016, Niigata, Japan
3. Q. Li, R. Higuchi, Y. Shingaya, Y. Kato, K. Tanaka and T. Nakayama., "Functionalized PANI network conductor towards future computation", The 64th JSAP Spring Meeting, 2017, Yokohama, Japan
4. Q. Li, R. Higuchi, Y. Shingaya and T. Nakayama, "Novel application of memristive nanowire complex network for brain-like computation", The 78th JSAP Autumn meeting, 2017, Fukuoka, Japan
5. Q. Li, Y. Shingaya and T. Nakayama, "Connectivity memory in $Ag@TiO_2$ nanowire network", The 66th JSAP Spring Meeting, 2019, Tokyo, Japan
6. Q. Li, Y. Shingaya and T. Nakayama, "Effect of surface oxygen density on memory efficiency of single $Ag@TiO_2$ nanowire", ACSIN14 & ICSPM26, 2018, Sendai, Japan

Poster presentations:

1. Q. Li, D. Tsuya, Y. Shingaya and T. Nakayama,, "Electromechanical properties of graphene under isotropic strain", The 7th international symposium on surface science, 2014, Matsue, Japan

2. Q. Li, Y. Shingaya, D. Tsuya and T. Nakayama, "Electromechanical properties of suspended graphene under isotropic strain", the 2nd International Symposium on the Functionality of Organized Nanostructures, 2014, Tokyo, Japan

3. Qiao Li et al., "Multiple-probe SPM Measurements of the Electrical Resistance of Suspended Graphene under Controlled Isotropic Strain", MANA international symposium 2015, Tsukuba, Japan

4. Q. Li, R. Higuchi, Y. Shingaya, Y. Kato, K. Tanaka and T. Nakayama, "Functionalized PANI network conductor towards future computation", MANA international symposium 2017, Tsukuba, Japan

5. Q. Li, R. Higuchi, Y. Shingaya, Y. Kato, K. Tanaka and T. Nakayama, "Functionalized PANI network conductor towards future computation", International Symposium on Atomic Switch: Invention, Practical Use and Future Prospects, 2017, Tsukuba, Japan

6. Q. Li, R. Higuchi, Y. Shingaya and T. Nakayama, "Novel application of TiO_2/Ag nanowire network for neuromorphic computation", International Conference on Nanoscience and Nanotechnology 2018, Wollongong, Australia

7. Q. Li, R. Higuchi, Y. Shingaya and T. Nakayama, "Connectivity memory in Ag@TiO_2 nanowire network", MANA international symposium 2018, Tsukuba, Japan

8. Q. Li, A. Diaz-Alvarez, R. Higuchi, Y. Shingaya and T. Nakayama, "Bio-inspired memorization in memristive network", MANA international symposium 2019, Tsukuba, Japan